Turbulence and Transport Phenomena in Edge and Scrape-Off-Layer Plasmas

by

István Cziegler

M.S. Physics (2005)

Eötvös Loránd University, Budapest

Submitted to the Department of Physics
in partial fulfillment of the requirements for the degree of

Doctor of Philosophy

at the

MASSACHUSETTS INSTITUTE OF TECHNOLOGY

September 2011

Author .....
Department of Physics
June 24, 2011

Certified by .....
Miklos Porkolab
Professor of Physics
Thesis Supervisor

Certified by .....
James L. Terry
Principal Research Scientist, Alcator Project
Thesis Supervisor

Accepted by .....
Krishna Rajagopal
Professor of Physics, Associate Head for Education, Physics

Turbulence and Transport Phenomena in Edge and Scrape-Off-Layer Plasmas

by

István Cziegler

Submitted to the Department of Physics
on June 24, 2011, in partial fulfillment of the
requirements for the degree of
Doctor of Philosophy

Abstract

This thesis reports recent experimental studies of edge turbulence structure using gas-puff-imaging at high time resolution in a radially broad zone at the low-field-side of Alcator C-Mod[1], and highlights the connections between its characteristics and particle transport.

Within the framework of this thesis a new detector system has been designed and built for viewing the steep gradient outboard midplane region at minor radii $0.9 < r/r_{\max} < 1.1$, where turbulence is postulated to be driven [2, 3]. The design is optimized for the study of edge and scrape-off-layer turbulence, based on previous studies of these regions.

Analysis of the data from this diagnostic in Ohmic L-modes from the electron diamagnetic drift propagating turbulence in the closed field line region of the plasma edge shows a strong scaling of the fluctuation power $\tilde{n}/n$ with the density normalized to the tokamak density limit $\bar{n}_e/n_G$; in addition, a critical physical scale is found at $k_\theta^c \rho_s \approx 0.1$, where the critical wavenumber is normalized to ρ_s, the ion Larmor radius at the sound speed, also known as the drift scale. The characteristic size scale shows very little variation with operating parameters. The analysis of the physical scale includes spectral analysis, yielding robust spectral indices $\beta \approx 4.5$ for larger wavenumbers and a sensitive spectral shape for lower wavenumbers, and the first spectral transfer measurement of turbulence on C-Mod, showing that the critical scale feeds power into the turbulence. A connection is found to the quasi-coherent mode (QCM), a modelike edge fluctuation characteristic of the Enhanced D-Alpha H-mode, which also appears at $k_\theta^{\mathrm{QCM}} \rho_s \approx 0.1$ and has decreased inverse transfer but greatly enhanced forward transfer compared to the L-mode levels.

Thesis Supervisor: Miklos Porkolab
Title: Professor of Physics

Thesis Supervisor: James L. Terry
Title: Principal Research Scientist, Alcator Project

Acknowledgments

At the end of my graduate studies at the Plasma Science and Fusion Center of MIT I feel that first of all I owe a great deal of gratitude to my thesis advisor Prof Miklos Porkolab who, as he likes to put it, discovered me at a conference in Hungary. Without his support and encouragement I would never have come to MIT, much less to the end of my doctoral training. Further, I am thankful for his pointing me to Jim Terry, my supervisor who has truly been the most helpful advisor all these years. His keen experimentalist and engineering insight and infinite patience in our long conversations – even with my sometimes esoteric problems and interests – always provided me with a huge uplift. I have been very fortunate to be his student and I really appreciate his open mind and support for my activities outside the field of physics.

I would also like to extend my appreciation to the researchers and professors who have contributed to this research and to my education: Doctors Paul Bonoli, Darin Ernst, Catherine Fiore, Jeffrey Freidberg, Robert Granetz, Martin Greenwald, Amanda Hubbard, Jerry Hughes, Ian Hutchinson, Jim Irby, Brian LaBombard, Bruce Lipschultz, Earl Marmar, Ron Parker, Abhay Ram, John Rice, Steve Scott, Dennis Whyte, Steve Wolfe, Steve Wukitch, and Stewart Zweben. There are a number of people who deserve special recognition for their contributions to this work. These include Jerry Hughes, Brian Labombard and John Rice all of whom have most generously contributed data that were used in this thesis. In addition, the ICRF group, notably Steve Wukitch and Yijun Lin deserve special recognition as do the C-Mod physics operators: Bob Granetz, Jim Irby, Earl Marmar, Prof. Ron Parker. The PSFC staff are an amazing and dedicated group of people who have helped me tremendously. I need to thank Corrine Fogg, Dragana Zubcevic, Ed Fitzgerald, Felix Kreisel, Gary Dekow, Henry Bergler, Josh Stillerman, Lee Keating, Mark London, Matt Fulton, Nancy Masley, Paul Rivenberg, Rui Vieira, Sam Pierson, Tim Davis, Tom Fredian, Valerie Censabella, and primarily Jessica Coco. Much gratitude is due to William Burke and William Parkin who provided invaluable help in the design and construction of the new diagnostic.

I would also like to acknowledge all of my fellow graduate students who have shared with me all the strife and beer of the last six years and made my time at C-Mod more memorable, at times more bearable: Aaron Bader, Brock Bose, Arturo Dominguez, Eric Edlund, Zachary Hartwig, Nathan Howard, Jinseok Ko, Liang Lin, Kenneth Marr, Yuri Podpaly, Andrea Schmidt, Jason Sears, Noah Smick, Gregory Wallace. A special acknowledgment is due to my favorite officemates: Arturo Dominguez, the single most energetic, most irritating and most fun person with the awful Colombian sweets I have met (so far), and Nathan Howard, who taught me everything I ever wanted to know about fly-fishing – and everything I never knew I never knew.

Dear Mia, thank you for staying up all night so often and for helping me when you did to finish my thesis.

Last but far from least, Mia, Kat, Susan, Hui-Ying, Jonas, Ari, Paul, John and Kirk: here is to the simple life.

Contents

List of Figures

List of Tables

Chapter 1

Introduction

The study of turbulence is an area of research that has not only stimulated scientific investigation of fluids for hundreds of years but has also been becoming gradually more important in the field of magnetically confined fusion due to the decisive role turbulent processes play in plasma transport. All known laboratory plasmas exhibit turbulence both in the core and strongly in the edge (surface) region.

In the context of research toward controlled fusion, it has been known since at least as early as the mid 1970's or early 80's [7, 8, 9] that both the energy and the particle loss rate are much faster than what classical collisional transport theory calculated for curved magnetic field geometries, in particular the tokamak geometry (the so-called *neoclassic* theory), which is the plasma scenario under consideration for this thesis. These losses that cannot be accounted for in the neoclassic theory are commonly referred to as due to "anomalous" transport. Anomalous transport has generally been attributed to microturbulence (i.e. incoherent fluctuations at a scale much smaller than the plasma radius).

The focus of this thesis work – the turbulence of the edge and scrape-off-layer region (defined below) of laboratory plasmas – is important for the following reasons

1) any exchange of energy or mass between the plasma and the external world needs to happen through this boundary. Therefore controlling edge confinement may "seal" the interior plasma, allowing higher temperatures or densities to be

achieved;

2) in the far scrape-off-layer (SOL) where turbulence phenomena are manifested as coherent emission structures, they are decidedly the dominant transport process;

3) these filamentary structures play a significant role in determining the SOL density width, the plasma-wall interaction and possibly the robust experimental density limit[10];

4) beyond the transport of mass and energy, a better understanding of the formation of turbulent structures at the surface of the plasma is likely to give new insights into other currently studied transport processes such as the so-called spontaneous rotation and anomalous momentum transport [11, 12, 13, 14] and finally,

5) one of the most drastic transport-related effects in tokamak plasmas, the low- to high-confinement phase transition (L-H transition) [15] is now widely accepted to be caused by either a suppression of the edge turbulence or the radial decorrelation of transport enhancing turbulent eddies, i.e. the suppression of turbulence-related transport in any case.

Since the (edge) turbulence and its anomalous transport properties in tokamaks bear such an enormous importance, there has been a considerable effort both in the theoretical and the experimental fields to describe and predict these features of confined plasmas. Yet, despite many cases of partial agreement of some theories with a restricted set of observations, no theoretical model of turbulent transport has reliably predicted tokamak performance. What is required of a theory of turbulence in a tokamak plasma can then be summarized as follows:

a) It must provide a – most likely microscopic – theory for the source of the observed fluctuations, i.e. an instability of the tokamak plasma. Historically, this has largely been prevented by the fact that, in most cases, the fluctuations are broadband and it is therefore difficult to identify their source scale and hence the underlying instabilities.

c) It must explain the way the spectral distributions of the defining fluctuation quantities are formed (e.g. a broad spectrum of instabilities, wave-wave interactions, nonlocal transfer or any other spectral transfer process, and damping), as well as the level at which they appear. And finally:

c) it must predict the transport rate of the key macroscopic quantities, such as density n_e, energy (temperature) T_e, angular momentum Rv, etc, resulting from a) and a).

1.1 Thesis Goal and Outline

The primary objective of this thesis was to provide the experimental groundwork for such a study of edge turbulence on Alcator C-Mod. Specific objectives are 1) to make measurements of the edge and SOL turbulence in especially fine detail, 2) to examine the structure of the density fluctuation and velocity-field, 3) to measure the spectral characteristics of the turbulence thereby identifying any significant spatial and time scales of fluctuations, and 4) to connect each of the above to specific operating parameter ranges and the transport properties these regimes exhibit.

For this purpose, a new gas-puff-imaging system was designed and constructed for the study of edge fluctuations, greatly enhancing the time resolution, spatial coverage, sensitivity and signal-to-noise ratio of the imaging fluctuation diagnostics previously installed on Alcator C-Mod. In addition, the required sophisticated data analysis techniques were developed and implemented specifically for the new, fast, two-dimensional APD-based gas-puff-imaging system. The thesis reports the results obtained from this diagnostic and the data analysis from a wide range of plasma conditions, and is structured as follows.

The rest of this chapter gives a very basic description of tokamaks, concentrating on the terminology necessary to understand the chapters that cover the main results, and introduces the Alcator C-Mod device.

Chapter 2 provides some background on the previous experimental work on edge turbulence, concentrating on the points that the main results of this thesis connect

to – either by showing similar results and refining them, or contrasting them with observations specific to our application. The second section of the chapter discusses the significant transport-related trends found in Alcator C-Mod and other tokamaks, such as the Greenwald density-limit [10] and the concrete measurements of edge particle fluxes in Ohmic L-mode plasmas of various densities. In the end, historically important turbulence models are mentioned in order to explain the typical normalizations used throughout the main text and explain the basic concepts of turbulent transfer on which we rely.

Chapter 3 explains the principles of the diagnostic method applied and details the design of the new detector system, as well as the region observed in this study.

Measurements of edge and SOL turbulence spectra, propagation velocities and their trends in Ohmic L-mode discharges are presented in Chapter 4 and compared to H-mode discharges. First, the general findings from L-mode plasmas are introduced, which also provides some background for the H-mode experiments and motivation for concentrating on the turbulence of the edge region. In particular, the edge turbulence is shown to respond quite sensitively to plasma density. Then results from H-mode experiments are used to present further evidence for the connection of edge turbulence (i.e. turbulence just inside the LCFS) and cross-field particle transport, by showing that the different confinement regimes have specific "fingerprints" in the dispersion relations of the observed turbulence. The results are organized in order of sophistication of the analysis methods, and the physical insight gained through these analyses. They proceed from the relatively simple analyses of the time history of emission from a single viewing spot, to the bispectral analysis of 2D signals, which leads to *the first detection of spectral transfer* made using any diagnostic on C-Mod. The connections to the results of the other analysis methods are emphasized in an attempt to draw a coherent physical picture.

In Chapter 5 the trends found in the chapter on the main results are discussed in view of theory-relevant scales and quantities. This leads to the explanation of the most significant paths of further improvement on the turbulence analysis techniques.

Finally the major findings from Ohmic L-mode plasmas are summarized, includ-

ing the important connections found to the modelike plasma oscillations of the most common C-Mod H-mode, and are related to the trends found in the SOL. The summary closes with some comments on future directions of research and on applications of the diagnostic to fluctuations not directly related to turbulence characteristics, some of whose results are offered in the appendices.

1.2 Tokamak

All magnetic confinement scenarios of plasmas are based on the fact the Lorentz force will make charged particles gyrate in a plane perpendicular to the magnetic induction lines (field lines) in the region. If the magnetic field is sufficiently strong, this can stick the particles onto tightly wound helical orbits along the field lines. Early research on magnetic confinement of plasmas was conducted on linear devices, in which the magnetic field was provided by solenoid coils. Because the magnetic field would not prevent particles from freely streaming parallel to the field lines, this scheme always presented an issue about how to "seal" the two ends of the magnetic configuration. Eventually, and roughly at the same time, Lyman Spitzer in the US and Igor Tamm and Andrei Sakharov in the Soviet Union came up with the idea of bending the straight field lines of the solenoid into circles and forming a torus [4]. Since most modern fusion devices have this shape, it is important to introduce the common terms and notations of toroidal geometry (Figure 1-1).

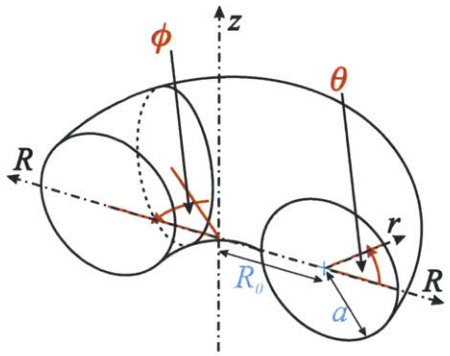

Figure 1-1: A torus cut in half; notations for toroidal geometry

A torus is a surface of revolution (or sometimes the space it encloses) generated

by revolving a circle (or another, non-intersecting, closed plane curve) about an axis that does not touch the circle but is coplanar with it. This means a circular torus is the Cartesian product of two circles, a large one and a small one, and in Cartesian coordinates it can be written in the parametric form:

$$x = (R_0 + a\cos\theta)\cos\phi$$
$$y = (R_0 + a\cos\theta)\sin\phi$$
$$z = a\sin\theta,$$

where the radius R_0 of the large circle is called the *major radius*, the radius a of the small circle is called the *minor radius*, the direction following increasing ϕ (fixed θ), that is around the symmetry axis, is referred to as *toroidal*, while the direction following increasing θ (fixed ϕ) is referred to as *poloidal*. The ratio a/R_0 is known as the aspect ratio, typically $1/3$ for a standard tokamak (a typical bicycle tube has an aspect ratio of $\sim 1/20$, a bagel features a large $2/3$). There are two coordinate systems that are commonly used to describe locations in the torus: the familiar cylindrical coordinate system (R, ϕ, z), where we start z in the plane of the center of the small circle – or in a magnetic device, the *magnetic axis* – which is often called the midplane. In this parametrization, the distance R from the axis of symmetry is still usually called the major radius (of the location, as opposed to the torus), as is ϕ still referred to as the toroidal angle. Another commonly used coordinate system is (r, ϕ, θ), where the distance r from the center of the smaller circle in its plane is still referred to as the minor radius.

Unlike in an infinite straight solenoid, the magnetic field from toroidal field coils is not constant inside the coils, as application of Ampère's law with a loop that runs in the toroidal direction will show, but rather drops as $1/R$. The part of the torus closer to the symmetry axis is therefore often called the high-field-side (HFS) or inboard, while the part on the "outside" of the torus is referred to as the low-field-side (LFS) or outboard.

Soon after the conception of toroidal devices it was found that a simple toroidal

field confines a plasma poorly because of particle drifts. A force acting on a charged particle perpendicular to the magnetic field causes its center of revolution (the so-called *guiding center*) to drift perpendicular to both the field and the external force, as can be easily verified via integration over a rapid revolution around the field line supposing that the external force is steady. If the force is opposite in direction for opposite charges, it will move them together, if it is the same, it will move them in opposite directions. The curvature of the magnetic field in a torus causes opposite charges to drift apart (up and down) and the electric field thus set up causes them all to drift away from the symmetry axis.

The Russian design of the toroidal magnetic confinement device is known as the *tokamak* a Russian acronym for "toroidal chamber with magnetic coils". It overcomes the above problem by driving a current I_p in the plasma inductively (or in modern experiments partially through waves), which generates a poloidal magnetic field. The helical twist to the field lines makes an electrical connection betwen the top and the bottom of the plasma, effectively shorting out the electric field which would drive the plasma into the wall of the vessel. The measure of how tightly the field is wrapped around the torus is called the safety factor q; it denotes the number of times a magnetic field line goes around toroidally for each time around poloidally. The helical field lines wrapping around the torus eventually map out a surface known as a *flux surface.* An important quick measure of the magnetic configuration is q_{95}, the safety factor on the flux surface which includes 95% of the magnetic flux. If the flux surface intersects a solid structure such as the vacuum vessel, it is called an open flux surface, while flux surfaces not contacting a solid structure are closed flux surfaces. The boundary between these two regions is known as the *separatrix* or last closed flux surface (LCFS). In modern tokamaks, the LCFS is formed through special shaping fields which cause some open field lines to touch the material surfaces in a closed region at the top or the bottom of the vessel, called the divertor. This forms a null-point of the poloidal magnetic field, called the X-point, somewhere on the LCFS. If this point is at the top (bottom) of the configuration, the geometry is referred to as upper-single-null or USN (lower-single-null, LSN); if both the top and the bottom

of the LCFS feature a neutral point, the geometry is a double-null (DN).

This design is to date the most promising magnetic confinement concept for fusion applications and there are on the order of $\sim$ 20 major tokamak experiments all around the world today, conducting research into the physics of fusion grade plasmas.

1.3 Alcator C-Mod

The experimental studies reported in this thesis were conducted on the Alcator C-Mod [1] tokamak, located at the Plasma Science and Fusion Center, MIT. Alcator C-Mod is a compact, high magnetic field, high density, shaped, diverted tokamak. Although it is a relatively small device compared to other currently operating tokamaks, and indeed about 10 times smaller than ITER [16], the first tokamak designed specifically to burn a fusion plasma at high gain, Alcator is particularly well suited for fusion research due to its high magnetic field which allows it to reach plasma temperatures and densities, and scale lengths that are relevant for even a reactor-like operation such as ITER. Figure 1-2 shows a cross section of Alcator C-Mod with the LCFS of a typical, LSN D shaped plasma, and the most important parameters that characterize the system are listed in Table 1.1.

Table 1.1: Alcator C-Mod device parameters

Parameter	**Value**
Major Radius R_0	0.67 m
Minor Radius a	0.21 m
Toroidal Fielda B_T	$2.6 - 8.1$ T
Plasma Current I_p	$0.4 - 2$ MA
Ion Cyclotron Heating P_{RF}	6 MW
Electron Density n_e	$1 \times 10^{19} - 1 \times 10^{21}$ m^{-3}
Core Electron Temp. T_e	≤ 9 keV
Pulse Length	1-3 s

The magnetic field in Alcator C-Mod is generated by conventional copper coils, which are cooled cryogenically. The coils are powered by an alternator combined with a 75 ton rotor. The frequency and length of pulses are determined by the amount

of time necessary to cool the coils to safe operating temperatures and spin up the rotor. The primary auxiliary heating in Alcator C-Mod is ion cyclotron resonance frequency (ICRF) waves launched from three antennas around the vessel. Recently, a lower-hybrid (LH) microwave source was installed to drive current noninductively and provide additional heating power.

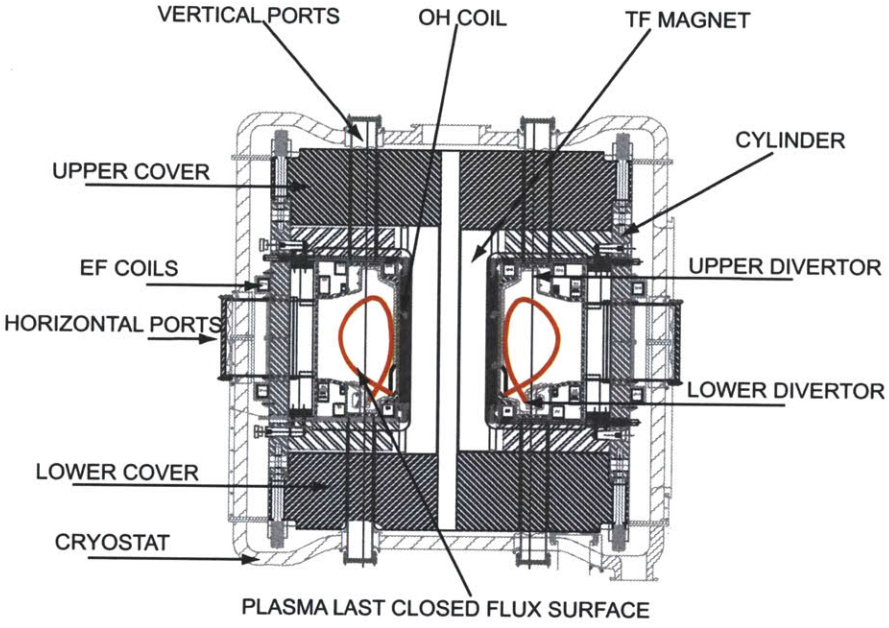

Figure 1-2: Horizontal cross section of the Alcator C-Mod tokamak

1.4 Operating Regimes

There is a wide range of conditions available for plasma operation on the Alcator C-Mod tokamak. The quality of the global confinement of energy in these plasmas varies greatly and is most often quantified by the *energy confinement time* τ_E, which represents the e-folding relaxation time of the energy stored in the plasma due to both conduction and other heat loss processes [17]. The sharpest boundary expressed in terms of τ_E is a transition between a low-confinement regime or "L-mode" and a high-confinement regime or "H-mode", where τ_E is about a factor of 2 higher than in the L-mode. In addition, particle confinement is also usually enhanced in the H-mode, leading to a quick increase in density of the confined plasma (cf. Figs. 1-3,1-4

and 1-5). This phenomenon has made the time history of the plasma density a good indicator of the confinement regime.

The H-mode is traditionally achieved with the use of auxiliary heating, i.e. not via the Joule heat of the plasma current, known as Ohmic heating, although in recent years Ohmic transitions have been produced. At a critical level of external heating power, the plasma undergoes a transition from L-mode to H-mode confinement on a sub-millisecond time scale. The transition was originally observed on the ASDEX tokamak [15], but has since been achieved on all major tokamaks. The power threshold of this abrupt transition depends on a number of integral quantities such as the plasma density, magnetic field strength and device size [17], as well as the magnetic geometry used. In particular, it has been found that if the ion $\mathbf{B} \times \nabla B$ drift is towards the X-point, the auxiliary power necessary to induce a transition can be about a factor of 2 lower than in a geometry where the drift is away from the X-point. The underlying physics of the L-H transition, and consequently its scaling properties are not yet explained thoroughly.

The main part of this thesis focuses on the characteristics of the fully developed turbulence in the edge of L-mode regimes. Yet, it is unavoidable to touch upon the characteristics of the edge fluctuations of some of the high confinement regimes. Indeed, there is a number of confinement regimes that are observed on the Alcator C-Mod tokamak.

First the high confinement regime most common in tokamak devices, the so-called ELMy H-mode will be described. Then the two quiescent H-modes most typical of C-Mod operation, the Enhanced D-Alpha H-mode and the ELM-free H-mode will be covered, their characteristics used in the analysis summarized; then a more recently accessed and studied regime, the I-mode will be introduced.

1.4.1 ELMy H-mode, ELMs

Steep edge-pressure gradients are the defining feature of the H-mode confinement regime. This steep gradient region, the 'pedestal', is, in general, not stable since it can be the free energy source for many modes, and even in the case when these modes

are stabilized, the plasma suffers a radiative collapse explained in the section on ELM-free H-modes. Edge-localized-modes (ELMs) [18] are instabilities that are typically responsible for periodically relaxing the steep pressure gradients at boundaries of tokamaks on a fast (< 1 ms) time-scale. In such explosive events, usually referred to as ELM "crashes", which appear as sharp spikes in the Dα signal in Fig. 1-3, a significant amount of both particles and heat leave the main plasma, a serious consequence of which is the large transient heat load on the divertor plates.

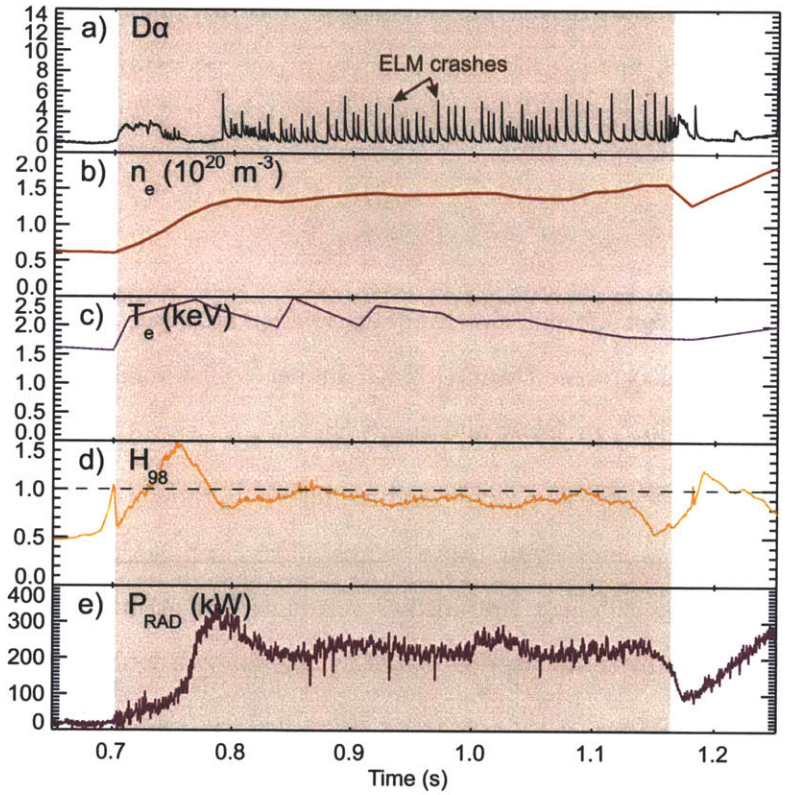

Figure 1-3: Characteristics of a typical ELMy H-mode regime with a heating power of $P = 2$ MW. Confinement relevant plasma parameters; a) Dα brightness (a.u.), b) line averaged electron density, c) central electron temperature, d) H_{98} confinement factor [4], e) radiated power.

The problem is so serious that it threatens to limit the lifetime of these components in burning plasma experiments. Characterizing and understanding the ELM phenomenon is also complicated by different manifestations of ELMs. The title of this section as one referring to a separate confinement regime is therefore somewhat

inaccurate. In fact, there is an entire zoology of ELMs – Type I (giant), Type II (grassy), Type III, etc.

ELMs are not the typical relaxation mechanism for the H-mode edge-pedestal on Alcator C-Mod, although Type II ELMs and larger Type III ELMs are occasionally observed in some kinds of discharges. Yet, in the past few years an operational space has been accessed in C-Mod for which discrete, relatively large ELMs are the relaxation mechanism for the pedestal. This operational space is one of large triangularity for the lower half of the plasma ($\delta_{lower} > 0.75$), small upper triangularity ($\delta_{upper} \approx 0.15$), and a normalized collisionality in the pedestal $0.2 < \nu^* < 1$. The normalized collision rate or collisionality is defined as

$$\nu^* = \frac{qR\nu_{ei}}{\epsilon^{3/2} v_{t,e}}, \tag{1.1}$$

where ν_{ei} is the electron-ion collision frequency, ϵ is the aspect ratio and $v_{t,e}$ is the thermal velocity of electrons. Plasmas with higher collisionalities typically exhibit EDA H-mode (see below) or EDA and small ELMs.

It is not our purpose here to provide minute details on the nature of the instabilities or their characteristics, not even those which have been added to the vast body of literature on ELMs through the studies conducted at Alcator C-Mod. We will therefore highlight only those aspects of ELM phenomena which were explored by our new diagnostic.

The type of the ELMs in C-Mod plasmas is, as yet, not clear. Yet, our previous studies have shown that (1) the T_e pedestal height can be $\approx$ 900 eV (pedestals this hot are typical of Type I), (2) this pedestal is usually not completely destroyed in the crash and (3) *there is a precursor oscillation* to the crash event (typically present for Type III and some Type I). The current paradigm of ELMs asserts that the events arise from a coupled peeling/ballooning instability for modes at an intermediate toroidal mode number n. Previous observations on Alcator C-Mod, including those made by magnetic pick-up coils and an older version of GPI diagnostic, typically show a pre-crash oscillation. They usually have a relatively long (up to 300 μs) period of stable

oscillation between $150 - 450$ kHz, and as magnetic measurements have shown, an intermediate toroidal mode number $5 < n < 15$ [19].

1.4.2 EDA H-mode

Enhanced D-alpha (EDA) H-modes are one of the most common types of H-modes run on C-Mod. They are quiescent H-modes without explosively unstable Edge Localized Modes (ELMs) [18], characterized by increased particle transport through the edge relative to ELM-free H-modes, which are more commonly accessible on other tokamaks. This increase in edge transport can be most readily observed in the increase of Dα emission during the H-mode period (see Fig. 1-4).

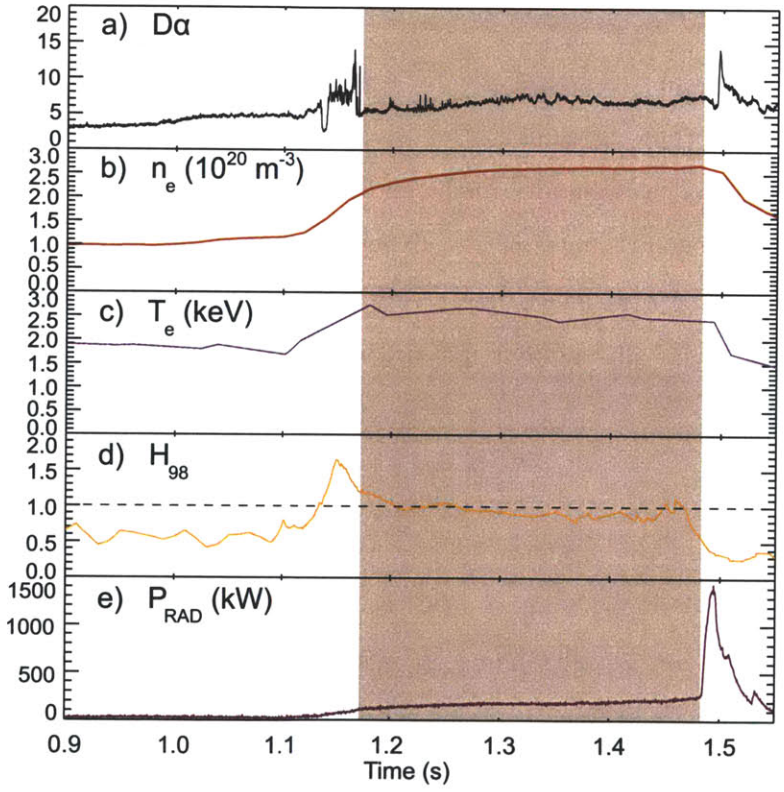

Figure 1-4: Characteristics of a typical EDA H-mode regime with a heating power of $P = 2.5$ MW. Top: Confinement relevant plasma parameters; a) Dα brightness (a.u.), b) line averaged electron density, c) central electron temperature, d) H_{98} confinement factor, e) radiated power.

The enhanced particle transport has been correlated with a quasi-coherent mode

(QCM) observed on the density and magnetics fluctuations at frequencies between 50 and 200 kHz [20]. The QCM develops shortly after the formation of the edge pedestals, is localized to the electron density pedestal and is likely the result of a resistive ballooning instability [21]. It is believed to be the mechanism that prevents impurities from accumulating in the core. The increased particle transport allows for steady state H-mode operation with constant radiated power, density, temperature, and confinement. Figure 1-4 shows these parameters for a typical EDA H-mode. The QCM, and thus EDA H-modes, are only observed in high collisionality plasmas, typically $\nu^* > 1$ at the top of the pedestal.

1.4.3 ELM-free H-Mode

ELM-free H-modes are characterized by a strong particle transport barrier due to the lack of macroscopic instabilities of the edge. This barrier results in impurity accumulation during the H-mode. In the high temperature ($T_e \gtrsim 10$ keV) core plasma small nuclei (up to and sometimes even beyond carbon or oxygen) are completely ionized and even larger nuclei exist at a very high degree of ionization. Consequently, the main plasma generally radiates due to Bremsstrahlung, whose radiation power is [22]

$$P_{\mathrm{BS}} \propto n_e T_e^{1/2} \sum_i n_i Z_i^2, \tag{1.2}$$

where n_e and T_e are the electron density and temperature, and n_i and Z_i are the number density and charge number of the i-th ion species. Thus, the rate of energy loss through radiation rapidly increases with the effective atomic number Z of the plasma. Therefore ELM-free H-modes are inherently transient in nature, since an accumulation of impurities eventually causes a radiative collapse of the plasma. Both the plasma and impurity density increase monotonically during ELM-free H-modes, while T_e, T_i, and energy confinement peak early and then degrade as a result of the increasing radiated power. Indeed, as the radiated power approaches the input power, the plasma energy confinement and temperature pedestal both decline[23]. These characteristics are shown in Fig. 1-5.

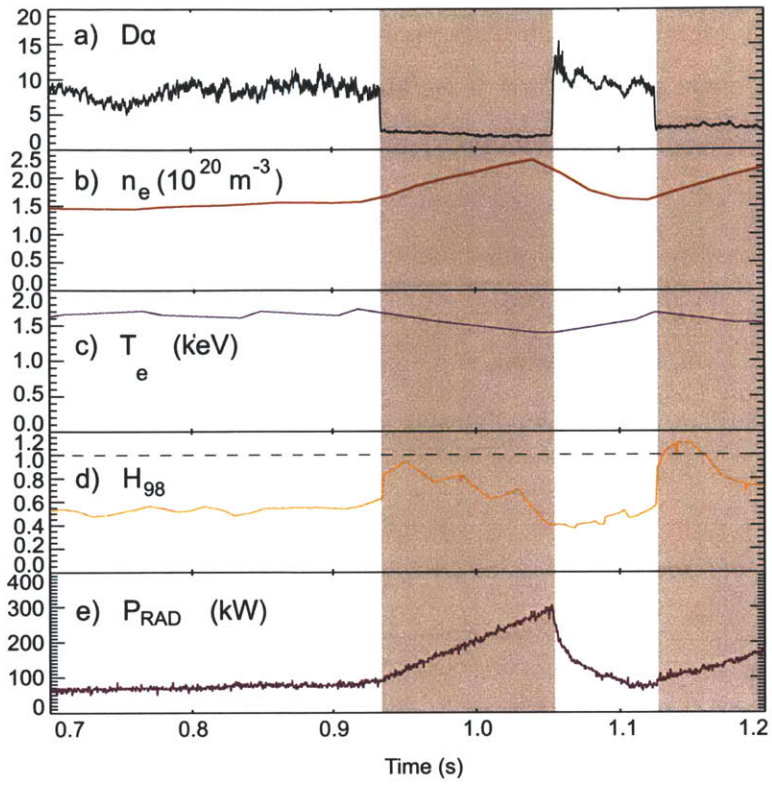

Figure 1-5: Characteristics of a typical ELM-free H-mode regime with a total heating power of up to $P = 0.9$ MW. Top: Confinement relevant plasma parameters; a) Dα brightness (a.u.), b) line averaged electron density, c) central electron temperature, d) H_{98} confinement factor, e) radiated power.

1.4.4 I-mode

C-Mod discharges with the X-point in the unfavorable ion $\mathbf{B} \times \nabla B$ drift direction with input power just below the H-mode threshold have been observed to exhibit a slow evolution prior to L-H transitions[24]. In recent years, this motivated research into developing this transient period into an operational regime that can persist for many energy confinement times [6]. The developed regime is characterized by an L-mode-like edge particle barrier, but an H-mode-like energy barrier and has been termed an 'improved L-mode', or 'I-mode'. In I-mode the plasma density increases modestly coincident with the application of ICRF power, but does not increase further or approach its H-mode values. The plasma temperature, however, approaches and maintains close to its full H-mode value during the I-mode period. The most relevant

confinement characterizing quantities can be seen in the traces shown in Fig. 1-6. The I-mode electron temperature pedestal approaches a full H-mode pedestal, while the electron density pedestal remains significantly closer to L-mode levels.

The steady state operation in I-mode is associated with an edge turbulence structure observed on the density and magnetic fluctuations with a frequency around $100 - 300$ kHz. This broad spectral feature appears to be similar to the QCM observed in EDA H-mode operation, but exists at much lower collisionality ($\nu^* < 1$) and is spread over a wider frequency range, and has hence been referred to as the "Weakly Coherent Mode" (WCM).

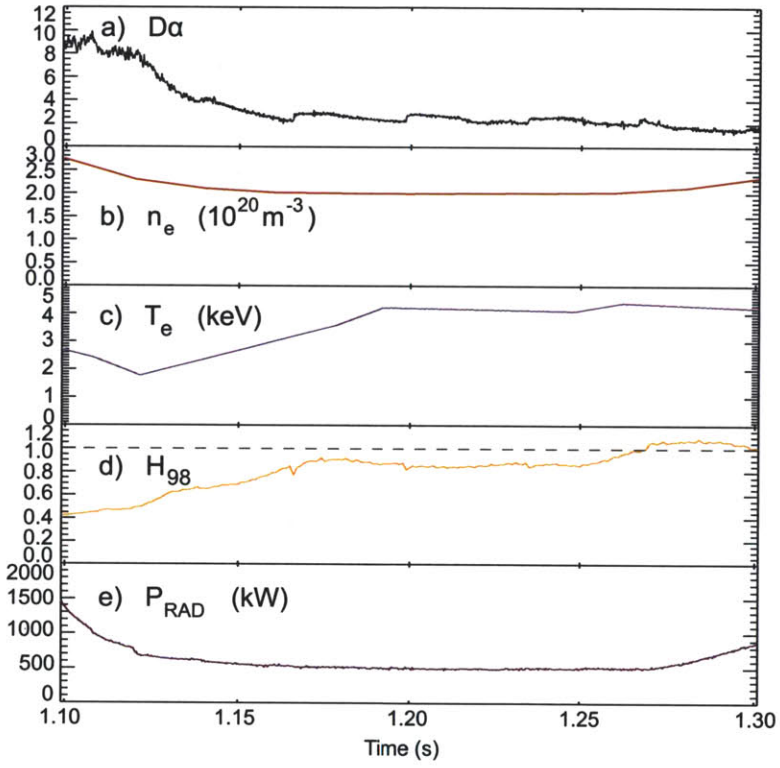

Figure 1-6: Characteristics of a typical I-mode regime with a heating power of $P = 4.3$ MW. Top: Confinement relevant plasma parameters; a) Dα brightness (a.u.), b) line averaged electron density, c) central electron temperature, d) H_{98} confinement factor, e) radiated power.

Chapter 2

Edge Turbulence and Transport

This chapter provides some information on the previous experimental work in the field of tokamak edge turbulence, as well as measurements of the transport characteristics of the edge-SOL region in Alcator C-Mod L-mode plasmas. A very brief introduction to the models of plasma turbulence will also be presented, which we will call upon from time to time when interpreting the results reported in the main chapters of this thesis. The intention of this chapter is therefore not to present a review of these fields, but to briefly mention the specific details which will help motivate the present research and describe it within a broader context.

For a true review of experimental (and some theoretical) results on edge turbulence and transport, the reader is directed to one of the excellent and widely available comprehensive reviews: [25, 26, 27]

2.1 Tokamak Experiments

Much of the pioneering experimental work and analysis in the field of tokamak edge turbulence was done on the Texas Experimental Tokamak (TEXT) [28, 29], on the ATC[30], Caltech[31] tokamaks. This section gives a short summary of the various characteristics that were measured in those earlier experiments. Some of the results are cleanly reproduced at Alcator C-Mod, while others show interesting new features, some due to the methods developed for this thesis.

Starting from the first observations of low frequency microscopic turbulence in tokamaks, the fluctuations have shown a broad spectrum in frequency, not only in the density fluctuation field but also in the electric potential and in some cases even the magnetic field perturbations. The exact range of frequencies varied from one device to the next, nevertheless the range of wavenumbers measured (wherever applicable), was similarly broad.

In all regions of the tokamak plasma, the overwhelming majority of the spectral energy was carried by fluctuations $k_\perp \rho_s < 1$, where $k_\perp$ is a wavevector perpendicular to the magnetic field – as can be expected from drift-wave-like turbulence. This normalization and the expected drift-behavior will be explained in Section 2.3. In addition, in specifically the edge region, $k_\perp \rho_s < 0.15$ was shown to be dominant, and spectral shapes were generally broadband and monotonically decreasing with increasing frequency (wavenumber), showing no modelike structures. The specifics of the spectral shapes have generally been addressed in terms of broad statistical terms only.

Ever since these early experiments, the edge region has been known to be considerably more turbulent than any other part of the plasma, showing a $10 - 100$-fold increase of $\tilde{n}/n$, as compared to the core. The scaling of the total fluctuation level with plasma density was studied quite extensively, with various results. In many cases, the $\tilde{n}/n$ in the edge was found not to depend on $\bar{n}_e$ at all, such as in the Caltech tokamak or the PLT. Later, strong gas-puffing *was* in fact shown to cause a clear increase in fluctuation power on PLT.

The direction of poloidal propagation of the edge turbulence has been an interesting issue. In measurements, where the region spanning the LCFS was carefully scanned with good spatial resolution, such as in the Caltech tokamak [31] and TEXT [29], probe measurements showed that the turbulence moved in the ion diamagnetic direction far out from the core, but changed to the electron direction further in. The regions were never sharply separated, and the velocities were observed to transition smoothly from one direction to the other.

2.2 Preliminaries on Ohmic Transport

The purpose of this section is to describe the particular cross-field particle transport trends found on Alcator C-Mod. This is a crucial step in the work delineated in the section on the goals of this thesis. The first key phenomenon to note, however, is an apparently universal result, occurring not just on C-Mod. In addition to the operational limits imposed by basic stability considerations (on I_p and $n_e T_e$, etc.), an independent limit on plasma density has been observed in confined toroidal plasmas. In tokamaks, the most common form of this empirical scaling law is written as [32]:

$$n_G = \frac{I_p}{\pi a^2}, \tag{2.1}$$

where if I_p is in units of MA, and a is in units of m, n_G denotes the upper limit on the attainable density in units of 10^{20} m^{-3} before a disruptive discharge termination occurs. There is some evidence linking the limit to physics near the plasma boundary; a peaked density profile and hence additional particles in the plasma core do not seem to affect the limiting physics. Theoretical work has concentrated on increased levels of radiation which at a high enough density may dominate power balance. These theories are admittedly problematic and are typically not fully consistent with experimental results. A separate thread of research looks for the cause in collisionality enhanced turbulent transport, but the understanding of the underlying mechanisms is as yet, insufficient.

In terms of direct evidence of edge transport phenomena, research at the Alcator C-Mod has been conducted to study the behavior of edge plasma transport, profiles and flows over a wide range of plasma conditions, spanning several run campaigns [33, 34, 5]. Most importantly, line-averaged density ($\bar{n}_e$) scans were performed at various combinations of I_p and B_T, with a range of variation $0.1 < \bar{n}_e/n_G < 0.5$. Figure 2-1, reproduced from Ref. [5] summarizes the results most important for this thesis. In Fig. 2-1(a) the response of density profiles to increased line-averaged density illustrates some of the transport trends. A steep gradient region is found even in L-modes at the LCFS, which persists even as $\bar{n}_e/n_G$ is raised using strong gas-puffing,

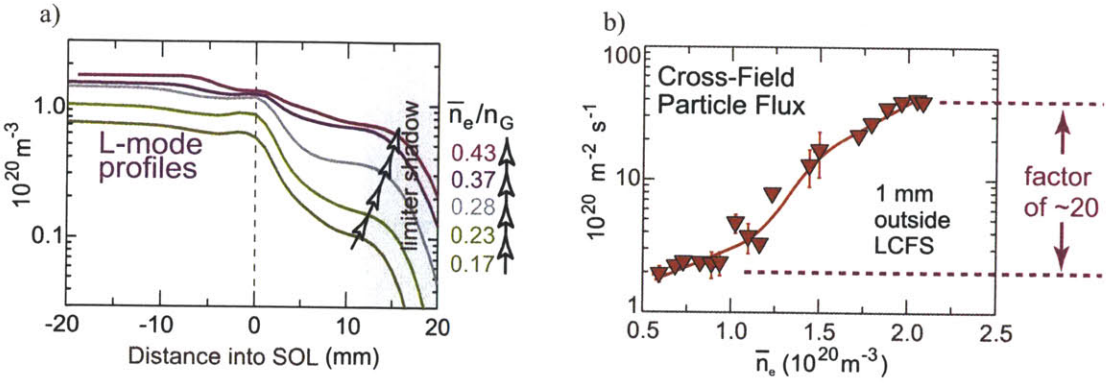

Figure 2-1: Reproduced from Ref. [5]: a) composite density profiles assembled from probe and Thomson scattering diagnostics for Ohmic L-mode discharges; b) cross-field particle flux densities at a location $\sim$ 1 mm outside the LCFS vs line averaged density.

yet the SOL fills in, so that the density ratio between the closed and open field lines actually drops. Even higher densities cause the density at the separatrix to drop as intermittent features, normally seen only in the near SOL intrude into the closed field line region. All the above in itself is evidence for an explosive growth of cross-field transport with increasing $\bar{n}_e/n_G$, but to make the claim stronger, Ref. [5] tracked the changes in cross-field particle transport directly, as is shown in Fig. 2-1(b). The figure shows that cross-field particle flux densities in the L-mode edge grow nonlinearly (almost exponentially) with plasma density, exhibiting a factor of $\sim$ 20 increase over the range $0.12 < \bar{n}_e/n_G < 0.5$, whch increased by only a factor of $\sim$ 4.

2.3 Models of Plasma Turbulence

The first notable theoretical attempt at explaining the spectrum of plasma turbulence was that by Hasegawa and Mima [35]. Here we will describe the main features of this model, not because it is directly relevant – it has been shown not to directly apply to tokamak turbulence, and edge turbulence in particular – but because through it the most fundamental concepts of the drift wave turbulence, such as the basic spectral transfer terms, and the length normalization it motivates, can be introduced. The Hasegawa-Mima model was a very simplified model of drift wave turbulence, treating

the entire turbulence as fluctuations of a *single field* (the electric potential) in two dimensions. The model has no sources or sinks, i.e. it only describes freely decaying turbulence, from a "manually" inserted scale. It operates under the assumptions that a) the background magnetic field is homogeneous and strong (the rate of change of anything is slower than the ion Larmor precession), b) ions are cold (therefore the thermal balance equation is not considered, and the ion-pressure is dropped), c) electrons respond to the perturbed electric field adiabatically, therefore the Boltzman-equation is satisfied:

$$\frac{\tilde{n}}{n} = \frac{e\phi}{T_e}. \tag{2.2}$$

From these assumptions, using the fluid equations, the following can be derived. First of all, since the d/dt is small, the changes to the electric field only appear as a polarization drift, therefore the full velocity vector is the $\mathbf{E} \times \mathbf{B}$ velocity $\mathbf{v}_E$ and the polarization drift.

$$\mathbf{v} = -\nabla\phi \times \frac{\mathbf{B}}{B_0^2} + \frac{1}{\Omega B_0}\left[-\partial_t \nabla_\perp \phi - (\mathbf{v}_E \cdot \nabla_\perp)\nabla_\perp \phi\right], \tag{2.3}$$

where Ω is the ion cyclotron frequency. Note that the polarization drift (the second term) is much smaller than the $\mathbf{E}\times\mathbf{B}$ drift (the first term) due to the condition on slow variations ($d/dt\Omega^{-1} \ll 1$), but it is kept because unlike the latter, the polarization drift is not divergence-free. Using this velocity expression, and considering small potential perturbations, such that $\ln n \approx \ln n_0 + e\phi/T_e$ for the Boltzmann-equation, we obtain

$$\left[\partial_t - \nabla_\perp \phi \times \frac{\mathbf{B}}{B_0^2} \cdot \nabla\right]\left(\frac{1}{\Omega B_0}\nabla_\perp^2 \phi - \frac{e\phi}{T_e}\right) - \nabla_\perp \phi \times \frac{\mathbf{B}}{B_0^2} \cdot \nabla \ln \frac{n_0}{\Omega} = 0. \tag{2.4}$$

At this point the equation can be made dimensionless, by using the natural units $(e/T_e)^{-1}$ for ϕ and Ω^{-1} for time. This leaves us with the normalized spatial coordinate

$$\tilde{x}^2 = x^2 \frac{e}{T_e}\Omega B_0 = x^2 \Omega^2 \frac{m_i}{T_e}, \tag{2.5}$$

where $\Omega = eB_0/m_i$ was used. This motivates introducing the length units of

$$\rho_s = \sqrt{\frac{T_e}{m_i}}\frac{1}{\Omega} = \frac{c_s}{\Omega} \tag{2.6}$$

where ρ_s is the drift scale, which is the ion gyro-radius at the sound speed c_s. This means that the H-M equation has a characteristic scale length inherent to it. Note also that with these normalizations, the dimensionless fields are $\tilde{n} = \tilde{\phi}$. With these normalizations, the dimensionless Hasegawa-Mima equation is

$$\partial_t(\nabla^2\phi - \phi) - [(\nabla\phi \times \hat{z}) \cdot \nabla]\left[\nabla^2\phi - \ln\frac{n_0}{\Omega}\right] = 0, \tag{2.7}$$

where $\hat{z}$ is the unit vector parallel to the magnetic field. Most importantly, notice that the second term is nonlinear in ϕ: this term is what provides the spectral transfer through coupling of waves at different wavelengths. In particular, Fourier-transforming Eq. (2.7) yields

$$\frac{d\phi_{\mathbf{k}}}{dt} + i\omega_{\mathbf{k}}\phi_{\mathbf{k}} = \sum_{\mathbf{k}=\mathbf{k}_1+\mathbf{k}_2} \Lambda_{\mathbf{k}_1,\mathbf{k}_2}\phi_{\mathbf{k}_1}\phi_{\mathbf{k}_2} \tag{2.8}$$

where the matrix element $\Lambda_{\mathbf{k}_1,\mathbf{k}_2}$ can be directly calculated from the wavenumbers. The quadratic term in the above equation describes the interaction of wave triplets, whose wavenumbers form a closed triangle, i.e. conserve wave momentum. This is called the three-wave interaction. The model equation is very similar to regular 2D fluid turbulence with a generalized energy and enstrophy (average vorticity), except for the internal size scale ρ_s. The fluctuations following the Hasegawa-Mima equation are therefore expected to be similar to the Kolmogorov-Kraichnan spectrum [36] of 2D turbulence, at least at scales $k\rho_s \gg 1$.

The most important problem with the H-M equation was that it did not allow for any deviations from electron adiabaticity, therefore ignoring all density fluctuation dynamics. The so-called "$i\delta$" models [37] were invented to deal with this problem in an approximate way. They included no deviations from $|\tilde{n}| = |\tilde{\phi}|$, but intended to simulate the nonadiabatic electron response as $\tilde{n}_{\mathbf{k}} = \tilde{\phi}_{\mathbf{k}}(1 - i\delta_{\mathbf{k}})$. These models,

in addition to the polarization nonlinearity of the H-M equation, include the $\mathbf{E} \times \mathbf{B}$ nonlinearity arising from the convection of the nonadiabatic electrons.

Perhaps the very simplest approximation involving both potential and density fluctuation dynamics in the description of the turbulence, was due to Wakatani and Hasegawa [38]. In this form of the model, the ion-electron collisions were kept, therefore both dynamics could be included by using both the ion and the electron momentum equation. In a fashion completely similar to the above, they arrived at

$$[\partial_t - \nabla\phi \times \hat{z} \cdot \nabla] \nabla^2\phi = c_1(\phi - n) + c_2\nabla^4\phi \tag{2.9}$$

$$[\partial_t - \nabla\phi \times \hat{z} \cdot \nabla] (n + \ln n_0) = c_1(\phi - n). \tag{2.10}$$

The set of equations above are a consistent description of turbulence compared to the H-M equation, because they automatically contain a drive without the need to add external forcing terms. The solution gives a fairly sharply defined positive growth rate for the wavenumber range $k_\perp \rho_s \approx 1$. Physically, it is seen that adiabaticity is not exactly satisfied because of parallel dynamics in the electron momentum equation. This description still allows for an $i\delta$ approach though.

Even the H-W equations are only suitable for basic illustration of transfer physics. In reality, the parallel dynamics cannot be simplified to a constant factor as in c_1, the magnetic field is inhomogeneous, etc.

Modern models of the edge turbulence, such as the DALFT, DALF3, GEM, [39] relax the electrostatic approximation, since the normalized pressure (beta) of a real tokamak can easily be high enough to be important in the dynamics. They often consider curvature terms in the magnetic field, and include interchange dynamics, due to finite quasi-static compressibility. These models allow one to at least estimate the importance of certain effects, such as the interchange/ballooning, due to edge gradients or beta, or the kinetic Alfvén dynamics due to finite poloidal beta. We end the description of turbulence models here, since we have distilled the key points that will serve as background for the spectral transfer analyses of Chapter 4, i.e. how 3-wave non-linear coupling arises naturally in this regime and the strengths and weaknesses of (nearly) single-field models.

Chapter 3

Design and Construction of the Gas-Puff-Imaging Diagnostic

3.1 Gas-Puff-Imaging

Diagnosis of the light emitted by the plasma is highly favored in plasma physics (among other fields) because it provides an essentially non-perturbative method of observation. Even though the line radiation spectrum of highly or even nearly completely ionized plasmas (common in fusion devices) is typically not amenable to use for turbulence diagnoses on turbulent timescales, the use of visible light emission from tokamak plasmas for diagnostic purposes is well-established. Most devices used for these measurements cannot determine spatial localization since they measure brightness in a line integrated fashion. *Gas-Puff-Imaging* (GPI) is one of the most successful experimental approaches to the study of plasma turbulence, because it enables us to make spatially localized measurements without the need for tomographic systems.

The principle of the technique is almost the same as that of beam emission spectroscopy (BES): to inject a source of strong radiation – atoms or ions – from just outside the plasma. When this local gas puff is viewed with an optical system with lines of sight crossing the puff, the emission from the local puff will overwhelm any intrinsic radiation arising along the viewing chord, thus localizing the measurement to the zone where the neutral atoms are introduced. With a suitably built and placed

nozzle, this zone can be small in the toroidal dimension.

The diagnostic therefore does not directly measure electron density n_e fluctuations, but rather fluctuations in the local emission. The emissivity ε is mostly dominated by electron impact excitation of the artificially introduced neutral atoms, of density n_0, and can therefore be written as

$$\varepsilon \propto n_0 n_e \Gamma(n_e, T_e), \tag{3.1}$$

where n_e is the electron density, T_e is the electron temperature, Γ is the excitation rate coefficient. Importantly, it has been argued and tested that n_0 varies much more slowly than the frequencies of interest for turbulence measurements [40, 41]. Furthermore, the gas cloud dynamics were modeled for realistic scenarios [42], and it was shown for both deuterium (D_2) and helium (^4He) gas puffs, that for a wide range in both n_e and T_e, the emissivity is locally a power function of both:

$$\varepsilon \propto n_e^{\alpha_n} T_e^{\alpha_T}. \tag{3.2}$$

The exact variations, as determined by these models, are detailed in Appendix B. It is shown there that for the vast majority of edge fluctuations presented in this thesis, α_n is up to 5-6 times greater than α_T. Because of this, the measured fluctuations are still often regarded as ones determined nearly completely by the local density.

GPI has been a very successful diagnostic system on Alcator C-Mod [40, 41, 42, 43, 20] ever since its original installation and development by J. L. Terry and S. Zweben starting in 2000 [44]. Currently, there are several gas puff nozzles installed on C-Mod that are used for GPI: 1) at the outboard midplane mounted on the A-B limiter (four capillary tubes), 2) at the inboard midplane and 3) at the lower high-shear region just above the lower X-point on the low-field-side. Before this thesis work was done, the optical arrays viewing these gas puffs were coupled to essentially two kinds of detectors: linear arrays of fiber views coupled to PIN photo-diodes (so-called "fast-diode" systems) which in physical space had a ~ 4 mm spot size per fiber and were sampled at 1 MHz and viewed both the LFS and the HFS; and two coherent

fiber bundles that were coupled to fast-framing CCD cameras with $\sim$ 2 mm spatial resolution and a maximum frame rate of 150 kHz at the LFS midplane and lower high-shear region.

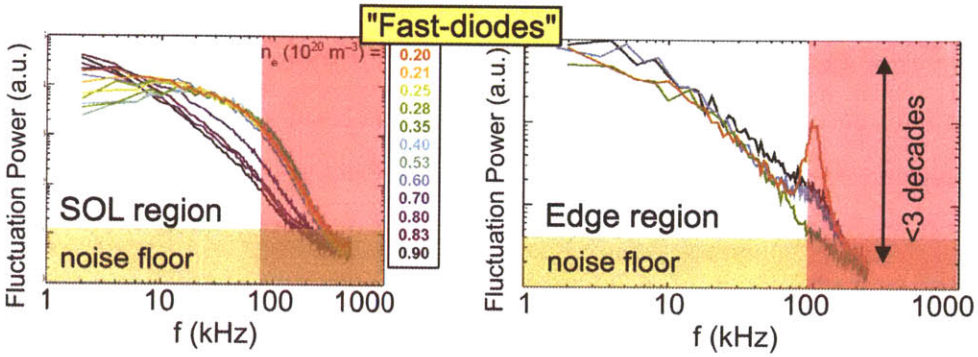

Figure 3-1: Spectra recorded with the PIN photodiode system with the problematic region (high noise levels in the edge) for the diodes shaded in brown and those for the CCD system (high frequency) shaded in red. The APDs overcome both problems (cf. Fig. 4-10).

Studies of the edge turbulence of Alcator C-Mod plasmas in L-mode, ELMfree H-mode and Enhanced D-Alpha (EDA) H-mode and even the recently established I-mode [6] operation had been hindered by limitations in each of the previous imaging systems (illustrated in Fig. 3-1). The Quasi-Coherent Mode (QCM), the phenomenon distinguishing the EDA from the ELM-free H-mode, has a typical fundamental frequency between 60 and 150 kHz, and the frequency associated with the scale of significant dynamic changes evidenced by slowly or abruptly changing spectral indices[1] in the edge-SOL turbulence appears to be 150 – 250 kHz. Thus the CCD cameras at sampling rates up to 200 kHz (or more recently 380 kHz) could not follow the dynamics of fast timescale features of these phenomena, such as the harmonic structure of the QCM (see Section 4.7), or the decay of the turbulence. The drawback of the PIN photo-diode system on the other hand was that it could only provide two one-dimensional, albeit perpendicular, series of views in a region where the motion of the plasma turbulence becomes fully two-dimensional, and therefore emission structures are often lost from their restricted fields of view. In addition, the radial dependence

[1]The rate of decay towards high frequency components, defined more accurately in Section 4.4

of quantities derived from poloidally resolved structures could be obtained only by scanning the plasma equilibrium across the single poloidal array of views.

The 2D fast CCD camera data provided no information in the red shaded regions even though data from the fast photodiode arrays have shown these regions are of great interest. On the other hand, the noise levels of the fast-diodes at low light levels prevent parameter fitting in the high frequency (small scale) regime of the turbulence in the plasma edge where light levels are always expected to be quite small (because of ionization by the hot and relatively dense edge plasma) compared to the region closer to the wall.

3.2 Technical Details of the Design

In designing a new GPI system we desired to overcome some of the shortcomings of the then-existing GPI systems. We desired (a) 2D coverage at the outboard midplane region where the strongest changes are expected in cross-field transport, (b) a time response covering the time-scales relevant to the study of turbulence as well as the modelike plasma responses found in the edge and (c) an improved light-level sensitivity, so that the low emission regions inside of the separatrix could be diagnosed. The first step in designing such a diagnostic was finding a suitable detector.

Maintaining the spatial resolution of the existing PIN photodiode system at $\sim$ 4 mm, yet expanding the views to full 2D coverage of the required region ($\sim$ 4 cm $\times$ 4 cm) meant the new system needed to consist of $\sim$ 100 views. The signal-to-noise ratios of possible detector arrays were estimated based on known average light intensities in the observation region and specifications. Figure 3-2 shows the results of this process for the top two contenders, a photo-multiplier-tube array, and the avalanche photo-diode (APD) array which was ultimately chosen because of its superior sensitivity and SNR at low light levels. An APD can be thought of as the semiconductor equivalent of a photomultiplier, i.e. a photodetector with a built-in first stage of amplification. By applying a high reverse bias voltage, APDs show an internal current gain due to impact ionization. The graph indicates that at a multiplication factor of

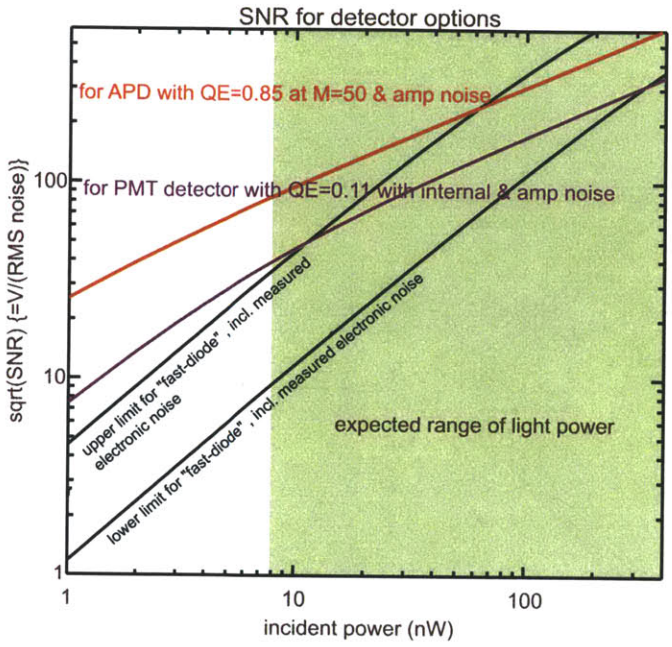

Figure 3-2: Estimated signal-to-noise-ratio of detector options and of the pre-existing fast PIN photodiodes.

50 (i.e. 50 charge carrier-pairs for every pair generated by photon impact), the APD certainly outperforms the PMT, and through most of the incident power range, also the PIN photodiodes.

This chapter describes the new GPI detector system built around such an APD array, by providing technical details of each element in Figure 3-3 from the detector, to the plasma.

3.2.1 Detector, Electronics, Data Acquisition

At the core of the new 2D GPI system are three Hamamatsu S8550 avalanche photodiode arrays. The S8550 is a 4×8 array of individual photosensitive surfaces, 2×8 sharing a common cathode. The element size is 1.6 mm $\times$ 1.6 mm on 2.3 mm centers. The quantum efficiency of the photoeffect is $QE \approx 0.85$ at both wavelengths of interest (656 nm, 589 nm). The most important operating characteristics of the device can be understood as follows. The multiplication ratio (gain, M) depends on the electric field applied across the avalanche layer, a characteristic value is then the

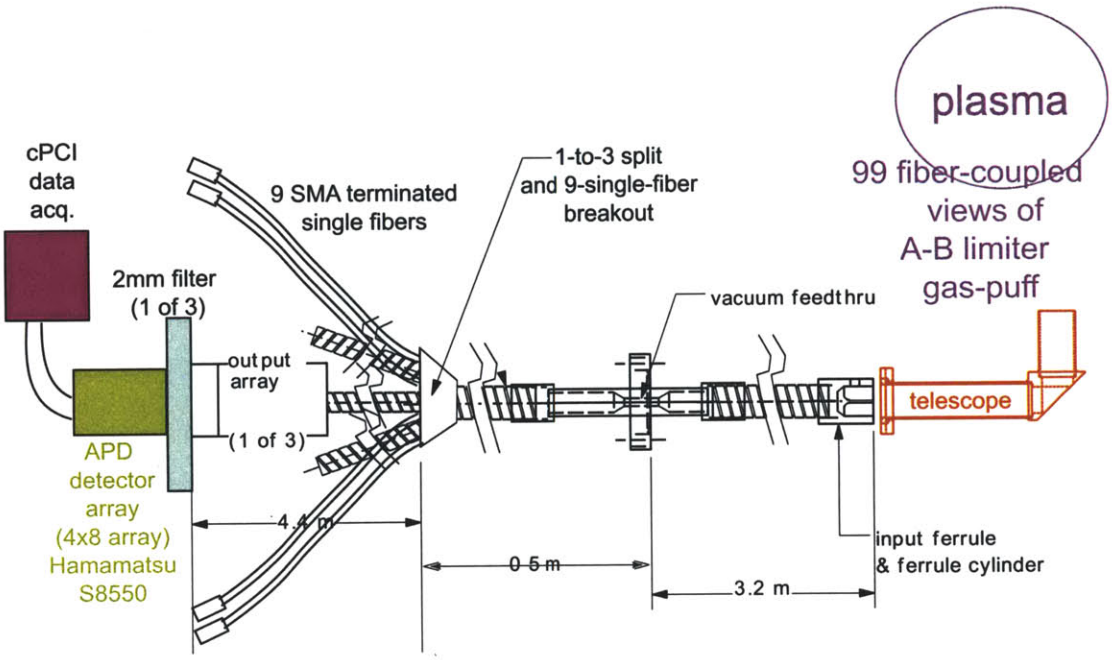

Figure 3-3: Schematic of new 2D fast imaging GPI system.

required voltage for a given typical gain, in our case for M=50. This is called the normal operating voltage VR. Normally, the higher the voltage, the higher the gain, however if the bias voltage is increased beyond a certain value characteristic of the device the diode starts conducting through. This is the breakdown voltage VB, which should never be applied. Table 3.1 gives both characteristic voltages for all six APD cathodes.

Table 3.1: Specific operational voltages of the APD arrays at room temperature ($25°C$)

cathode	07G024/1	07G024/2	07G025/1	07G025/2	07G026/1	07G024/2
VB(V)	454	455	450	442	440	439
VR(V)	409.5	412.8	403.5	392.5	391.1	390.3

It must also be understood that the APD gain has temperature dependent characteristics. At high temperatures stronger lattice vibrations will cause more drag on the charge carriers which will be less apt to trigger ionization. The temperature coefficient $1/M(dM/dT)$ is normally expressed in %/°C. To obtain a constant output,

either the reverse voltage has to be adjusted according to the changes in temperature or the APD must be kept at a constant temperature. We chose the latter solution, and therefore a chilling system was built for the APD's. Each chip is encased in a copper plate providing good heat contact with the device. Cooling is provided by circulating water in an aluminum case which covers the detectors and their read-out circuit on all sides. The water is cooled and circulated by a Thermo Scientific HAAKE EZ Cool 80 which keeps the temperature within ± 0.1°C of the desired temperature. Since a chiller was introduced into the system, it was decided to operate slightly below room temperature at 15°C, therefore the reverse voltage dependence of gain had to be calibrated on each device.

The calibration was carried out by illuminating the detectors with a steady light source and stepping the reverse voltage. A URS-600UV Labsphere was used for this purpose, with a calibration ferrule for the optical fibers (described later) which let us include a filter for the desired wavelength of light (described below). The temperature coefficients were measured at three different gain levels by repeating the measurement at room temperature and the operating temperature. It is a fairly slowly varying function going from $1/M(dM/dT) = -1.2\%/°C$ around HV=350V and reaching $1/M(dM/dT) = -3\%/°C$ around HV=410V. The factory given M=50 at VB was adjusted by these values to produce Figure 3-4, shown alone here for a single array cathode, but the M vs HV relationship had to be determined individually for each of the six cathodes. The crosstalk between channels was also tested in the calibration process, by illuminating a channel (red in Figure 3-5) individually using the same calibration ferrule as above. The two adjacent photosurfaces (yellow) showed a response 0.6%, and the one diagonally across from the illuminated channel (green) showed a crosstalk of 0.4%. The signal was undetectable everywhere else on the chip. There is absolutely no measurable crosstalk between channels on different cathodes.

The photocurrents from each anode are amplified by a simple trans-impedance circuit using Burr-Brown OPA2380 precision, high-speed amplifiers from Texas Instruments in the layout shown in Figure 3-6. The graphed circuit elevates the zero input voltage to ~ 1.14 V, so that with the negative input current, the output has a

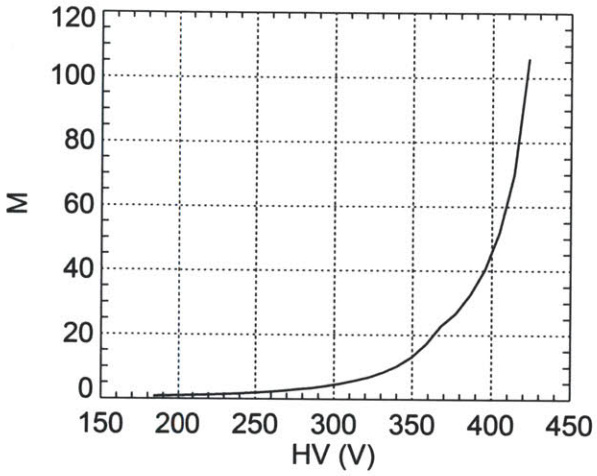

Figure 3-4: Multiplication factor (gain) M vs reverse voltage HV for the array 07G024/1 at $T = 15°C$.

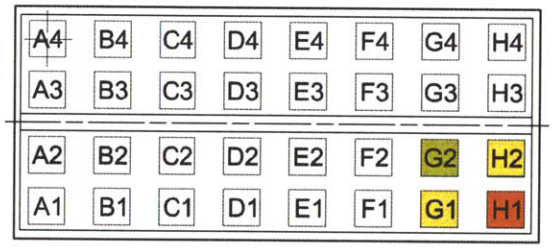

Figure 3-5: Layout of channels in the crosstalk test of the APD array.

range of ~ 3.5 V. The OPA2380 is spec'd to have a flat frequency response with the APD's terminal capacitance of $C_T = 10$ pF. This was tested with the result shown in Figure 3-7. The bandwidth of the electronics is therefore $BW \approx 1$MHz, and the signals are digitized at a rate of 2M frames per second by 3 D-tAcq ACQ132CPCI 32 Channel Simultaneous digitizers, providing 14 bit ADC per channel. The input voltage range of the digitizer can be switched between ± 10 V and ± 2.5 V. Since the signals are in the range $-2.3 \text{ V} < V_{\text{out}} < 1.14$ V, the latter setting must be selected upon startup in order to minimize digitization noise. With the above settings, at the low light levels which produce 10% of the maximal output voltage on the PIN photodiodes, the new detector was tested against the fast photodiode system with the results in Table 3.2. The application of APDs clearly increases the dynamic range, but most

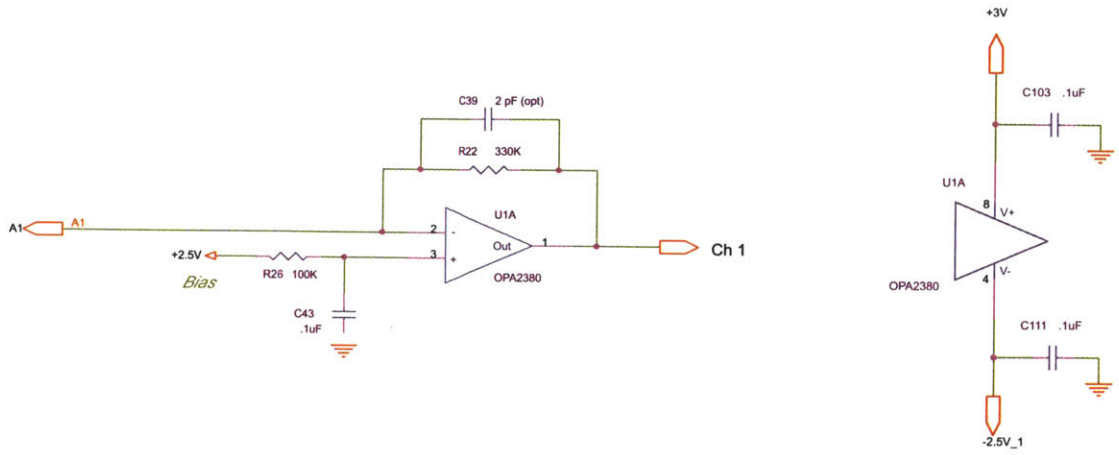

Figure 3-6: Layout of the transimpedance circuit (left) and its power voltages (right).

important, causes an order of magnitude improvement in the signal-to-noise-ratio at low light levels, thus confirming the estimates of improved sensitivity illustrated in Figure 3-2.

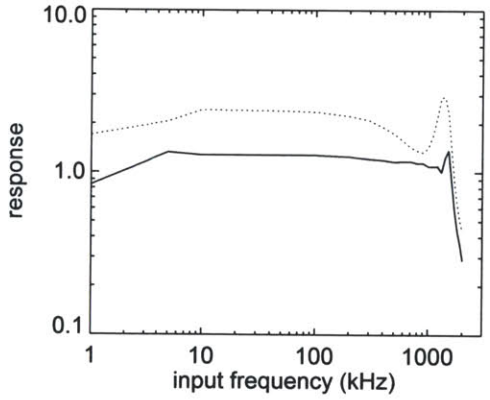

Figure 3-7: Frequency response test of the APD system (solid curve) against the previously calibrated PIN photodiodes (dashed line).

The dynamic range is further improved by being able to adapt the individual cathodes to the plasma conditions. High voltages for reverse biasing the APDs are provided by 6 programmable Emco C05 units (which produce from 0 to 500 V at 2 mA, and thus can cover the whole range of the APD operation), and consequently the reversed voltages can be changed on a shot-to-shot basis from the control room with-

Table 3.2: Response to low light levels in PIN and APD at M=30

Detector	V_{out}(mV)	V_{rms}(mV)	S/N
PIN	200	90	2.2
APD	120	5	24

out access to the cell where the detectors are located. Note that in this design the system must not be used with a reversed voltage less than HV$\approx$ 200, because with a high voltage too low the leads on a common cathode can conduct through backwards, effectively shorting the inputs of two opamps and driving some amplifiers to positive while others to negative power supply voltage.

3.2.2 Optical Solutions and Materials

Since the photosensitive surfaces are quite small, in order to eliminate a complicated optical system which could image to such a small spot, the fibers connecting the detectors to the plasma views are coupled close to the photosurfaces with only an interference filter interposed. The optical fibers are quartz, have an inner diameter of $400\mu m$ and are custom made by RoMack Inc in groups of 30 in an MIT specified order onto three MIT machined output ferrules which are designed and precision machined to match the centers of each array's individual detectors. For calibration purposes, an additional output ferrule was manufactured with one end having fibers precisely matching the form-factor of the Hamamatsu arrays and with the other end terminated in 30 individual-SMA connectors. The three close-packed arrays of 3 $\times$ 10 fibers are arranged side-by-side (radially) on the light input side, because the radial variation of light is much greater than the poloidal variation, and controlling the reverse voltages separately enables us to adjust for all dark or all bright channels together without saturating some detectors while not getting enough current out of some others.

The fibers have an acceptance cone corresponding to an optical relative aperture of F/#= 2.2 at the output, which makes the maximum distance they can be from the 1.6 mm $\times$ 1.6 mm photosurface for complete exposure D_{max} = 2.5 mm. Since

the signals must be filtered for the required wavelength, custom made, especially thin filters for both the HeI and Dα lines were specified by us and purchased from Andover Corp. Given that we are not using any collimator optics, the transmission at an angle through the interference filters must be taken into account. For the wavelength of a wave passing through at an angle θ with respect to the normal to the surface, we have

$$\lambda_\theta = \lambda_0 \left[1 - \left(\frac{n_{\text{ext}}}{n^*}\right)^2 \sin^2\theta\right]^{1/2} \tag{3.3}$$

which with a maximum angle determined from F/#=2.2 means that all light is still collected for a bandwidth of 10 nm for both wavelengths. The specifications of the interference filters can be found in Table 3.3. Note that the thickness includes a 0.5 mm casing for which a groove is cut into the output ferrule, so that the ferrule is actually $D = 2$ mm away from the surfaces, leaving a 0.3 mm margin in all directions.

Table 3.3: Parameters of the interference filters for the new 2D GPI diagnostic

Description	Dα	HeI
Wavelength	656.3 nm $\pm$ 2.0	589.0 nm $\pm$ 2.0
Bandwidth	10.0 nm $\pm$ 2.0	10.0 nm $\pm$ 2.0
Construction	3 cavity	3 cavity
Size	25.0 mm	25.0 mm
Thickness	2.5 mm	2.5 mm
Effective Index n^*	2.05	2.05

3.2.3 Geometry

A poloidal section and a top view of Alcator C-Mod is shown in Fig. 3-8 with cross sections of the magnetic flux surfaces of a typical lower-single-null (LSN) equilibrium and the schematic of the array of gas-puff-imaging (GPI) diagnostic views overlaid. The telescope focuses the 9 $\times$ 10 array of in-vessel optical fibers on the low-field-side "midplane" region with toroidally viewing, horizontal lines of sight. The deuterium Balmer α or the HeI line is locally enhanced at the toroidal position of the system's

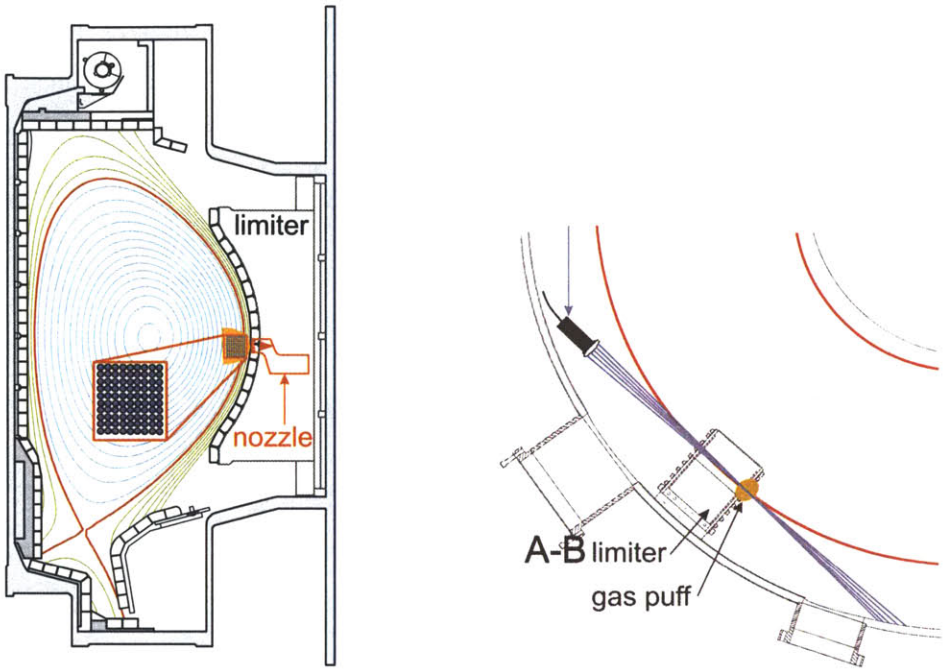

Figure 3-8: (left) The cross section of Alcator C-Mod with a representative LSN magnetic equilibrium. The diagnostic gas puff enters from a 4-barrel nozzle mounted in the low-field-side limiter, with its center 2.54 cm below the height of the midplane. The 2D GPI viewing array covers 4cm(*radial*) × 4.4cm(*vertical*) at this location, extending both into the region of closed flux surfaces (inside the thick curve, blue) and open field lines (outside the thick curve, green). (Right) The top view of C-Mod with the LFS viewing GPI chords in blue. The arrow points out the in-vessel location of the telescope.

focus by a D_2 (or ^4He) gas puff from the nearby nozzle.

The viewing area is 4cm (radial) × 4.4cm (vertical), with an in-focus spot size of 3.8 mm for each of the 90 individual channels, viewing the region with major radii of 88cm $< R <$ 92cm and heights-above-axis of $-5.4\text{cm} < z < -1\text{cm}$. Note that the radial extent of the field of view $L_{vis} = 4\text{cm}$ ($\approx 0.2\times$ minor radius) is broad compared to the relevant physical size scales of the plasma edge: the characteristic length of the pressure profile, $L_{vis} \gtrsim 6L_p$ and the sound gyro-radius $L_{vis} \gtrsim 60\rho_s$.

Chapter 4

GPI Measurements of Edge and SOL Turbulence

This chapter presents the initial results on the investigation of turbulence in Alcator C-Mod with the new Gas-Puff-Imaging diagnostic. The main focus of the work is turbulence in the Ohmic L-mode; therefore in all cases where it is not otherwise noted, measurements are from this confinement regime. First, the characteristics of individual emission signals will be presented in order to introduce the most basic concepts involved with GPI and to define the different regions in configuration space spanned by the diagnostic.

4.1 Emission Time Histories from Single Views

Two examples of signals representing the time evolution of the line radiation are shown in Fig. 4-1. The graphs illustrate the effect of the gas puff, and are specifically chosen with a D_2 puff into a D plasma in order to show a finite gas-puff contrast. The substantial brightness increase marked by the arrow in the figure at $t = 0.9$ s is caused by the introduction of neutral gas. The gas-puff contrast is defined as the ratio between the time average intrinsic radiation (before 0.9 s in the graph) and the gas-puff enhanced level; for the samples given in the figure, the contrast is ~ 5. Since the lines of sight of the GPI system cross flux surfaces (cf. Fig. 3-8) and the

distribution of the intrinsic light primarily depends on the local neutral density and electron density and temperature – which are toroidally symmetric – a high gas-puff contrast is a fair indicator of a toroidally well localized gas puff and thus a radially well localized measurement.

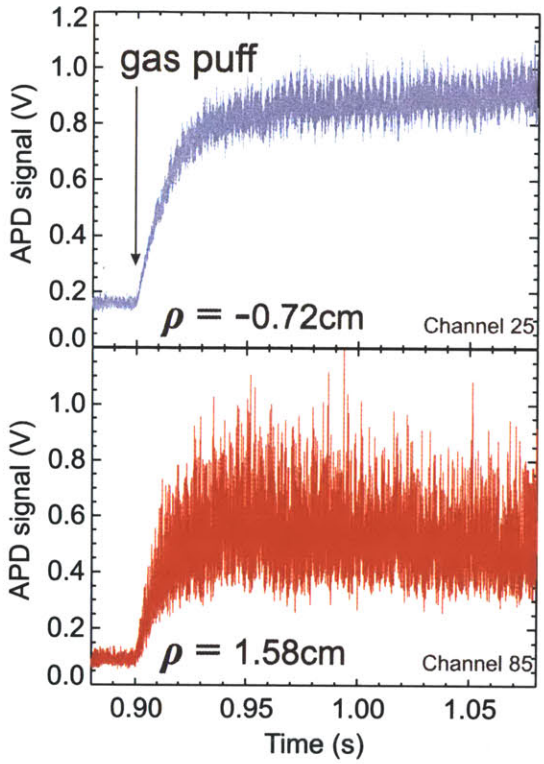

Figure 4-1: Sample signals from inside the LCFS ("edge", top) and the open field line region ("SOL", bottom). The arrow marks the time when the D_2 gas hits the plasma edge. The gas-puff contrast is the ratio of the pre-puff average to the post-puff average of the same duration.

In the rest of this thesis, observations of clear differences in the turbulence characteristics of the open and closed flux surface regions will be reported, consequently we distinguish between the regions by using the term *"edge" to refer exclusively to the* $\sim 2cm$ *wide region inside the last closed flux surface, as opposed to the "Scrape-Off-Layer" (SOL) which is the region with open field lines.* The physical depth of the measurements is labeled by the variable ρ, the distance of the flux surface from the separatrix mapped to the height of the magnetic axis on the low-field-side, and takes a positive sign in the SOL. Figure 4-1 then also demonstrates an important trend

observed previously in many GPI and BES, as well as probe measurements of tokamak edge/SOL plasmas [45, 31, 46]. The trend is demonstrated by the dissimilarity between the nature of the top and bottom figures. It is clear from the figure that the relative fluctuation power changes significantly across the viewing array. The range of fluctuation levels is $5\% < \delta n/\bar{n} < 95\%$ increasing with ρ, where δn is the rms fluctuation. But, perhaps more importantly, the top trace in the figure, from the edge, shows a signal distribution relatively steady in time, whereas the bottom trace, one from the SOL, exhibits bursty positive events. The probability density functions (PDF) of the SOL signals is consequently more skewed, as is evidenced by Fig. 4-2 where the two distributions are overlaid for comparison.

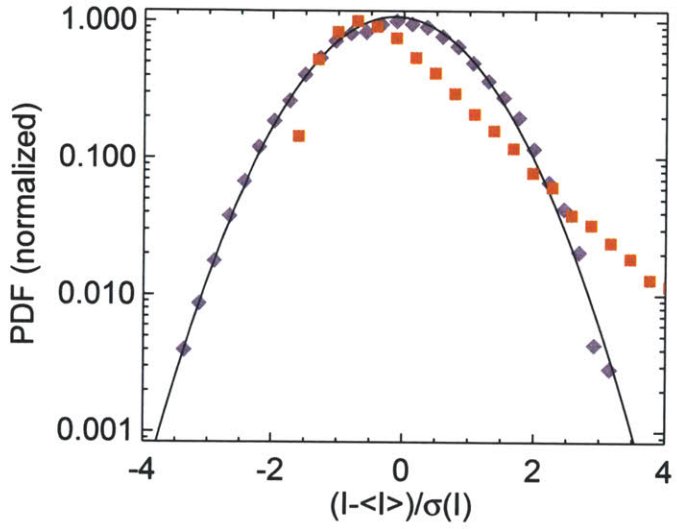

Figure 4-2: Probability distributions of two traces; a fluctuation signal from the edge region (blue diamonds) showing an almost exact Gaussian distribution (all moments of order > 2 vanish), with the quadratic fit overlaid (solid black), and a fluctuation signal from the far SOL (red squares) exhibiting a highly skewed and flattened distribution due to a relative excess of positive bursts.

In order to produce reliable estimates of such distributions, the size of the sample needs to be large enough for the statistics of the sample to converge to the distribution of the measured random variable. The convergence size depends on the underlying distribution as well as the signal-to-noise ratio of the sampling method. The conver-

gence of the distributions was therefore tested both in the edge and the SOL regions by observing the convergence of the first four standardized moments of the distributions, the mean $\mu = \langle I \rangle$ (whose standardized form is identically zero), the variance $\sigma^2 = \langle (I - \langle I \rangle)^2 \rangle$, the skewness [47, 48]

$$S = \frac{\langle (I - \langle I \rangle)^3 \rangle}{\langle (I - \langle I \rangle)^2 \rangle^{3/2}}$$

and the kurtosis [47, 48]

$$K = \frac{\langle (I - \langle I \rangle)^4 \rangle}{\langle (I - \langle I \rangle)^2 \rangle^2} - 3,$$

where 3 is subtracted from the flatness value since that is the flatness of a normal (Gaussian) distribution. The slowest convergence is, as expected, exhibited by the kurtosis of signals from the SOL, i.e. the most flattened and skewed distributions. It converges at a sample size of $N_{\text{samp}}^{\text{min}} \approx 30000$, or taking the sampling rate of the system into account, at $t_{\text{samp}}^{\text{min}} = 15$ ms, which we henceforth used as the minimum sample length for the estimation of distributions and spectra.

Before comparing distributions generated from light intensities, another feature of the signals to consider is the linearity of the brightness response to density and temperature fluctuations. The intensity is locally a power function of the electron density and temperature, with the exponent possessing a complicated density and temperature dependence, as detailed in Appendix B. Linearization of the response in the density (and temperature) perturbation can be verified to cause an error of less than 5% so long as the perturbation is less than 50% of the average. This holds for a fairly wide spatial range, but breaks down at ρ's outside the near SOL, i.e. at $\rho \approx 0.5$ cm. For the signals outside of that range, the correct power law needs to be considered; and where the average electron temperature drops below ~ 10 eV the more complex dependence explained in the Appendix has to be taken into account, wherever possible. For a large number of signals from both He and D gas-puffs, and from a range of spatial views, after being treated appropriately to their characteristics as described above, the skewness and kurtosis of the PDF's are plotted against each

other in Fig. 4-3.

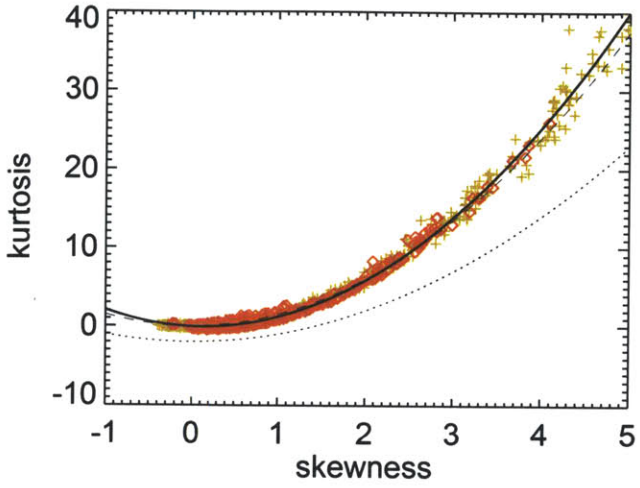

Figure 4-3: Kurtosis versus skewness of the adjusted signals from 3600 traces. Orange crosses represent shots with a He-puff, red diamonds shots with a D-puff. The fitted quadratic curve is plotted in a solid line; the dotted line marks the mathematical minimum of the kurtosis at a given skewness, while the dashed line represents the characteristic S-K relationship of the gamma-distribution, therefore the maximum of any beta-distribution.

The relationship between the skewness and the kurtosis is expected to be at least a quadratic one, since it can be shown directly[49], that for any distribution $1 + S^2 < F = K + 3$, where F is the flatness, unadjusted for normal distributions. Indeed, a least-squares fit of the data in the figure to a quadratic polynomial provides a good match with

$$a = 1.69 \pm 0.25 \tag{4.1}$$

$$b = 0.4 \pm 0.2 \tag{4.2}$$

$$c = -0.04 \pm 0.01, \tag{4.3}$$

for $K = aS^2 + bS + c$, which is the solid curve plotted in the figure. A quadratic relationship between the skewness and the kurtosis has been shown in a wide range of physical situations [50, 51, 52], and it is characteristic of many PDF families (such

as the Beta, Weibull, inverse Gaussian, log-normal, etc distributions [47]). Because of this, the particular coefficients of the quadratic relationship carry information about a potential theoretical PDF that reproduces all the experimental distributions, if possible.

Of the distributions mentioned above, the log-normal distribution at $c = 3$ is out of bounds; the inverse Gaussian distribution does not converge to the regular Gaussian distribution with μ/σ^2 as fast as do the experimental distributions, and the Weibull distribution (defined by the cumulative distribution function $F(x;k,\lambda) = 1 - \exp(-[x/\lambda]^k)$ [47]) exhibits a similar problem, generating negative skewness at the required widths. Previous measurements in tokamak plasmas [52, 53, 54] reported a change in the skewness sign when crossing the separatrix and called on the class of Beta distributions[52], or a combination of Gamma distributions[55, 56]. In our measurements, there are very few points at negative skewness, and even those appear at a moderate $S > -0.5$. To make contact with the results from other tokamaks, a fit with the generalized Beta distribution, given by the PDF

$$f_B(x;\alpha,\beta,x_{\min},x_{\max}) = \frac{1}{B(\alpha,\beta)}(x-x_{\min})^{\alpha-1}(x_{\max}-x)^{\beta-1}$$

was tested, for the special cases in which $S > 0$. For the general Beta distribution one can show that

$$K \leq 1.5S^2,$$

and the equality holds only when one of the exponents diverges (for $S > 0$ this means $\beta \to \infty$), and the corresponding S-K curve is plotted in Fig. 4-3 as a dashed line. If one simultaneously allows for $x_{\max} \to \infty$, the function becomes that of the more familiar Gamma distribution

$$f_\Gamma(x;k,\theta) = \frac{x^{k-1}}{\theta^k}\frac{e^{-\frac{x}{\theta}}}{\Gamma(k)},$$

which has recently been used to fit edge and SOL density fluctuation data in a number of experiments[57, 56].

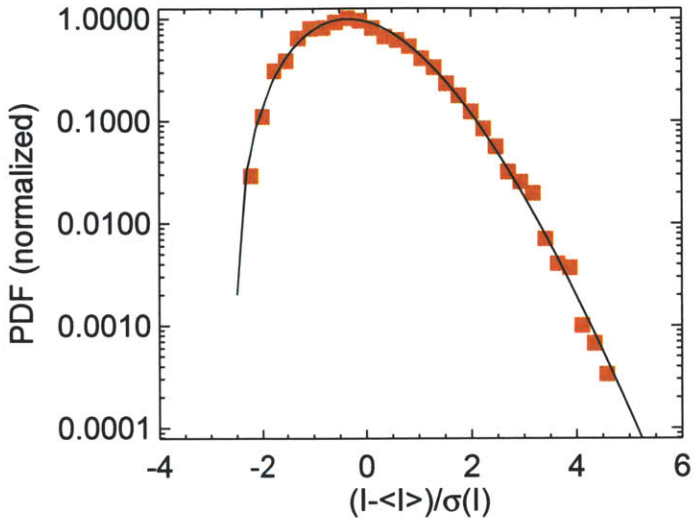

Figure 4-4: Sample probability distribution function of an adjusted trace with a medium skewness and kurtosis value, with the appropriate Gamma distribution overlaid.

The solid line in Fig. 4-4 represents a Gamma distribution matching the local GPI signal, adjusted in the sense described above. It is worth noting that other than setting the mean and the variance, no further fitting is necessary for a near perfect overlap in this region ($\rho \lesssim 1$ cm), making an excellent match to the measurements at the TCV[57], and unlike situations in which two separate Gamma functions were invoked for a better fit[56]. The latter becomes necessary only when, as expected, the Gamma fit breaks down in the region where the combination of the small time-average electron temperature and the appearance of large ($> 100\%$) bursts makes a simple power-law adjustment of the brightness signals impossible; it therefore seems to be a systematic effect. These signals were consequently not used in Fig. 4-3.

The importance of these findings is that fluctuations measured over the entire edge and SOL, including the high density and temperature gradient region, a likely source for instabilities, are characterized at all locations by PDFs of a universal character, in the sense that a unique relation links the skewness and the kurtosis, and that they can be described by the same analytical distribution. The latter is a strong indication that events in the whole region are related. Furthermore, the spatial positions where

the PDFs converge to a Gaussian one are located at and inside the separatrix. This is suggests that the transport in the regions inside is more diffusive-like. Since these PDFs are described by distributions of the same analytical form as those from the SOL, leading to the "universal" S-K relationship shown in Fig.4-3, this strongly suggests that the *edge* is the source of bursty, turbulent features of the SOL.

4.2 Wavelet Transforms

In the previous section special care was taken to avoid referring to the skewed and flattened distributions and the corresponding bursty events of the SOL as *intermittency.* Although in parts of the literature on turbulence – and edge plasma turbulence in particular – it is now more or less customary to apply this term, it often does more to obscure rather than clarify the nature of the observed fluctuations, and their proper place within the theory of turbulence.

In this section it is still single signals that provide the basic analysis material, but the complexity is somewhat increased by the application of a wavelet decomposition in an attempt to prove true intermittency in the emission from the SOL. The presence of rare, large amplitude events and thus a heavy tail distribution is not necessarily intermittency, the latter being defined by the measured quantity exhibiting activity only a fraction of the time. This is because the distribution of signals can be skewed down (or up) to any scale, in which case we may refer to the distribution as *self-similar* in nature. The properties of the turbulence at various scales τ can be studied by applying a continuous wavelet transform, providing a decomposition

$$C_\tau(t) = \frac{1}{\sqrt{\tau}} \int I(t') M\left(\frac{t'-t}{\tau}\right) dt',$$

where the kernel $M(t)$ is the so-called mother wavelet, in this case the "Mexican Hat" (2^{nd} derivative Gaussian), commonly used for singular feature detection. The specific difference of intermittency is then the quality that the distribution function of an

intermittent process cannot be homogeneously rescaled, ie

$$P\left(C_\tau(t)\right) = \lambda^h P\left(C_{\lambda\tau}(t)\right)$$

cannot hold for all λ, regardless of the degree h. Figure 4-5 gives an example of just this behavior, comparing the shortest time scale $\tau = 64\mu$s at which the PDF is nearly perfectly Gaussian to a short time scale of the same signal at which the wings are important in the PDF, thus proving the presence of true intermittency. The largest coefficients are observed around $\tau = 4\mu$s.

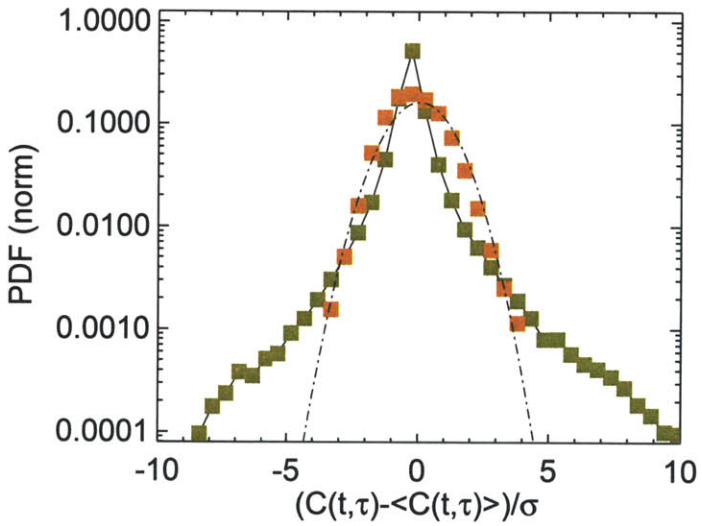

Figure 4-5: Probability density functions of wavelet transforms at two different time scales, exhibiting a proof of intermittency, since at scale $\tau = 2\mu$s (green) bursts give a large weight to the wings of the distribution, whereas at scale $\tau = 64\mu$s (brown) and above, the distributions revert to a Gaussian shape (dash-dotted line). The two distributions cannot be linearly scaled into each other.

The heavy tail distributions conform well to the ones shown in Fig. 4-2 and only appear symmetric due to the choice of the mother wavelet, having the same positive weight as negative.

Self-similarity is a crucial assumption for a cascade-like spectral transfer process in the Kolmogorovian sense [48, 36, 58]. As we can see, in most scales important for the fluctuations of the SOL this symmetry is, however, violated. Nonetheless it is still

reasonable to apply a spectral transfer analysis relying on local transfer *in the edge plasma.* This will be important for the study of edge turbulence structures presented later in sections 4.7 and A.

Upon proving true intermittency, the wavelet decomposition also renders it possible to identify the intermittent events in the time series, which brings up the important issue of the distribution of waiting times between events. First, to characterize the local activity present in the signal at a given time scale τ and time t, a method described by Farge [59] was used. The events in this analysis are conceived of as the appearance of those structures that distort the otherwise Gaussian background, therefore the method splits up the signal into two orthogonal sets of wavelet-coefficients. A threshold on the *local intermittency measure* (LIM)

$$l_\tau(t) = \frac{C_\tau(t)^2}{\langle C_\tau(t)^2 \rangle}$$

is defined such that all points which fall below belong to the background and all those exceeding it are considered intermittent events. The threshold is found iteratively as the one that sets the kurtosis of the background zero, which ensures that the background have a Gaussian distribution. Since events may last more than a single time point, the time instances of intermittent activity are identified as those that belong to the "event distribution" and have a local maximum. In Fig. 4-6 the probability distribution of waiting times at the most important scale $\tau \approx 4\mu$s. The fit to an exponential distribution is demonstrated. The time constant of the distribution shows some variation with the time scale considered but is generally close to the one fitted to the scale plotted, $t_{4\mu s} = 110\mu$s, which due to the exponential distribution is also the expected value of the waiting time. The significance of an exponential distribution for the waiting times is that it is the continuous limit of the geometric distributions, which are mostly known for characterizing a random process with no memory.

The above analysis then also indicates the presence of coherent emission features in the SOL. These structures have indeed been reported [60, 61, 62, 63] to exist outside the confinement zone, and moreover to be the dominant mechanism for energy and

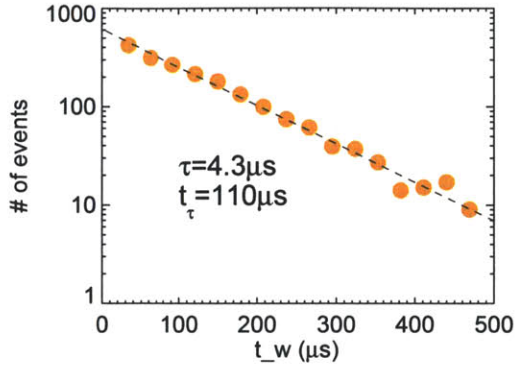

Figure 4-6: Distribution of waiting times between intermittent events at the most important scale. The dashed line is an exponential fit.

particle transport there. Due to the intermittent nature of these events, the common Fourier-methods used in the remainder of this thesis are not as adequate in their region of dominance as are wavelet-based analysis techniques, on which a more detailed analysis of SOL fluctuations should therefore rely, and has indeed relied in various previous experiments [46]. That, however, is outside the scope of this thesis, as its primary focus after the next chapter is the characterization of the edge turbulence, the most likely source of these intermittent events.

4.3 Two-Point Correlations

The power in the GPI brightness signals from the entire SOL, and sometimes even a few mm of the edge, are dominated by intermittent features. BES and GPI diagnostic measurements have long reported such coherent emission features in the SOL of tokamak[20, 64, 65], as well as reversed-field pinch[46, 66] plasmas and in linear devices [67, 68]. Due to the usually *near-circular poloidal cross-section* of these at the low-field-side midplane of tokamaks, they are now widely known as "blobs", and there is a vast literature on both theoretical and experimental studies addressing their shape[69, 70], time-statistics[71, 41], radial speed and its relationship to the poloidal size of the blob [69].

This section addresses the characteristic size corresponding to the maximal in-

tensity event time scales by calculating the correlation coefficient with zero time lag between the signal of a reference channel and all other views in the GPI APD array. The exact method of estimating the correlation coefficient at an arbitrary time lag and hence calculating propagation velocities for the brightest features (known as Time-Delay Estimation, or TDE) is described in Appendix C. At least in the SOL, the shape and size of the high correlation regions are expected to represent the typical shape of emission features, due to the fact that the intermittent events carry the overwhelming majority of the fluctuation power in the SOL.

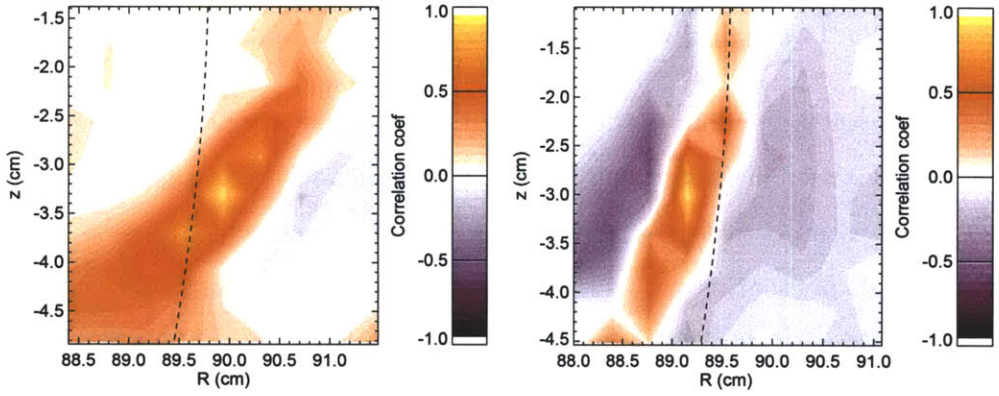

Figure 4-7: Zero time-lag correlations to a view close to the separatrix in a D-puff, $I_p = 0.6$ MA, $B_T = 4.84$ T (left), and a He-puff, $I_p = 1.2$ MA, $B_T = 5.6$ T (right); the dashed line indicates the projection of the separatrix.

Although the correlation lengths in the radial and poloidal directions are very close to both each other, at $\xi_r = 0.8$ cm and $\xi_\theta = 1.0$ cm and those measured by the fast framing CCD, the two dimensional maps of the correlations turn out to be very different from those recorded by the cameras and many previous, albeit lower sensitivity, GPI measurements on other machines. Only the far SOL of plasmas with a large outer gap and He gas puffs exhibit near-circular patterns at all. Patterns typical for most locations in the edge and SOL are displayed in Fig. 4-7. The contours of $\sim 50\%$ correlation around the reference channel are highly elongated, covering a significant proportion of the viewing array, and without exception they slant so that they have a positive tangent in the $R-z$-plane. These elongated and tilted correlation patterns are unlikely to be instrumental artifacts. Observe that in some cases, such

as the one depicted in Fig. 4-7a, the band extends across over three quarters of the field of view radially. This involves correlation between different detector arrays and different digitizers.

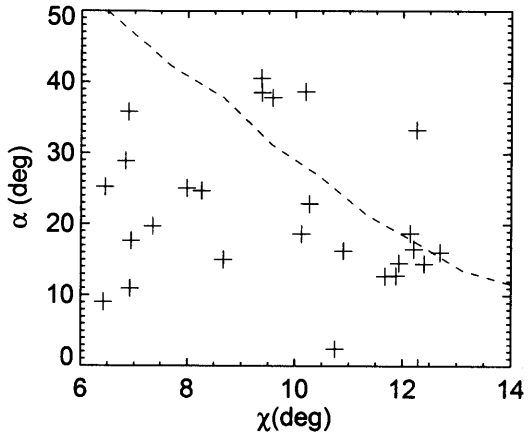

Figure 4-8: The angle α the correlation band makes with the vertical within the GPI field of view against the pitch angle of the magnetic field as reconstructed from magnetics. The dashed line is the α expected from viewing a filament structure illuminated by a toroidally extended gas puff. It is clear that the observations do not follow this dependence; indeed no general trend with pitch angle is observed.

In search of systematic effects, one may turn to the radial non-localization due to toroidal spreading described in Section 3.2.3. With the assumption that the dominant feature in the correlation maps would be one with the highest overall intensity spatially, the shape of a fluxtube in the SOL crossing the reference channel and reaching farthest into the SOL (achieving the highest feature contrast) at the brightest part of the array was tested for a wide range of magnetic geometries, and compared to the correlation patterns generated. Due to the LoS not being aligned with the magnetic field lines, such flux tubes are expected to be approximately ellipses, the vertical elongation of which should sensitively depend on the angle $\chi = \arctan(B_\theta/B_\phi)$ the local magnetic field lines subtend with the horizontal LoS, commonly referred to as the magnetic pitch angle. The comparison was quantified by determining the angle α the visible section of a least-squares-fit parabola to the experimental maxima makes with the vertical and comparing it to the value predicted for the elliptic curves generated

in the described manner. However, the experimental points displayed in Fig. 4-8 show no dependence on the pitch angle.

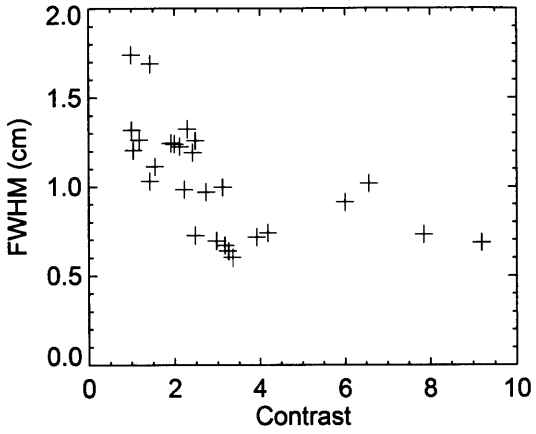

Figure 4-9: The full width at half the maximum correlation (FWHM) plotted against the field-of-view-average gas-puff contrast, as defined in 4.1. The width clearly decreases with increasing contrast, and settles around 8 mm.

In addition, the dependence of the correlation patterns on the quality of the gas-puff contrast was tested. While the results, as demonstrated in Fig. 4-9, do corroborate the importance of a high puff contrast by showing that the width of the pattern decreases rapidly up to a contrast level of ~ 4, neither the shape nor the tilt angle α were exhibited a dependence on contrast.

More recent measurements of the correlation patterns in the signals of the fast framing GPI CCD camera, sampling at 380 kFPS constructed in the same manner as the ones in Fig. 4-7 have in fact shown similarly tilted structures in He gas puffs. Accordingly, the tests were repeated on the APD signals after a wavelet decomposition to test for fast time scales only, with the result that all meaningful scales (i.e. up to the complete loss of significance due to edge effects) have the same behavior. Therefore the cause of these patterns remains unknown.

The positive result reported here is that the characteristic size scales of fluctuations in the SOL together with the most important time scales determined through wavelet decomposition provide values that are well within the range of both previous observations and the theoretically expected values [69, 11, 12] for blobs. The

poloidal velocities estimated from TDE analyses of these features ($\bar{v}_\theta = 1$ km/s and 0.8 km/s respectively for the two shots in Fig. 4-7) are in good agreement with the ones determined using Fourier methods, which become important for the remainder of the chapter. Radial velocity measurements show similarly large velocities in the SOL, $v_R = 0.3 - 1.0$ km/s. This rapid radial motion outwards is not only a typical trait of blobs reported previously by both C-Mod researchers and others [41, 72, 73], but, due to the relatively high particle density and temperature of the intermittent features, also emphasizes their importance in non-diffusive cross-field transport in the SOL region.

4.4 Single Fourier Transforms

This section introduces the basic methods and results of the Fourier-analysis on which the main findings of this thesis, detailed in the section and the chapter which follow, are based. In addition to the analysis in those chapters, we may note that observing the spectra of the signals described in the previous sections is essential in determining the physical meaning of the flat distributions of signals and intermittency in general; for instance, non-Gaussian statistics have been known to be caused by long-lived coherent modes[45]. This, however, is certainly not the case for the L-mode samples. As it has been reported from various tokamaks, as well as RFP and linear plasma devices, the fluctuations of the edge and SOL densities are very much broadband: there is no evidence of any distinct, small-scale ($k_\perp a \gg 1$) peaks in the power-spectra, characteristic examples of which are shown in Figs. 4-10 and 4-11. More precisely, the spectra shown here and in later sections are time averaged over at least 15 ms from spectrograms with a bin size that accommodates for a frequency resolution of $df_{\text{req}} = 2$ kHz. In order to cancel any slow variation due to a time-changing gas-puff level as well as non-uniformity in the internal gains of the APDs, the signals are normalized binwise to the average brightness (see App. C). This process also has the advantage of yielding spectra in the familiar relative fluctuation level form $\delta n/\bar{n}$.

In the case of broad spectra like these, the overall frequency (or, when applicable,

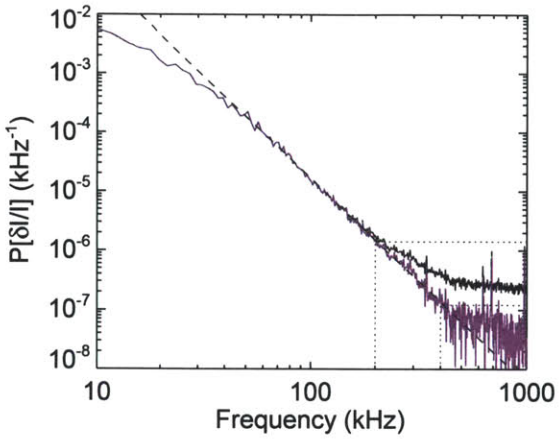

Figure 4-10: Demonstration of the effect of subtracting the spectrum of the photon noise estimated from calibration to a constant light source.

wave-number) scaling is the first thing to examine since this can yield information on (i) the character of the pulses (esp. in the SOL) and/or (ii) the dynamics of the turbulence. For the former, it is worth briefly noting that recent literature on the topic has reported both exponential [74] and (partly) power-law [29] spectra, as well as a mixture of the two [75] on different types of devices. From the large number (over 100) of experimental conditions measured on C-Mod exponential spectra have not been observed in either the edge or the SOL plasmas of either L- or H-mode confinement regimes. Regarding power-law dependences, we note that since the first scale-free cascade model of spectral transfer by Kolmogorov[58] a number of models predict a power-law dependence for energy spectra $S(f) \propto f^{-\beta}$, with a spectral (or cascade) index β, in different scenarios for the turbulence dynamic (such as those described in Chap. 2.3). Most spectra from both the edge and the SOL of L-mode plasmas in Alcator C-Mod are described by either: (a) a section of "curved" spectrum in a log-log graph (consistent with a Gaussian pulse shape of intermittent features [74]) and a section of power-law decaying spectrum, or (b) multiple (usually two) power-laws (Fig. 4-11).

Since the photon noise is "white", i.e. not a function of frequency, for each average brightness level recorded by a particular APD detector there is a level of photon noise,

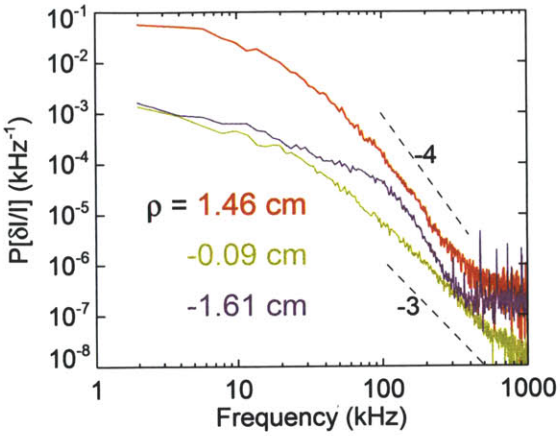

Figure 4-11: Average spectra of single signals across the entire field of view from a $B_T = 5.4$ T, $I_p = 800$ kA, Ohmic L-mode discharge.

known from the calibration. This level normalized to the average brightness was simply subtracted from the measured spectra, as shown in Figure 4-10. This results in a cleaner measurement for the low intensity (generally high frequency) part of the spectrum. In some cases this process is successful enough to reduce the minimum useful power in the normalized fluctuation level by nearly an order of magnitude more, providing a longer tail to which a spectral index may be fitted.

Figure 4-11 displays a typical tendency seen in L-modes. The spectral indices measured at the high frequency part of the spectra decrease as the sampled region moves from SOL in towards the LCFS, i.e. with decreasing ρ, with the actual values commonly in the range $2 < \beta < 4$, eventually giving way to spectra of a different shape in the plasma edge. More will be said about spectral indices and the breaks in β seen in the blue curve ($\rho = -1.61$ cm) of Fig. 4-11, which are common in the edge only. First, however, the separation of propagation directions of features on the same flux surface must be introduced.

4.5 2-Dimensional Spectra

4.5.1 Radial Profiles

The region observed by the GPI diagnostic can also be characterized by generating spatial as well as temporal Fourier transforms from the light signals. Since the GPI viewing array has 10 vertical views at each of 9 radial locations, it is possible to use true spatial Fourier transforms, rather than the two-point technique[76], which has gained a certain level of popularity in plasma turbulence measurements, mostly due to the availability of diagnostics with only a few spatial points. This enables us to directly study the wavenumber-structure of the fluctuations without needing to call on the Taylor-hypothesis of frozen flows [77]; for further advantages of this choice and a comparison of the two techniques, see Appendix C). The vertical columns of the viewing array are nearly aligned with the poloidal sections of the flux surfaces (cf. Fig. 4-7), so that the variation of ρ along any single vertical column is less than 1.5 mm at all times. Spatial Fourier-transforms along these columns therefore generate *poloidal* wavenumber information, yielding 2-dimensional, wavenumber–frequency spectra $S(k_\theta, f)$ from every vertical column in the array, i.e. 9 radial locations, spanning the edge and the SOL. Since as we saw in Section 4.4, typical turbulence spectra fall off rather rapidly with both k_θ and frequency, it is useful to inspect the 2-dimensional spectra in terms of the power of the components and the dispersion of the detected waves separately. For this purpose, the normalization

$$S(k_\theta|f) = \frac{S(k_\theta, f)}{\sum\limits_k S(k_\theta, f)} \tag{4.4}$$

is introduced. This normalization can be thought of as treating the spectrum as a probability distribution and generating the $S(k_\theta|f)$ *conditional spectrum*, in order to highlight the dispersion even in the relatively high frequency, high wavenumber domain.

The radial profiles of the edge turbulence produced in all purely Ohmically heated L-mode discharges are qualitatively the same. Conditional spectra of the edge–SOL

turbulence of these plasmas show a characteristic radial profile (Fig. 4-12). Fluctuations of the SOL produce a single lobe in the observed k_θ–f spectra with $k_\theta < 0$ cm^{-1}. A negative wavenumber in our sign convention means that the propagation is vertically *down*. With the toroidal magnetic field and plasma current direction of the most common C-Mod operation, this is in the *ion diamagnetic drift direction*[31, 29] (IDD). Edge turbulence, by contrast, is found to be dominated by $k_\theta > 0$cm^{-1} fluctuations, i.e. propagating in the *electron diamagnetic drift direction* (EDD).[1]

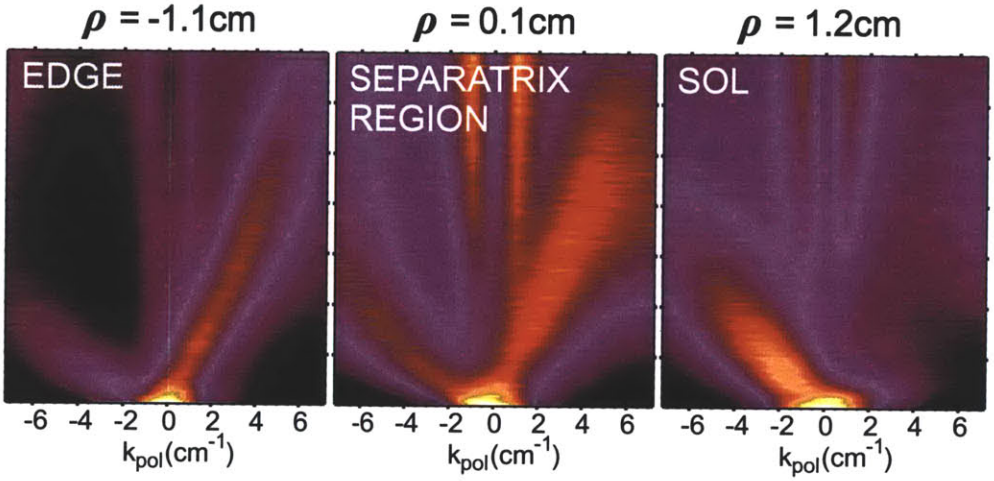

Figure 4-12: Radial profile of the turbulence in poloidal wavenumber and frequency space. $k_\theta > 0$ corresponds to propagation vertically up, in the EDD (see text) – this is characteristic in the edge, and $k_\theta < 0$ to motion in the IDD, this is characteristic of the SOL. The middle graph shows the separatrix region in which instead of a slowly propagating feature, both features are seen with their well defined speeds. The two narrow spikes in the middle are caused by noise. $B_T = 5.4$T, $I_p = 0.8$MA, $\bar{n_e}/n_G = 0.45$

This propagation velocity trend across the separatrix may not be surprising. Experimentally, similar profiles were found in our region of interest as early as 1984 in TEXT [28] and 1985 at Caltech [31], where probe measurements showed that the direction of propagation was IDD at the very edge and *changed smoothly* to EDD further in, and numerous measurements done more recently have found the same. Theoretically, similar structures are expected on the basis of neoclassical predictions and divertor-considerations. In the SOL, i.e. on open field lines, parallel electron

[1]Deviations from this radial profile of turbulent structure motion are introduced and discussed in Section 6.3, under the study of the effects of radio-frequency waves on the plasma edge.

losses dominate, setting up a potential due to the field line contact with the wall, which is $\phi_{\text{float}} \approx 3T_e/e$ (as in [78]). Since for all confined plasmas $\nabla T_e < 0$ must hold by definition, the radial electric field $E_r = -\partial_r \phi$ of the SOL is positive, setting the $\mathbf{E} \times \mathbf{B}$ direction parallel to what we labeled "ion diamagnetic drift direction" (IDD). In the edge, on the other hand, neoclassic transport predicts that perpendicular ion losses will dominate, rendering $E_r < 0$ in this zone, and generating an $\mathbf{E} \times \mathbf{B}$ drift in what we called the "electron diamagnetic drift direction" (EDD). However, there are details of the radial velocity profiles recorded with the new 2D GPI system at C-Mod that suggest a more subtle view.

4.5.2 Poloidal Velocities

The measured k_θ–f spectra are generally well fitted by a single linear dispersion relation up to high frequencies so that $v_{ph} = v_g = 2\pi f/k_\theta$ (cf. Fig. 4-13) for a broad range, and these velocities can be determined for every radial location. It is important to remember that the excitation of the neutral gas depends on the number and average energy of electron-neutral collisions making the diagnostic sensitive to a combination of $\tilde{n_e}$ and $\tilde{T_e}$ [79, 80]. The velocities measured from a spatial and temporal GPI spectrum are therefore phase velocities of emission features.

In order to compare the motion of observed emission features with expected fluid motion and particle drifts, the electron diamagnetic drift velocity in the edge and the near SOL are estimated using the n_e and T_e profiles from Thomson scattering [81], while radial electric field profiles in the SOL are evaluated from direct electric potential measurements made using scanning Langmuir probes[82].

One conspicuous feature of the middle graph in Fig. 4-12 is shown in more detail by the radial profile of these fitted poloidal velocities in Fig. 4-13. Wavenumber-frequency spectra from the separatrix region exhibit two counter-propagating lobes, with velocities very closely matching those found in the regions where the respective features dominate. In sharp contrast to the older results from probe measurements referenced in the previous section, these velocities are *never found to transition smoothly* from one direction to the other; rather, their velocities are remarkably constant with

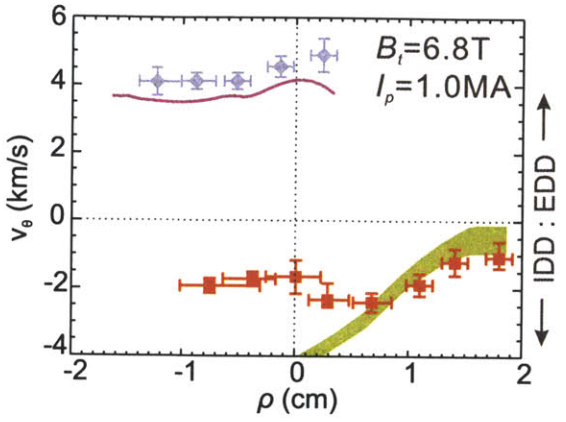

Figure 4-13: Radial profile of the poloidal propagation velocities. Diamonds show the measured phase velocities of the positive k_θ, while squares show those for negative k_θ. The solid curve (purple) is the electron diamagnetic drift velocity profile and the broad, solid band (green) is the $\mathbf{E} \times \mathbf{B}$ velocity for $\rho > 0$.

R; and in some cases the IDD propagating features exist as deep as $\rho = -1.7$ cm in the plasma, albeit with low intensities. This velocity trend is clearly demonstrated in Figure 4-13, where for comparison, we also plotted $v_E = E_r/B_T$ as a solid band (green), the thickness of which shows the error estimated from probe measurements. Probe measurements made in different discharges with similar q_{95} and normalized density as GPI observations, since probe data were not always available for the discharges with a diagnostic puff, show that this match is very reliably reproducible: in the far SOL, there is good agreement between v_E and the propagation velocities, although they manifestly deviate at $\rho \lesssim 0.5$cm. The EDD velocities in the edge are close to the diamagnetic drift velocity $v_D = \nabla p_e/n_e e B_T$ also plotted in Fig. 4-13 as a solid (purple) curve. The v_D curve generally runs below the measured phase velocities as expected, since v_E and v_D are expected to be in the same direction in the region. This suggests that the observed velocity is a combination of a bulk $\mathbf{E} \times \mathbf{B}$ rotation of the plasma and true propagation of waves in this region, at speeds typical of drift-wave-like turbulence. The diamagnetic velocity is plotted up to the separatrix only because in the open field line region the diamagnetic velocity determined from the average density profile becomes meaningless due to the large local perturbation to the density field at the time and location of a filament (blob) ejection. The diamagnetic

flow causes no drift to the blobs, but rather a rotation around the perimeter of the feature.

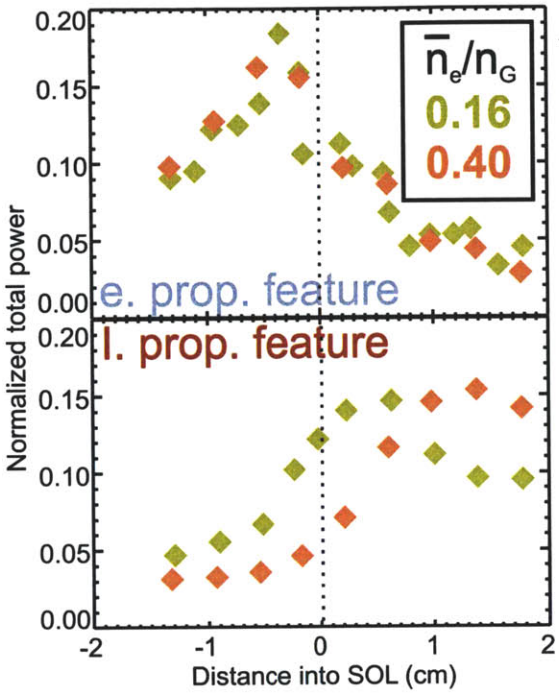

Figure 4-14: Radial profile of the total intensity of the features in Fig.4-12 from two plasmas with extremes of the Greenwald fraction. The plot of the electron diamagnetic direction propagating feature in the low density case is the composite of two shots. The profiles were normalized to sum up to unity, so that trends can be compared.

It must be made clear that this observation is not necessarily in contradiction with the early measurements of edge and SOL turbulence velocities either on Alcator C-Mod [83] or elsewhere[31, 28]. Whereas the early measurements made with a large probe array showed a change in the propagation direction from one column to the next [31] and others had a layer of "fuzzy" dispersions[29], probe measurements on C-Mod used a two-point correlation technique, for which a spectrum of the form in Fig. 4-12b *should* in fact produce a small absolute velocity. The smooth variation can be restored then in terms of the power contained in the two lobes in the $S(k, f)$ spectra. In order to demonstrate the two spatial regions of dominance, the power in $k_\theta < 0$ and $k_\theta > 0$ are integrated separately and plotted in Fig. 4-14 where the intensity profiles of both sides are normalized to a sum of unity, so the regions of dominance may

become apparent. The peak intensity (normalized to DC) of the SOL turbulence in the higher Greenwald fraction ($F_{Gr} = \bar{n}_e/n_G$) cases shifts outwards. The graph shows that instead of a smooth transition from EDD to IDD when crossing the separatrix, there are two regions with well-defined propagation velocities which vary little across their regions of dominance.

4.5.3 The High Shear Region

Because of this slight discrepancy though, the interpretation of the conditional spectra and the poloidal velocities derived therefrom at the region around separatrix is worth a few words. Such dispersions can arise in one of the following ways: (a) with two counter-propagating waves (potentially of different sources and dispersions) simultaneously present in the same spatial domain, (b) with the presence of finite size features with trajectories primarily perpendicular to the sampling array (ie mostly radial in our case) or (c) with a boundary between the two layers with different and well defined velocities that is narrower than the viewing spot. In addition to all these, some radial contamination is expected for large toroidal spreads. However the presence of this region does not depend on the quality of the gas-puff contrast.

As it was mentioned in Section 4.2, radial speeds become comparable to the poloidal propagation in the near SOL, which makes (b) at the separatrix unlikely. Scenario (a) can be tested by decreasing the spectral sampling time (for details, see Appendix C of the system to the point where either the lobes cease to be simultaneously present, or the frequency resolution necessary to produce the spectra is lost. It is found that the two lobes of approximately the same power persist down to $\sim 150\mu$s, and show clear signs of non-simultaneity at a bin size of $\sim 110\mu$s (Fig. 4-15), which we recall happens to be the characteristic time of blob ejections into the SOL. It must, however, be noted that no obvious correlation has been found between blob flashes in the SOL and the changes in the dominant propagation direction in the separatrix region to date. If the measured velocities were simply interpreted as $\mathbf{E} \times \mathbf{B}$ drifts, E_r would have to change sign in less than the 3.7 mm spot size, and attain its maximal values. This is in disagreement with both previous probe results [34] and measure-

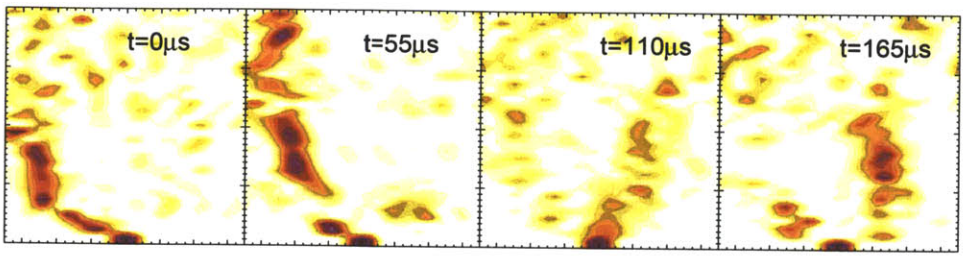

Figure 4-15: Conditional spectra from the separatrix region with $df = 9$ kHz, corresponding to $t_{\text{int}} = 110\mu$s with 50% overlap between samples for better time resolution. The scales are the same as in Fig. 4-12. Both sides show activity some of the time.

ments of the radial electric field by charge-exchange recombination spectroscopy [6]. Interpretation of the *edge* propagation velocity solely as v_E in these regimes also contradicts the existence of the E_r-well found in ref. [6], which should cause a shear in the region where the edge turbulence propagation velocities seem to be largely invariant. The results do suggest though the presence of a narrow (< 3.7 mm) boundary between the regions of the two counter propagating features, with a radially fluctuating position.

To summarize what we have learned so far, both the edge and the SOL spectra are broad-band, yet there are clear differences between the two regions: the fluctuation levels relative to the average brightness levels of the views are significantly (about an order of magnitude) higher in the SOL than in the edge; SOL emission signals are intermittent and produce distinctly different spectral distributions from those of the edge; emission features of the edge show no radial propagation, but pick up radial speed quickly once they cross the separatrix; and perhaps most obviously, the features in the two regions propagate in opposite directions.

The above observations suggest that the velocities measured belong to two distinct objects, a wavelike set of fluctuations dominant in the edge and plasma blobs moving generally with $\mathbf{E} \times \mathbf{B}$ in the SOL[2]. This motivates treating the two lobes of the k_θ–f spectra separately even in the regions of overlap, and may have implications as to the generation mechanism of the SOL features from edge turbulence, to which we return

[2]The fact that blobs are tracers of the v_E field has been shown in other experiments and simulations [84] as well and is essential for the analysis in Sec. 6.3

in Sec. 4.5.4.

4.5.4 Edge Studies

The region at the edge of tokamak plasmas exhibiting a steep gradient in plasma density and temperature in the low confinement regime (L-mode) and a density- and temperature-pedestal in the high confinement regime (H-mode) is crucial for the understanding of confinement states, transport and plasma–wall interactions. Cross-field transport across the last closed flux surface (LCFS) and the near Scrape-Off-Layer (SOL) is believed to be directly linked with the global confinement properties of the plasma [85, 86, 87, 33], as well as the physics of the L-H transition itself. In the open field line region, particle transport is found to be dominated by intermittent events – radially propagating plasma "blobs"– in nearly all types of magnetically confined plasmas [88, 71, 62, 89, 90, 69]; and although recent experimental studies on low pressure devices [61] have linked the formation mechanism of these structures to theoretically expected instabilities, blob-generation in tokamaks is still not well understood.

Nevertheless, recent experiments on Alcator C-Mod [34] have revealed a number of connections between global operating parameters (density and temperature profiles, plasma currents) and dimensionless scaling parameters of electromagnetic turbulence. These advances have led to the hypothesis that edge transport physics is described as a system near marginal stability [5, 91]. Therefore, both electromagnetic instabilities and critical gradients are of interest since they are thought to play a decisive role inside the LCFS determining the width of the edge gradient in all confinement regimes. Moreover, in the low-field-side pedestal, decidedly mode-like plasma responses, such as the Quasi-Coherent Mode of the Enhanced D-Alpha (EDA) H-mode [92] are found, which are known to drive particle transport [20]. How these modes develop and what their connection is to edge turbulence remains a question.

Finally, all the above dynamics and their dependence on plasma density (or collisionality) are thought to play an essential role in the physics that sets the robust Greenwald density limit [10]. With that together with the transport phenomenology

described in Section 2.2 as motivation, in this section we describe the dependence of the edge turbulence characteristics upon electron density normalized to the Greenwald density.

The structure and behavior of edge and SOL turbulence has been studied for a wide range of plasma parameters. Here we focus on LSN Ohmic L-mode discharges with I_p parallel to B_T and $\mathbf{B} \times \nabla \mathbf{B}$ towards the active X-point. Comparison between the general turbulence trends of LSN and USN discharges from the campaign of 2006-2007 showed very little differences, therefore we make no further reference to USN plasmas in the main discussion of this thesis[3]. Magnetic equilibria were set up for a range of plasma currents $0.4\text{MA} < I_p < 1.0\text{MA}$, and toroidal magnetic fields $2.6\text{T} < B_T < 6.8\text{T}$. Line averaged density $-\bar{n}_e-$ scans were performed at various combinations for $0.15 < \bar{n}_e/n_G < 0.45$, where $n_G(10^{20}\text{m}^{-3}) = I_p(\text{MA})/(\pi a^2(\text{m}^2))$ is the Greenwald-limit [93]. For the majority of discharges the safety factor at 95% of the flux was held constant at $q_{95} \approx 5$ but in the graphs showing collections of data from the scans, fixed B_T and scanned I_p data are included as well in order to separate out any potential current-related effects.

The *edge* turbulence spectra for positive k_θ plotted in Figure 4-16 show a number of remarkable features. Qualitatively, spectra scale with the Greenwald fraction: a high value of $\bar{n}_e/n_G$ gives a higher relative fluctuation level in the edge plasma. Figure 4-17 gives a more quantitative view on this scaling, showing the total relative fluctuation level above 50 kHz from the positive k_θ side of spectra. The lower limit on the integration is chosen so as to exclude any contamination from the negative k_θ side, due to finite resolution.

The result shows a sensitive dependence of the turbulence power on Greenwald fraction, with a sharp increase in power around $\bar{n}_e/n_G = 0.25$ making a strong connection to the observations of the cross field transport summarized earlier [5] and [34]. In these studies the density profile of the SOL was found to systematically flatten and its average density to increase as the line averaged density of the main plasma,

[3]For the special case of H-mode-unfavorable $\mathbf{B} \times \nabla \mathbf{B}$ directions and the closely related I-mode phenomenon, see App. A; and for the different effects of radio-frequency waves on the SOL in USN and LSN configurations, see Sec. 6.3

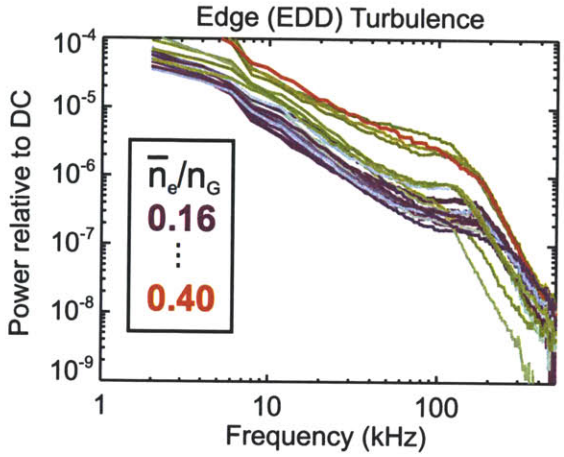

Figure 4-16: Edge turbulence spectra normalized to average brightness values with a $k_\theta > 0$ filter for $0.15 < \bar{n}_e/n_G < 0.45$. The curves are color coded for Greenwald fraction in a rainbow scheme going from low F_{Gr} (blue) to high (red). Lower F_{Gr} curves generally fall under the higher F_{Gr} ones.

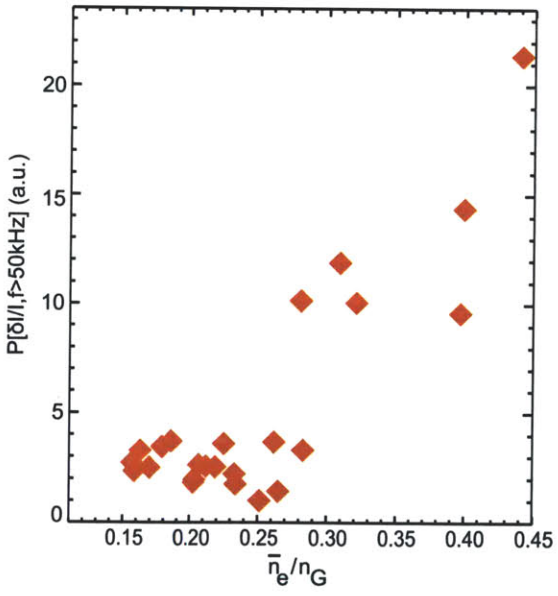

Figure 4-17: Sum of the fluctuation power relative to the DC level above 50 kHz from the EDD turbulence.

and consequently F_{Gr} increased. This provides further evidence to the claim in the above references that n_G is in fact a limit set by turbulent transport, but indicates as well that the key region for the turbulent transport is the edge, indeed the turbulence with positive k_θ in the edge. More will be said about the effect of the edge turbulence on SOL spectra and the far SOL density in Sec. 4.6 upon comparison to H-mode results. For now we continue interpreting the edge spectra.

All curves in Fig. 4-16 exhibit an unmistakable break in slope. The frequency values at which these breaks occur cover a wide range from 100 kHz to just above 300 kHz. However, since the k_θ-f spectra are well fitted by a constant propagation velocity, one can evaluate the spatial scales of the break in slope simply as

$$k_\theta = \frac{2\pi f}{v_{EDD}}.$$

This is advantageous considering that the time resolution of our system far exceeds its spatial resolution capabilities. The wavenumber scales are especially useful to consider since the wavenumber is unaffected by the choice of the reference frame. The literature of theoretical treatment of edge turbulence on the other hand prefers $k_\perp \rho_s$ as a parameter, for its significance in the equations describing drift-wave turbulence [39] (ρ_s is the ion gyro-radius at the sound speed). The characteristic values found experimentally fall in the range $k_\perp \rho_s \in [0.09, 0.17]$ (cf. ref. [39] where this is the range both in $k_\perp \rho_s$ and α_d where both drift waves and interchange instabilities may be important). Further, we find that even after adjusting for the propagation speeds and normalizing the resulting break in slope wavenumber k_θ^c to the sound gyro-radius, a trend remains in the $k_\theta^c \rho_s$ values. This trend is shown in Figure 4-18 with $k_\theta^c \rho_s$ showing a slight decrease as F_{Gr} increases. These break in slope wavenumbers then lend themselves as division points for further inspection of the spectra: the reason why they might represent the scale of energy injection is that spectral transfer is expected to be different towards larger structures than towards smaller ones, and even if these critical wavenumbers cannot be identified as such, their importance remains as the spatial scale where factors of turbulence drive and dissipation change essentially.

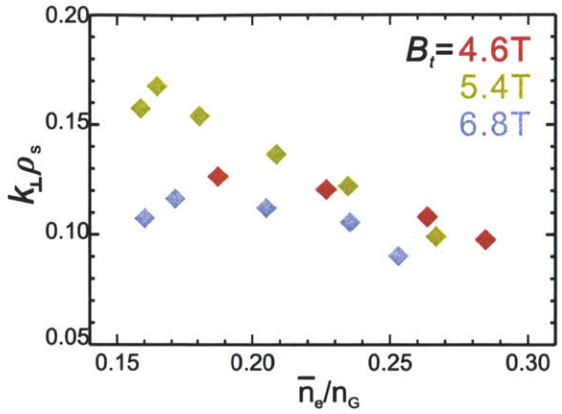

Figure 4-18: Drift-normalized wavenumbers of the break in slope in the edge turbulence spectra from $q_{95} = 5$ discharges.

One conspicuous feature of the power spectra above this point is that they all show a power-law decay $S(f) \propto f^{-\beta}$, a tendency considered customary after the formulation of the Kolmogorov-scaling, but demonstrated here only above 200 kHz. The decay exponents, or spectral indices, of the spectra from all experiments were determined by least-square fits, which provided values of $\beta = 4.1 \pm 0.4$. Below the break in slope, on the other hand, a considerable variety of spectral shapes is seen, with the trends as a function of F_{Gr} shown in Fig. 4-19.

At low Greenwald fractions, we find that the spectrum has a slight, sometimes even a pronounced peak at the high frequency ($\sim$ 200kHz) end of the spectra. We will return to discussing the significance of this point. As the Greenwald fraction increases, this feature becomes a plateau, eventually giving way to a fully developed turbulent spectrum, in which it is manifested as the break in slope. Meanwhile, the overall turbulence intensity increases as noted above. Thus the positive k_θ turbulence in the edge responds quite sensitively to changes in the Greenwald fraction, filling in more and more size scales with higher and higher intensities as the density increases.

So far we have concentrated on the propagation and the behavior of the edge turbulence, but the trend of the poloidal propagation velocities of the SOL turbulence with Greenwald fraction can also help strengthen our understanding. Figure 4-20 shows trends in the poloidal velocity of the SOL turbulence from the 2007 campaign together with recent results. At the Greenwald fraction where the edge turbulence

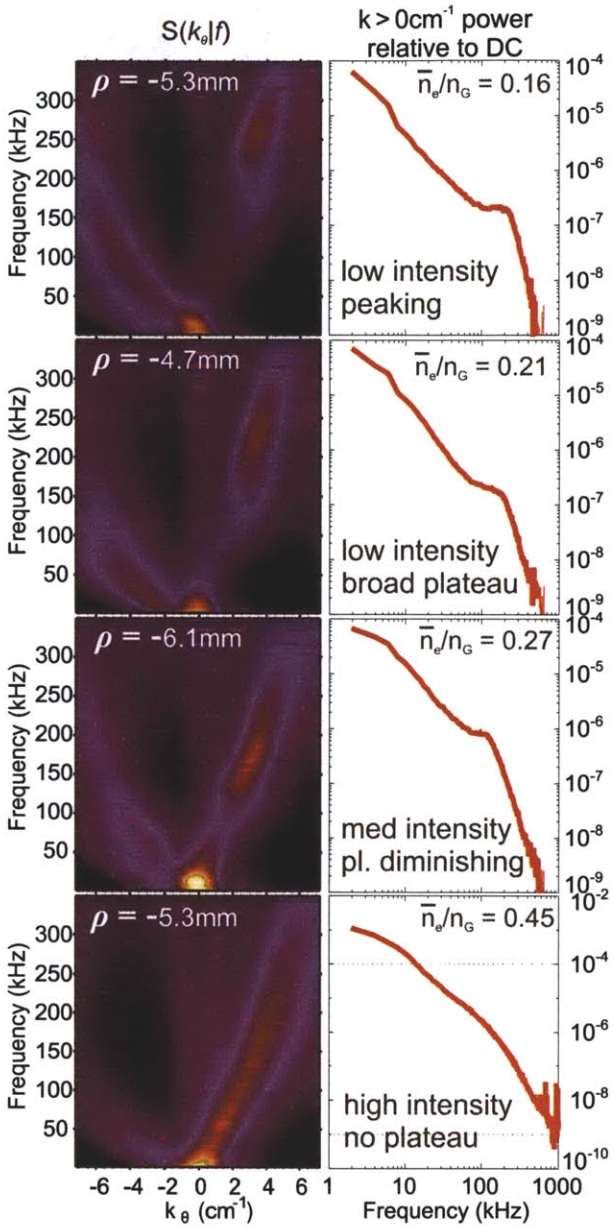

Figure 4-19: Conditional wavenumber–frequency spectra from the edge region of L-mode plasmas, plotted for a wide range of Greenwald fractions. The corresponding turbulence spectra on the right show only the positive k_θ component in order to filter the data from any effects caused by the blobby SOL component which is subdominant in this region. The intensity of the turbulence goes up rapidly at $F_{Gr} \approx 0.25$

starts to grow, the phase velocities in the IDD direction decrease for each value of magnetic field. The trend supports our statement that the far SOL blob velocity is $\mathbf{E} \times \mathbf{B}$.

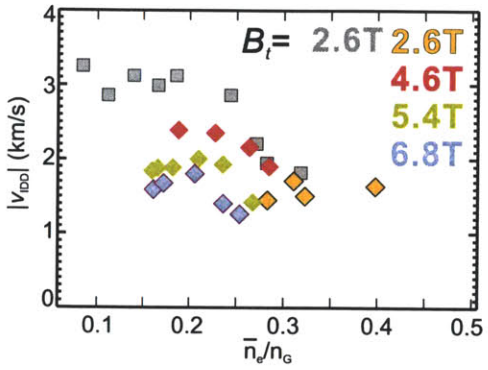

Figure 4-20: Measured propagation velocities in the SOL in the ion diamagnetic drift direction against Greenwald fraction at different toroidal fields. The low F_{Gr}, high speed points at 2.6T are from the 2007 campaign, all others are from the present experiment.

In view of Ref. [5] the edge-SOL system is considered to exist at a critical α_{MHD}, normalized pressure gradient. If however the density increases, ∇T_e is expected to decrease unless completely different physics (like H-mode) enters. But $E_r \propto \nabla T_e$ in the SOL, therefore v_E is expected to decrease with density. Moreover there is also a clear decreasing tendency with toroidal field, qualitatively consistent with $v_E = E_r/B_T$.

Given the observations [34] of increased particle transport with increased F_{Gr}, the new observations regarding the dependence of *edge turbulence* on F_{Gr} suggest a close connection to edge particle transport. The behavior of cross-field edge transport, on the other hand, shows even more dramatic changes as the plasma undergoes an L-to-H transition. Therefore the edge fluctuations during the transition were also studied.

H-Mode

Studies of the edge turbulence in the L-H transition were conducted in LSN discharges, with $\mathbf{B} \times \nabla \mathbf{B}$ in the direction favorable for transitions, i.e. toward the active X-point. Both Ohmic and Ion-Cyclotron-Range-Frequency (ICRF) heated H-modes were studied. In Ohmic H-modes, the transition was triggered by ramping the toroidal field down to $B_T = 2.8$ T, subsequently raising the field back to a value that put

$q_{95} > 3.3$ to facilitate access to the Enhanced D-Alpha H-mode (EDA) [85, 94]. In order to exclude any effects having to do with changing values of the field, or the safety factor, we also studied ICRF heated H-modes with a fixed magnetic field of $B_T = 5.4$ T and a heating power of $P_{RF} = 2.5$ MW triggering the transition. As long as the safety factor value does not inhibit the onset of an EDA H-mode, the transition sequence is roughly the same in both Ohmic and ICRF heated H-modes: L-mode $\rightarrow$ ELM-free H-mode $\rightarrow$ EDA H-mode, so all three regimes are studied in each case. In no case were there discreet Edge Localized Modes (ELMs) [18, 4] observed.

Differences in the turbulence and turbulent fluxes have been noted in a number of studies (see e.g. [95], [96], or the review [97] and the references within). The prominent changes found in the edge turbulence as the above sequence occurs are demonstrated in Figs. 4-22 and 4-21. The L-mode turbulence spectrum plotted in the figure has a $k_\theta^c \rho_s = 0.13$. ELM-free H-modes exhibit a much reduced outward cross-field transport, both main species and impurity density increases roughly linearly with time in such plasmas, eventually leading to radiative collapse unless another H-mode regime is accessed. In this phase, the k-filtered spectrum reveals that the positive k_θ features decrease by over a factor of 10 in power. Filtering known sources of noise brings back a faint $k_\theta > 0$ feature at $f > 250$ kHz with a poloidal propagation velocity of ~ 25 km/s, approximately consistent with the results of ref. [6] (derived using Charge-Exchange-Recombination-Spectroscopy) where the E_r in the edge of ELM-free plasmas is found to be on the order of 100kV/m, yielding $v_E \approx 20$ km/s. Due to the low intensity, however, no radial velocity profile has yet been assembled, therefore the match to CXRS results is still somewhat limited. As the transition from ELM-free to EDA H-mode occurs, the QCM appears on the positive k_θ side in the edge with $k_\theta^{QCM} \rho_s = 0.11$, which is suggestive of a connection between the underlying instability of the QCM and the β-break scale of the L-mode turbulence. A connection is further reinforced by the fact that spectral powers at frequencies and wavenumbers somewhat smaller than those of the QCM remain reduced compared to L-mode levels, perhaps pointing to inhibited spectral transfer, which may be the

reason the QCM can grow strong. The QCM is known to be responsible for increased cross-field particle transport [20], and is now suggested as a further manifestation of the underlying drive of L-mode edge turbulence. One further argument for the edge turbulence, as opposed to the SOL turbulence being responsible for this transport is made by following the evolution of the SOL spectra through the transition. The negative k_θ (IDD propagating) spectra of the SOL turbulence (the blobs) *are invariant through these important changes* when normalized to the average brightness levels, as is evident from Fig. 4-23.

The above results have been reproduced for both the Ohmic and the ICRF heated H-mode discharges. No significant changes were found, adding to the correlation of strong cross-field particle flux and *edge* turbulence.

4.6 Discussion of primary results

Using fast (2 MHZ) 2D Gas-Puff-Imaging viewing the 4 cm radial region at the low-field-side of Alcator C-Mod, we examined the turbulence both in the edge and in the SOL. We distinguished two connected but distinctly different regions in L-mode plasmas: in the *edge* inside the LCFS, the dominant broadband turbulence propagates poloidally in the electron diamagnetic drift direction. In the far SOL the turbulent structures (blobs) move poloidally in the opposite direction, consistent with the $\mathbf{E} \times \mathbf{B}$ direction and magnitude there. We presented evidence that it is primarily the turbulence of the edge region that is closely linked with cross-field particle transport in this region. Poloidal-wavenumber–frequency spectra from the edge are found to be well approximated by a linear dispersion relation allowing to express power spectra as a function of $k_\theta = 2\pi f / v_{EDD}$, which is not subject to any Doppler-shifts. Results show a clear break in slope of power vs k_θ at k_θ^c with $k_\theta^c \rho_s = 0.09 - 0.17$ over a range of magnetic fields and densities. Below this value, there is a clear dependence of the spectra upon Greenwald fraction, with the power of the turbulence increasing with $\bar{n}_e / n_G$, and the power at wavenumbers lower than the characteristic k_θ^c filling in as the edge becomes more turbulent and spectral transfer

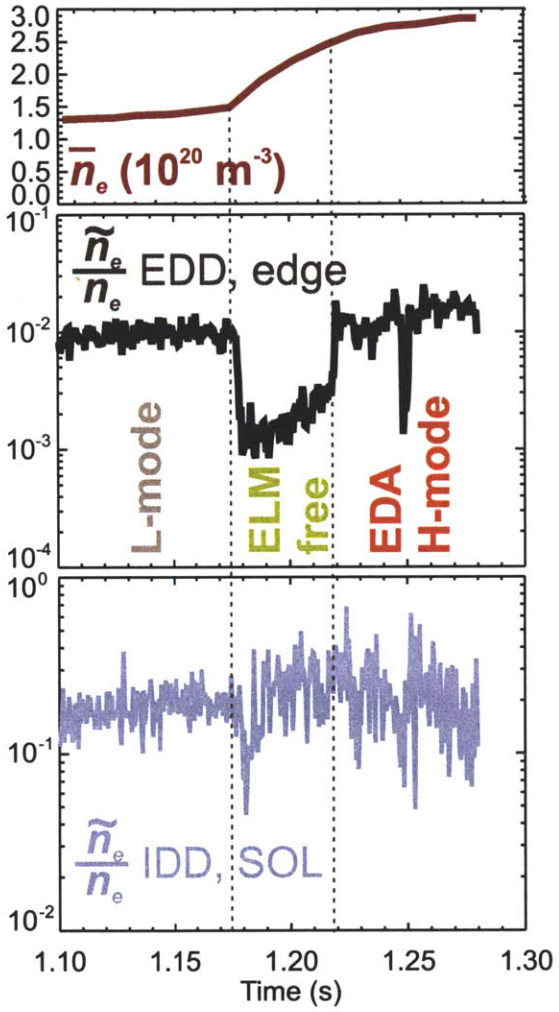

Figure 4-21: Observation of an Ohmic low- to high-confinement transition, with the characteristic sudden density increase marking the onset of the ELM-free H-mode; the trace of $\tilde{n}/n_0$ from the edge region shows a marked decrease during this regime, and is restored to almost the L-mode level in EDA H-mode, while the SOL trace shows no such transition.

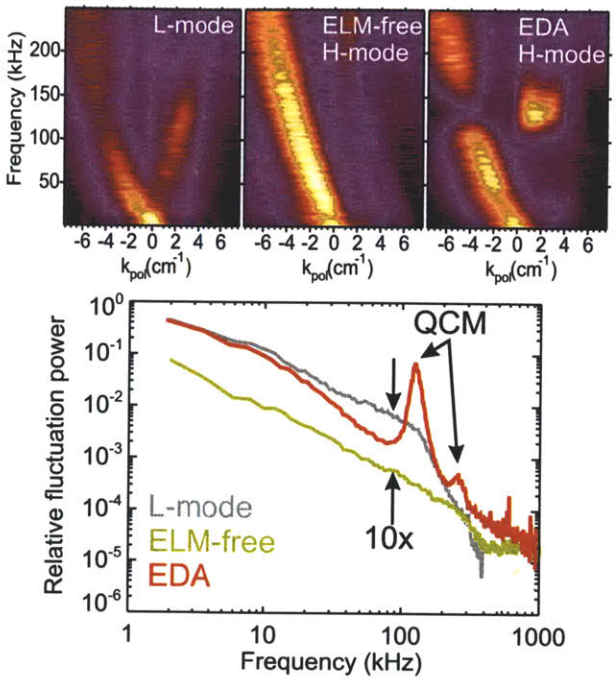

Figure 4-22: Changes in the edge turbulence spectrum at the L-to-H transition. The top part of the figure shows conditional k-f spectra (normalized to every band in frequency), from the edge of an Ohmically heated plasma undergoing a transition in (from left to right) the L-mode, the ELM-free H-mode and the EDA H-mode phases. The single lobe in the ion diamagnetic drift direction is not getting stronger in the middle graph, the increased visibility is an artifact of the normalization, and so is the apparent dip in the same lobe at the frequency of the QCM. The bottom figure shows the k-filtered spectra from the three regimes, with a $\sim 10\times$ drop in power from L-mode to ELM-free, and the QCM appearing at the breaking point of the spectrum in EDA.

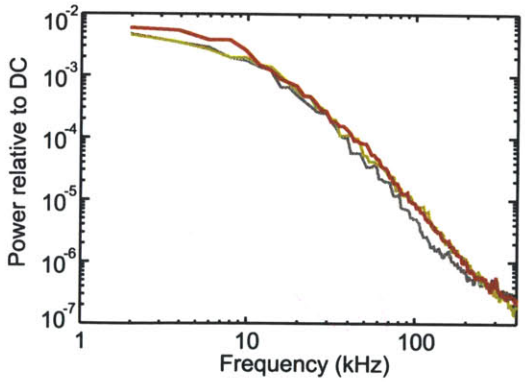

Figure 4-23: The power spectrum of the SOL turbulence relative to the DC brightness level. The L-mode, ELM-free H-mode and EDA H-mode spectra are essentially indistinguishable.

is enhanced. In ELM-free H-mode plasmas, this turbulence shows a dramatic drop in power and speeds up to $\sim$ 25km/s, approximately consistent with a concurrent increase in the E_r-well depth there. If the ELM-free H-mode evolves into an H-mode with a QCM, the QCM develops in this region with $k_\theta^{QCM}\rho_s = 0.1$, suggesting a possible connection with the turbulence input scale seen in L-mode. The SOL turbulence on the other hand seems largely unaffected by even the changes brought about by the L-H transition, as shown in Fig. 4-23. This result merely underlines the importance of edge turbulence and is *not* inconsistent with previous findings from C-Mod [20, 41] and other tokamak experiments [95, 96], in which the frequency or intensity of blobs, or the particle flux was observed to drop in the L-H transition. It needs to be emphasized, however, that the spectra in Fig. 4-23 are normalized to the average brightness level, and therefore the one from the higher confinement plasma, i.e. lower SOL density does represent an *absolute* drop in either blob frequency or intensity. Previous studies have also shown that plasma in the far SOL is primarily the result of blobs born near the LCFS (see e.g. [71]), explaining how invariant normalized spectra can still represent different particle fluxes from the edge region. The spectra are normalized to average brightness and not SOL density, but as is shown in Appendix B, the weak-temperature dependence along with the relative constancy of the temperature of this region in all regimes makes it possible to consider the two normalizations equivalent here. The new observation also ties in well with previous results from Alcator C-Mod, especially in ref. [34] where density in the far SOL is shown to systematically fill in relative to the edge at Greenwald fractions $F_{Gr} \approx 0.3$, indicating an enhanced cross-field particle transport. Here we show the relative intensity of the *edge* turbulence increasing at a similar value of F_{Gr}.

Even though it is not possible to know from these measurements the exact physics of the underlying instability for blob generation, the picture that is starting to take shape from these findings and those of [5, 91] seems very similar to the one presented in [61], and is roughly the following. The edge density and temperature profiles are set by gradient limiting transport mechanisms. This manifests itself as the QCM in EDA regimes, and perhaps through spectral transfer from this instability to larger

features, as broad-band turbulence in L-mode. This development towards larger features is hindered if: a) n_e/n_G is very small (peaked spectra), b) there is a strong edge flow as in ELM-free and EDA discharges. These features are wavelike, moving poloidally at a velocity set by their specific dispersion (v_D and v_E together), and their amplitude may become large enough to go beyond a critical gradient at which plasma is pushed across the field, at which point, instead of a wave motion (which does not involve poloidal particle drift) separate blobs of plasma travel through the SOL following v_E of that region.

Of course this conjecture is not complete. Not only does it not identify the underlying instability, it also gives no explanation to the existence of the IDD propagating feature in ELM-free H-mode as deep as $\rho = -1.5$ cm where the $v_E \approx 25$ km/s. This point raises possibility of "contamination" of the measurements by the intrinsic, non-localized D_α emission or of systematic instrumental effects associated with GPI. The possibilities that the IDD propagating features at $\rho \lesssim -1$ cm are due to non-localized intrinsic emission or to toroidal spreading of the local gas puff, leading to emission along the line-of-sight from a $\rho > 0$ were examined in the spirit of Section 3.2.3. Neither possibility is quantitatively consistent with the observations. Thus at present, we have no satisfactory explanation for the existence of the IDD feature well inside the LCFS and coexisting with the EDD feature.

4.7 Bispectral Techniques

In the previous section it was conjectured that the k_θ^c critical poloidal wavenumber at which the EDD power spectra of the edge plasma turbulence exhibit a sudden increase of the decay index β might in fact be the scale length at which the turbulence is driven. The evidence for this presented so far is admittedly circumstantial and is based on the observations that

a) in the wide literature of turbulence it is customary to refer to such breaks in the slope of power spectra as the scale of energy injection [48, 98, 99, 56]. This originates from the theory of two-dimensional fluid turbulence by Kraichnan[36].

The key difference found between three- and two-dimensional turbulence is the behavior of the *enstrophy*, or the square average of the vorticity $\nabla \times v$. In three dimensions only energy is conserved, not enstrophy, and it is found to be transported from large to small scales [58], which is known as the direct cascade. 2D fluid turbulence conserves the enstrophy, and accordingly exhibits a dual cascade: energy is transferred from small scales towards large ones (inverse cascade) and enstrophy is transferred from large to small scales (direct cascade). Due to the rapid equilibration along the magnetic field, turbulence in a magnetized plasma is often expected to be similar to 2D fluid turbulence. The generalized energy and enstrophy of these systems, such as in a Hasegawa-Wakatani [38, 100] turbulence or one of many two-nonlinearity models [101, 102] in the case of plasma turbulence, are conserved and thus the spectral transfer dynamics is predicted to be different towards smaller structures and larger ones, causing different statistical equilibria for structures which are larger than the drive scale and those which are smaller;

b) in the case of low plasma density, the scale and frequency at which the break in the slope in the log-log sense occurs shows up as a peak in the spectrum, which could be an indication of the existence of an actual unstable mode;

c) the normalized wavenumber $k_\theta \rho_s$ of this candidate mode is the same as that of the QCM forming in the EDA H-mode, a clear, coherent mode which exists in the same physical region as the EDD turbulence of the L-mode plasmas.

In this section both L-mode and EDA H-mode plasmas are studied in terms of their spectral transfer processes in order to provide additional evidence for or against the claim that the observed k_θ^c represent a turbulence driving scale. To first order this approach regards turbulence as a system of waves which arises from an instability of the underlying system, followed by wave-wave interactions at a non-linear stage. When this nonlinearity is a quadratic one (as explained below), this transfer process is known as three-wave interactions.

4.7.1 Frequency Space

Whether or not the spectrum is formed via spectral transfer from a given scale via three-wave interactions cannot be decided using only the shape of the power spectra. For example the two signals

$$y_{nl}(t) = [x(t)]^2 = [\cos(\omega_1 t + \theta_1) + \cos(\omega_2 t + \theta_2)]^2 \tag{4.5}$$

$$y_{lin}(t) = 1 + \cos(\omega_a t + \theta_a) + \cos(\omega_b t + \theta_b) + \frac{1}{2}(\cos(\omega_c t + \theta_c) + \cos(\omega_d t + \theta_d)) \tag{4.6}$$

will have the exact same power spectrum so long as $\omega_a = \omega_1 + \omega_2$, $\omega_b = \omega_1 - \omega_2$, $\omega_c = 2\omega_1$ and $\omega_d = 2\omega_2$; with random and independent phase angles θ_i for all i. Yet, $y_{nl}(t)$ is the product of a quadratic nonlinearity, whereas $y_{lin}(t)$ is a perfectly linear signal, with no interaction between any components. The phase angles $\theta_1 + \theta_2$, $\theta_1 - \theta_2$, $2\theta_1$ and $2\theta_2$ of the individual components in $y_{nl}(t)$ with frequencies $\omega_1 + \omega_2$, $\omega_1 - \omega_2$, $2\omega_1$ and $2\omega_2$, respectively, obviously depend on *only two* phase angles in the input signal $x(t)$ and hence only two independent phases can be found in $y_{nl}(t)$; therefore the phases between individual components will be locked. Such components of a power spectrum are said to be "phase coupled".

The bispectrum is the simplest of the higher order spectra, which is used in many applications ranging from interpreting EEG (electroencephalogram) signals to identification of radar signatures to plasma science, exactly to provide quantitative information on the phase coupling in the observed signal. In terms of sample statistics, it is the Fourier transform of the second order correlation function, and is therefore given by

$$B(f_1, f_2) = \left\langle X(f_1)\, X(f_2)\, \overline{X(f_1 + f_2)} \right\rangle, \tag{4.7}$$

where $X(f_i)$ is the full complex Fourier-spectrum of the recorded signal, the bar means complex conjugation and the angled brackets stand for an average over realizations. The average can be over an ensemble or time as as long as the distributions are stationary. The averaging is crucial in the definition since it ensures that complex

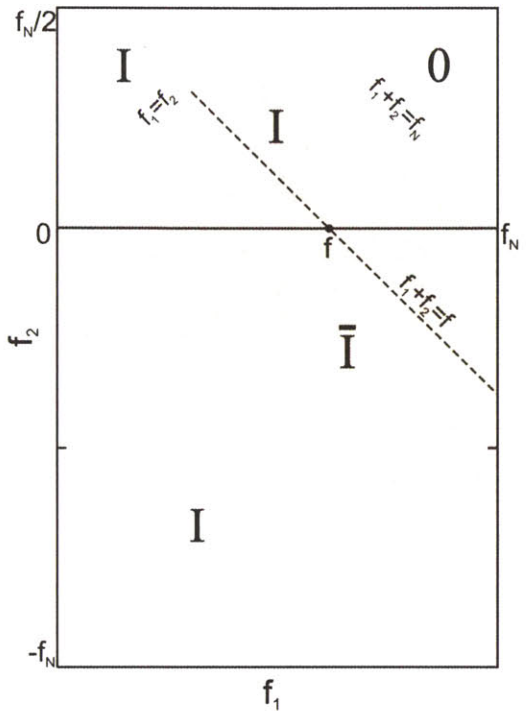

Figure 4-24: Full period of a discrete bispectrum. The shaded area indicates the components of frequencies (f_1, f_2) where cross-bispectra of the form $\langle XXY \rangle$ are both meaningful and non-redundant; the triangles labeled "I" can all be mapped into the the top part of the shaded region where the auto-bispectrum is not redundant, and the same holds for the complex conjugate of "$\bar{\text{I}}$". The region labeled "0" must vanish for any stationary signal. The dashed line represents a line along which the summation occurs when generating $\Sigma b^2(f)$.

triple products $X(f_1)X(f_2)\overline{X(f_1+f_2)}$ with random phases, i.e. those with independent phases for the three spectra, average to zero while the phase coupled components produce a finite (complex) value. The bispectrum is therefore quite sensitive to noise and depending on the SNR of the sample signals the number of realizations necessary for a well converged bispectrum must be determined. In addition, stationarity of the distributions of the signals used in the averaging must be ensured, since non-stationary signals can obviously cause non-cancelations, thus significantly altering the bispectrum. Stationarity was tested both in the statistical sense of Section 4.1 and with the steadiness of the power spectra, and for the high contrast, high SNR signals used here, good convergence was found to occur above a sample size of $\sim$ 200 bins (epochs) in a spectrogram of $df = 2$ kHz.

The auto-bispectrum (4.7) is inherently symmetric in f_1 and f_2, so most graphs include only the non-redundant part where $f_1 > f_2$. For the discrete bispectrum calculated from a finite length stationary signal sampled at $2f_N$, where f_N is the Nyquist frequency, components $f_N - f_1 < f_2$ will be zero[4], and therefore they also are not typically shown. It is possible to extend the bispectrum to difference-interactions, where the frequency in the argument of the complex conjugated term is the difference $f_1 - f_2$ using $X(-f_2) = \overline{X(f_2)}$. It can be seen that the auto-bispectrum is conjugate-symmetric between sum- and difference interactions with the canonical mapping $f_1 = f + f'$, $f_2 = f'$, since

$$\begin{aligned} &X(f_1)X(-f_2)\overline{X(f_1 - f_2)} = X(f_1)\overline{X(f_2)X(f_1 + f_2)} \\ &= X(f + f')\overline{X(f')X(f)} = \overline{\left[X(f)X(f')\overline{X(f + f')}\right]}. \end{aligned} \tag{4.8}$$

The region of difference interactions becomes meaningful though for cross-bispectra, in which the conjugate term is a spectrum different from $X(f)$. Figure 4-24 illustrates the regions of non-redundant components for auto- and cross-bispectra.

Since the amplitude of a component in the bispectrum depends on the amplitude of the respective Fourier components as well as the degree of phase coupling between them, it is often useful to normalize the bispectrum to the power spectra and get

$$b^2(f_1, f_2) = \frac{|B(f_1, f_2)|^2}{\langle |X(f_1)X(f_2)|^2 \rangle \langle |X(f_1 + f_2)|^2 \rangle} \tag{4.9}$$

the bicoherence square, which is normalized to run between 0 (no phase coupling) and 1 (the component is due to phase coupling entirely). It is also informative to calculate the total phase coupling into a particular frequency component f from any pair of f_1 and f_2:

$$\Sigma b^2 = \sum_{f_1 + f_2 = f} b^2(f_1, f_2), \tag{4.10}$$

which is commonly known as the summed bicoherence square; the summation is

[4]The components *can* in fact be calculated since the bispectrum inherits the periodicity of the discrete Fourier transforms. The region provides an opportunity for an additional test of stationarity [103]

customarily carried out over difference frequencies as well. The importance of this summation for the interpretation of coupling processes has been pointed out before [104], and will be seen in more detail in the sections that follow.

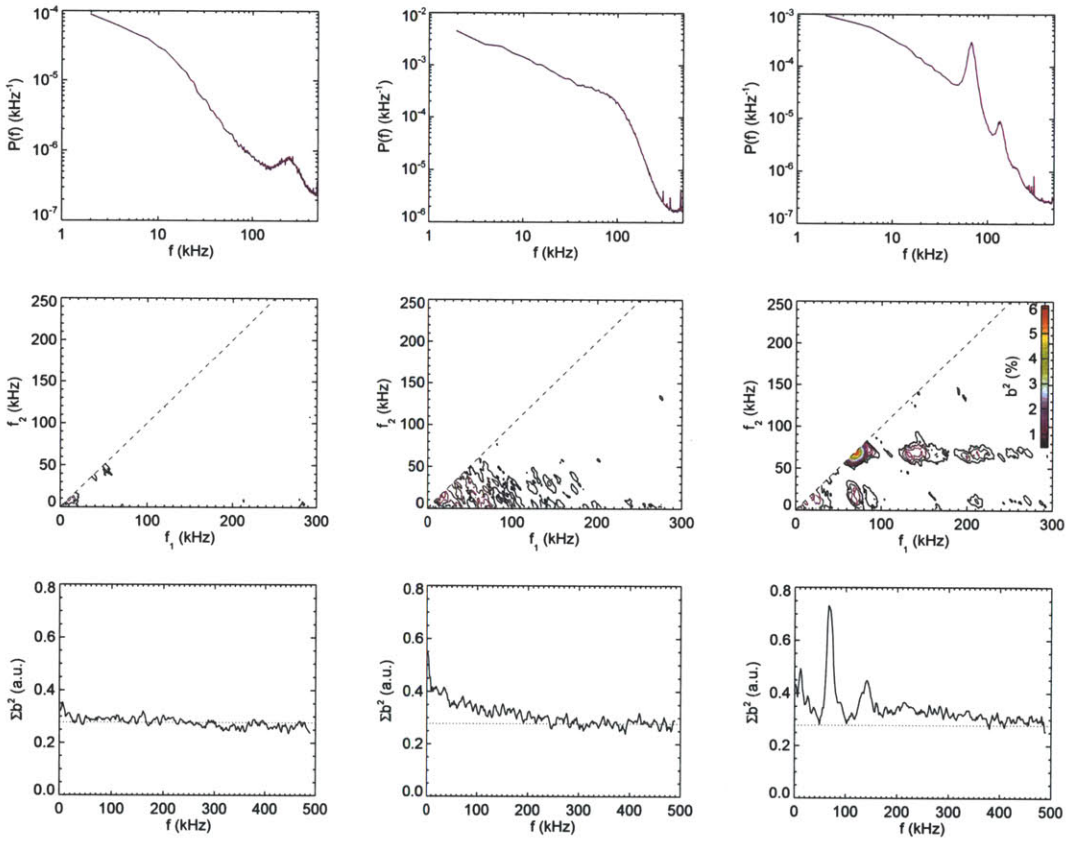

Figure 4-25: Phase coupling relations in the edge plasma turbulence of a low density, low beta Ohmic L-mode (left), a relatively higher density and beta Ohmic L-mode (middle), and an EDA H-mode (right); the power spectra of the EDD moving edge fluctuations are plotted for reference (top) with a relative fluctuation level scale ($\delta n/n_0$); the bicoherence spectra (middle) of the three discharges have contours at the same levels between half a percent and 6%; the summed bicoherence squares (bottom) have the same scales.

Figure 4-25 shows the auto-bicoherence $b^2(f_1, f_2)$ and summed bicoherence $\Sigma b^2(f)$ along with the respective power spectra of the signals they came from in three characteristic cases. First, plotted in the left-hand column of Figure 4-25 are analyses of a low density, low normalized pressure (beta) ($\bar{n_e} = 5.3 \times 10^{19}$ m^{-3}, $I_p = 400$ kA, $B_T = 5.2$ T, $F_{Gr} = 0.19, \beta_p \simeq 0.1, \nu^* \simeq 5$) Ohmic L-mode in which the

EDD spectrum exhibits a clear peak at ~ 250 kHz, and the overall turbulence power is low. The middle column is the analysis of a higher density and higher beta ($\bar{n_e} = 9.3 \times 10^{19}$ m$^{-3}, I_p = 800$ kA$, B_T = 5.4$ T$, F_{Gr} = 0.25, \beta_p \simeq 0.2, \nu^* \simeq 7$) Ohmic L-mode in which the EDD spectrum has a fully developed low-frequency–low-wavenumber portion with a break in slope at ~ 100 kHz and significantly higher power. Finally in the right-hand column are the corresponding plots for an EDA H-mode ($I_p = 800$ kA$, B_T = 5.4$ T$, \bar{n_e} = 2.5 \times 10^{20}$ m$^{-3}, \nu^* \simeq 2.5$). In all three cases a 200 ms long sample was analyzed, which at the common $df = 2$ kHz frequency resolution makes the number of realizations 40, a factor of two higher than the minimal number for convergence of $B(f_1, f_2)$ to ensure the data shown is reliable. A number of remarkable features are found.

Firstly, two out of the three cases show a clear indication of the presence of nonlinearity. While the lowest density discharge (left-hand column of Figure 4-25) provides a basically completely featureless bicoherence spectrum – the average value of which is drawn as a dotted line in the $\Sigma b^2(f)$ parts of Fig. 4-25 as a reference – the higher density L-mode (middle column) has significant, non-noise components below the break in slope frequency of $f \sim 100$ kHz. This supports the conjecture at the end of the previous section, since it indicates that there are stronger nonlinear interactions in the edge plasma turbulence in the case when the low-frequency–low-wavenumber part of the spectrum is filled in as opposed to in the low density case when there is a distinct peak at the $k_\perp \rho_s \sim 0.1$ scale. Note also that these interactions are concentrated in the frequency region *below* the break-in-slope frequency (wavenumber), indicating very little coupling forward from this scale.

The strongest phase coupling is found in the EDA H-mode fluctuations, where the strong peak at $f_1 = 70$ kHz, $f_2 = 70$ kHz is the strong coupling from the fundamental frequency of the QCM to its harmonic, showing that the second peak in the spectrum is a true nonlinear harmonic of the QCM. Evidence of further interactions are found between the fundamental and the first harmonic into the second and even a third harmonic, the latter of which is not even discernable in the power spectrum alone. Again, as in the case of the higher density L-mode, there are interactions up

to the frequency of the QCM, which still does appear at approximately the same dimensionless wavenumber ($k_\theta \rho_s$) as do the spectral features of the L-modes. Consistent once more with the hypothesis about the transfer dynamics in the previous section, the total level of this coupling is lower than in the fully developed L-mode situation (middle column). Furthermore, there are now strong interactions forward from the $k_\perp \rho_s = 0.1$ scale. In Appendix A the scaling properties of these interactions will be discussed in more detail, here we only wish to concentrate on the above key differences between L-mode and H-mode signatures in order to support the notion of the relation between the source of the L-mode turbulence and the QCM.

4.7.2 2-Dimensional Bispectra

Considering that the power spectra in wavenumber and frequency $S(k_\theta, f)$ at most physical locations considered in this thesis exhibit both an IDD and an EDD propagating feature, it is reasonable to ask whether the phase coupling – whose existence was shown in the previous section – occurs between the counter-propagating features of the edge fluctuations or if it is primarily concentrated within one single lobe of the k–f distributions. Most experimental studies of nonlinearities (with the exception of some excellent, recent work [105, 100]) in the literature of edge plasma fluctuations cannot provide any information on this, since they are often carried out at single locations or otherwise lack the required spatial resolution or SNR. The new GPI diagnostic, however, enables us to study phase coupling in a 2-dimensional sense.

When calculating bicoherence spectra in two dimensions, matching conditions in both wavenumber and frequency have to be fulfilled, i.e. in the definition of the 2D bispectrum

$$B\left(k_1, k_2, f_1, f_2\right) = \left\langle X\left(k_1, f_1\right) X\left(k_2, f_2\right) \overline{X\left(k_3, f_3\right)} \right\rangle, \tag{4.11}$$

$k_3 = k_1 + k_2$ and $f_3 = f_1 + f_2$ have to hold, corresponding to the conservation of wave momentum and wave energy in terms of the three-wave interaction. Since the full 2D bicoherence spectrum is a four-dimensional object, and also because in the case where $S(k_\theta, f)$ are fairly narrow (such as the ones considered throughout this thesis), most

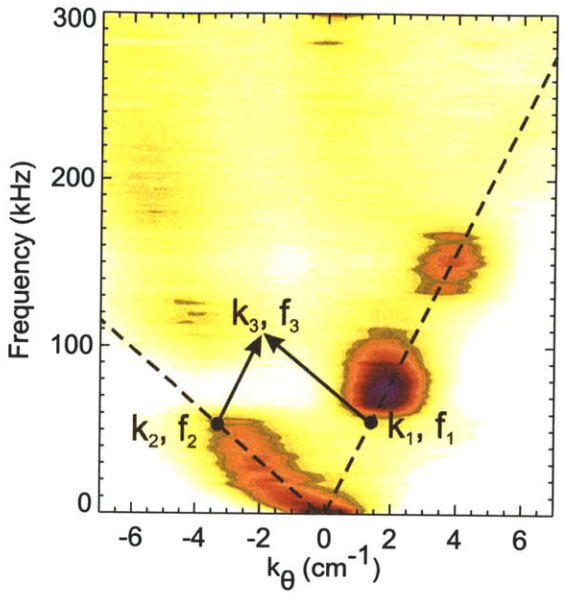

Figure 4-26: Schematic showing the construction of a two-dimensional bicoherence spectrum with interactions that conserve wave energy and momentum, from two slices of the 2D spectrum $S(k_\theta, f)$ with fixed phase velocities. the resultant component has k_3, f_3 and in general a phase velocity different from that of both contributing components. The schematic is superimposed on a conditional spectrum $S(k_\theta|f)$ from an EDA H-mode.

of that 4D space is featureless, it is far more instructive to compute specific slices of the full bicoherence spectrum. If a given wavenumber (frequency) range is of interest, one of the wavenumbers (frequencies) may be fixed, thus making the visualization of the spectrum possible. Alternatively, one may concentrate on the k–f regions of highest power by specifying dispersion relations for the two contributing waves. Due to the matching conditions, this will uniquely determine the resultant wave's dispersion. The simplest case of a linear dispersion (which is a good approximation for the high power spectral regions in the majority of the plasmas analyzed for the thesis) will be considered here.

Figure 4-26 demonstrates on a conditional spectrum from an EDA H-mode which components will be chosen for the resultant wave when the contributing components are chosen from the linear dispersion fit through the highest power in $S(k_\theta|f)$, indicated as dashed lines in the figure. The bispectrum in this case can be construed as

a three-field cross-bispectrum in the sense that

$$B_{XYZ}(f_1, f_2) = \left\langle X(f_1)\, Y(f_2)\, \overline{Z(f_1, f_2)} \right\rangle$$

for

$$\begin{aligned} X(f) &= S(k_\theta = 2\pi f / v_1^{\mathrm{ph}}, f) \\ Y(f) &= S(k_\theta = 2\pi f / v_2^{\mathrm{ph}}, f) \\ Z(f_1, f_2) &= S(k_\theta = 2\pi (f_1 / v_1^{\mathrm{ph}} + f_2 / v_2^{\mathrm{ph}}), f_1 + f_2). \end{aligned}$$

Consequently, the $f_2 > f_1$ area is no longer redundant in the spectrum, except for the special case when $v_1^{\mathrm{ph}} = v_2^{\mathrm{ph}}$. For the sake of clarity on whether a regular auto-bispectrum (bicoherence) or such a velocity filtered bispectrum is being graphed, the $f_2 > f_1$ region is plotted in the figures below, as well as in Appendix A.

In Figures 4-27 through 4-30, the results of the two-dimensional bicoherence calculations are shown for the same EDA H-mode and higher density L-mode plasmas discussed above in reference to the middle and right-hand columns of Figure 4-25. The IDD propagating part of the spectra get close to the Nyquist-wavenumber k_N at approximately 100 kHz in both cases, so for the cross-bispectra between the IDD and EDD fluctuations, f_2 is cut off at that value. In EDA H-mode very little phase coupling is detected between the counter-propagating features: the only significant peak appears at $f_1 \simeq 70$ kHz, $f_2 \simeq 14$ kHz. However, a comparison to the auto-bicoherence of the EDD direction reveals that the same coupling peak exists with a degree of phase coupling that is twice as large as between the opposite directions. This suggests that the feature at $f \simeq 14$ kHz is stronger in the EDD sense, and in fact the occurrence of the same peak in the IDD-EDD bicoherence is due to the finite wavenumber width which is due to the size of the viewing array. With that in mind, we conclude that the cross-bicoherence is featureless, which means that both the coupling under the QCM frequency and above it occurs in the EDD turbulence.

A further gain of the use of the full $S(k_\theta, f)$ spectrum with velocity filtering is seen

in Figure 4-28, which shows a striking improvement from Figure 4-25 in that all the forward-nonlinearity peaks from the QCM are raised far above the noise floor, with a large $b^2 = 25\%$ at the $f_{\mathrm{QCM}} + f_{\mathrm{QCM}} \longrightarrow f_{\mathrm{QCM}}^{\mathrm{1st\ h}} = 2f_{\mathrm{QCM}}$. In addition to the already known phase couplings (namely $f_{\mathrm{QCM}} + f_{\mathrm{QCM}}^{\mathrm{1st\ h}} \longrightarrow f_{\mathrm{QCM}}^{\mathrm{2nd\ h}}$ and $f_{\mathrm{QCM}} + f_{\mathrm{QCM}}^{\mathrm{2nd\ h}} \longrightarrow f_{\mathrm{QCM}}^{\mathrm{3rd\ h}}$ in addition to the one mentioned above), a coupling from the first harmonic to the third $f_{\mathrm{QCM}}^{\mathrm{1st\ h}} + f_{\mathrm{QCM}}^{\mathrm{1st\ h}} \longrightarrow f_{\mathrm{QCM}}^{\mathrm{3rd\ h}} = 2f_{\mathrm{QCM}}^{\mathrm{1st\ h}}$ emerges. As mentioned above, combinations between low-frequency components still exist in this spectrum, in fact with a b^2 gain compared to the single auto-bicoherence spectrum similar to that of the QCM. This points out the importance of concentrating one's attention to the scales where the local fluctuations are strongest and where the wave-wave interactions actually take place within the turbulence.

In the case of the L-mode spectra a similar improvement is found. The maximum squared bicoherence grows by a factor of 5 for the picked EDD velocity. In the IDD-EDD cross-bispectrum a previously unknown set of wave-interactions are observed between low frequency IDD fluctuations at approximately 30 kHz and the entire range forward from the frequency of the break in slope, albeit at a very low level of phase coherency. This might be an indication of the IDD fluctuations involvement in the forward transfer dynamics. The fact that the bicoherence level is small, and indeed in some plasmas missing entirely, could be a reason why there is little mention of interactions of this sort in the literature. While a more thorough investigation of this phenomenon is outside the scope of this thesis, we stress that this shows a statistically significant non-linear coupling between the IDD and EDD propagating turbulence in this Ohmic L-mode plasma.

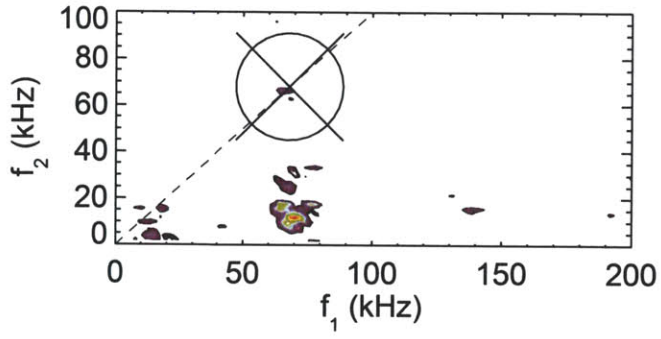

Figure 4-27: A slice through the 2D wavenumber-frequency bicoherence spectrum of the EDA H-mode studied in the previous subsection with fixed phase velocities for the two contributing components. The phase velocities are the QCM phase velocity for f_1, and the linear fit to the IDD feature below 100 kHz for f_2. The feature that is crossed out is due to an obvious aliasing effect at the QCM frequency (finite size). Maximum squared bicoherence: $b^2_{\max} = 3.3\%$

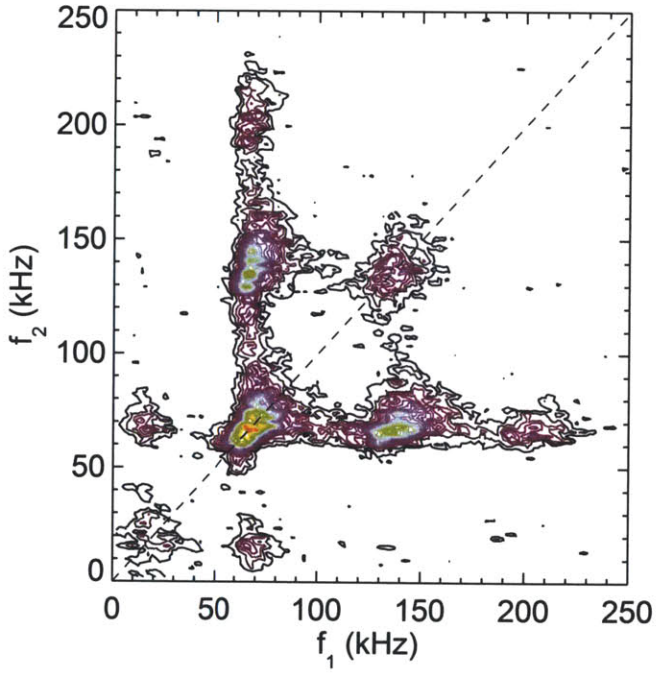

Figure 4-28: Auto-bispectrum of the slice at the QCM phase velocity of the same signal as in Fig. 4-27. Maximum squared bicoherence: $b^2_{\max} = 25\%$; squared bicoherence at the maximum of Fig. 4-27: $b^2_{\text{low}} = 6\%$.

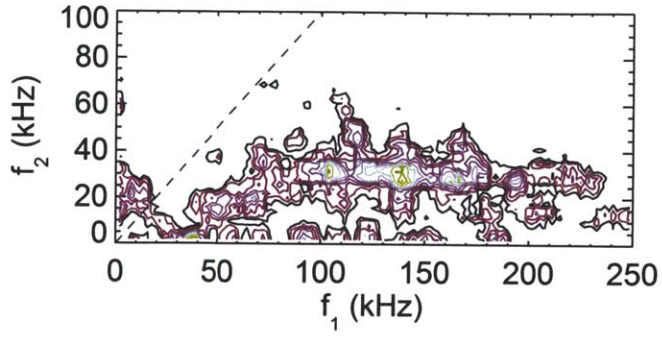

Figure 4-29: Bicoherence between the IDD and EDD features of the higher density L-mode of Fig. 4-25, with the same axes as Fig. 4-27 adjusted for the phase velocities of the wavenumber maxima on both sides of a conditional spectrum. The maximum bicoherence is barely statistically significant at $b^2_{\max} = 1\%$.

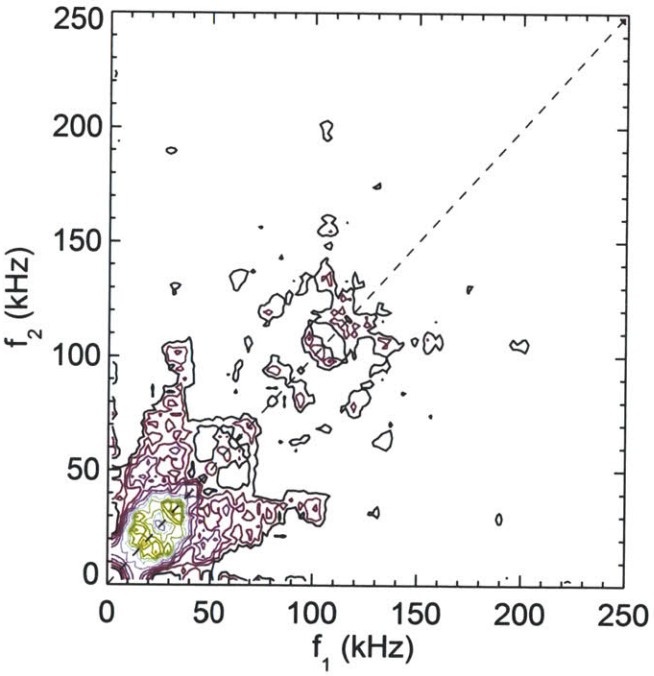

Figure 4-30: Auto-bispectrum of the slice at the EDD feature's phase velocity of the same signal as in Fig. 4-29. Maximum squared bicoherence: $b^2_{\max} = 5\%$.

4.7.3 Spectral Transfer

The results of the previous section serve one purpose very well: they give constructive evidence of the presence of quadratic nonlinearities in both the developed L-mode

EDD propagating edge turbulence and the EDA H-mode. In the former, the finite component of the bispectrum are concentrated below the break-in-slope frequency. In a specific shot the QCM, the characteristic edge fluctuation of the latter regime has been shown to possess a strongly nonlinear structure with multiple higher harmonics, as well as interactions with the broadband fluctuations. Since our main focus is the broadband turbulence and *its* relationship to the QCM, the dependencies of the nonlinear shape of the QCM are left to Appendix A.

There are two aspects however, in which a pure bicoherence or bispectrum analysis cannot deliver. The auto-bispectrum is sensitive to the existence of nonlinearity in a time series, it is indifferent whether this nonlinearity was accumulated in the past history of the signal (in turbulence this would be a spatial region of strong interactions and observed features advected into the sight of the instrument), or if it is active at the time and place of the observation. This in turn means that regardless of the biphase information, it is impossible to tell what the direction of the fluctuation power transfer is. This is a crucial measurement for deciding whether fluctuation power is being pumped into the turbulence at the break-in-slope or the QCM scale and hence transferred to both smaller and larger scales.

To access this information, the spectra exhibiting nonlinearity have to be measured in two separate locations (for $\langle . \rangle$ representing time averaging) or at two time (ensemble average). A method introduced by Ritz [106, 107], later refined by Kim [108] and recently even adapted to multiple-field turbulence [100] uses a simple network approach with a nonlinear transmission and can be applied in a wide range of situations. First the wavenumber and/or frequency spectra of the fluctuation quantity are taken at two different times $X(f)$ and $Y(f)$ and the later (or post-transfer) one is expressed as

$$Y(f) = L(f)X(f) + \sum_{f_1 \geq f_2} Q(f_1, f_2)X(f_1)X(f_2) + \epsilon, \tag{4.12}$$

which is just the Fourier transform of the Volterra expansion of the fluctuating quantity, used to model the output of a nonlinear system which depends on the input to

the system at all previous times, such as expected in a turbulent signal. The linear term $L(f)$ contains information about the dispersion and the linear growth rate. The primary way in which this model is more sophisticated than a simple bispectrum is the appearance of the *quadratic coupling coefficients* $Q(f_1, f_2)$. The expansion stops at the quadratic order; a choice justified in the present situation because four-wave interactions described by the cubic term are small. Indeed, in the analysis, the fourth order moments $\langle X(f_1)X(f_2)\overline{X(f_3)X(f_4)}\rangle$ have to be calculated and were therefore be shown to have an amplitude never more than 1% of that of the bispectrum. The term ϵ is therefore dropped. In order to determine the quadratic coupling coefficients, Eq. 4.12 must be solved for $L(f)$ and $Q(f_1, f_2)$ using the measured spectra. This is carried out by generating two moment equations from Eq. 4.12 by multiplying with $\overline{X(f)}$ and $\overline{X(f_1)X(f_2)}$ respectively

$$\langle Y(f)\overline{X(f)}\rangle = L(f)\langle X(f)\overline{X(f)}\rangle + \sum_{\substack{f_1 \geq f_2 \\ f=f_1+f_2}} Q(f_1, f_2)\langle X(f_1)X(f_2)\overline{X(f)}\rangle \tag{4.13}$$

$$\langle Y(f)\overline{X(f_1)X(f_2)}\rangle = L(f)\langle X(f)\overline{X(f_1)X(f_2)}\rangle + \sum_{\substack{f_1' \geq f_2' \\ f=f_1'+f_2'}} Q(f_1', f_2')\langle X(f_1')X(f_2')\overline{X(f_1)X(f_2)}\rangle \tag{4.14}$$

Where the matching condition was applied to restrict wave-wave interactions in order to satisfy the physical conservation laws. If we now use the density fluctuation spectrum (since that is the one to which the diagnostic is primarily sensitive in the parameter ranges under discussion) such that $X(f) = n(f,t)$ and $Y(f) = n(f, t+\tau)$, and recognizing that the power spectrum is $P(f) = \langle X(f)\overline{X(f)}\rangle$, we can write down the simplest form of a wave-kinetic equation for all scales f as

$$\partial_t P(f) \approx \gamma(f)P(f) + \sum_{\substack{f_1' \geq f_2' \\ f=f_1'+f_2'}} T(f_1, f_2), \tag{4.15}$$

where $T(f_1, f_2)$ is the quadratic power transfer, representing three-wave transfer between components $f \leftarrow f_1, f_2$, and

$$T(f) = \sum_{\substack{f_1' \geq f_2' \\ f = f_1' + f_2'}} T(f_1, f_2)$$

the power transfer *function* quantifying *total power gained (positive) or lost (negative)* by the scale f due to three-wave interactions, and is therefore the object of our primary interest. It can be found by expressing $P(f)$ with $X(f)$ and discretizing the time derivative

$$\begin{aligned} \partial_t P(f) = \partial_t (X(f,t)\overline{X(f,t)}) = \overline{X}\partial_t X + X\partial_t \overline{X} = 2\mathrm{Re}[\overline{X}\partial_t X] \\ \approx 2\mathrm{Re}\left\{\overline{X}\frac{X(f,t+\tau) - X(f,t)}{\tau}\right\} = \frac{2}{\tau}\mathrm{Re}(Y\overline{X} - X\overline{X}) \end{aligned} \quad (4.16)$$

which is the first moment equation with the identifications $\gamma(f) = 2\mathrm{Re}(L(f) - 1)/\tau$ and

$$T(f) = \sum_{\substack{f_1 \geq f_2 \\ f = f_1 + f_2}} Q(f_1, f_2)\langle X(f_1)X(f_2)\overline{X(f)}\rangle.$$

In the Kim method ideal (fully described by the quadratic transfer equation) and non-ideal fluctuations are separated. Here this separation is omitted and all fluctuations are considered as ideal. The validity of this can be checked a posteriori by noting whether power stationarity is satisfied with the variables calculated without imposing it such as in the assumptions of the Kim method. With this simplification the set of moment equations can be solved as a matrix equation, which saves significant computation costs. In this matrix form $\mathbf{A}$ and $\mathbf{B}$ are the vectors of the third-order moments (auto and cross-bispectra respectively), F is the matrix of the fourth-order moments (for details see Appendix C), and the set is solved by

$$L(f) = \frac{\langle Y(f)\overline{X(f)}\rangle - \mathbf{B}^* \cdot \mathrm{F}^{-1} \cdot \mathbf{A}}{\langle X(f)\overline{X(f)}\rangle - \mathbf{A}^* \cdot \mathrm{F}^{-1} \cdot \mathbf{A}} \quad (4.17)$$

$$Q(f_1, f_2) = (\mathbf{B}^* - L(f)\mathbf{A}^*) \cdot \mathrm{F}^{-1}, \quad (4.18)$$

where the asterisk means the adjoint operation (complex conjugation and transposition). The above solution makes no assumptions about the functional form of the coupling coefficients as does [109], it is however restricted compared to the analysis presented there for multiple fields by the fact that only n_e fluctuations are accessible in our case.

Since the time-resolution of the system is far better than its spatial resolution, and further because the viewing spots cannot be moved around to sample different areas, we wish to use frequency spectra in the analysis and substitute the discrete time variable τ by $\tau = \Delta z / v_E$, where Δz is the spatial separation between two measurements and v_E the bulk plasma velocity (which can be taken from e.g. CXRS measurements [6], and for the analysis assumed to be known).

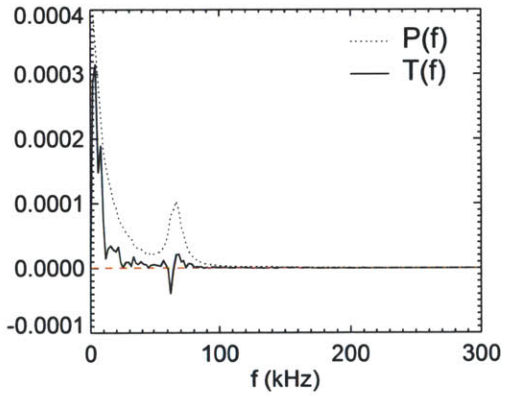

Figure 4-31: The power transfer function $T(f)$ calculated from paired individual signals for the same EDA H-mode as before; the flux-surface average power spectrum is overlaid for illustration of the scales involved. Negative $T(f)$ at the QCM frequencies and positive values through the broad-band turbulence are found.

Figure 4-31 displays the result of our calculation in the EDA H-mode of the previous sections, for $X(f)$ and $Y(f)$ individual signals, where $Y(f)$ is downstream from $X(f)$. To obtain the transfer function in the figure, pairs of signals with a fixed separation along the magnetic flux surface were chosen and the functions averaged for the flux surface. These first results show promising characteristics. At the frequency of the QCM, $T(f)$ is negative. This means that on average the QCM loses energy to other frequencies through quadratic coupling. Interestingly, it seems that some of this

energy is gained by the higher frequency part in the somewhat broadened peak of the QCM. The sum under the curve covering the entire mode, however is still negative. This implies that this scale feeds the rest of the spectrum.

To follow the course of the analysis from the previous section, we then turned to utilize the wavenumber information by using the same "velocity" selected spectrum as the one which provided the highly enhanced bicoherences. In order to have two measurement locations, the spectra are generated from 5 adjacent channels of the vertical viewing array. Figure 4-32 demonstrates how the values for the transfer function are enhanced in the analysis. The structure of the transfer processes remains qualitatively the same. In addition to the finding in the single view pair analysis, significant values are now found at the first harmonic frequency. The structure of $T(f)$ at this frequency is somewhat similar to the behavior at the QCM fundamental, yet, importantly, the sum under the curve at *this* component is positive, indicating that the harmonic gains energy from the interactions. The small negative value affirms the reliability of the calculation, since the second harmonic is expected to feed from the first and the QCM fundamental.

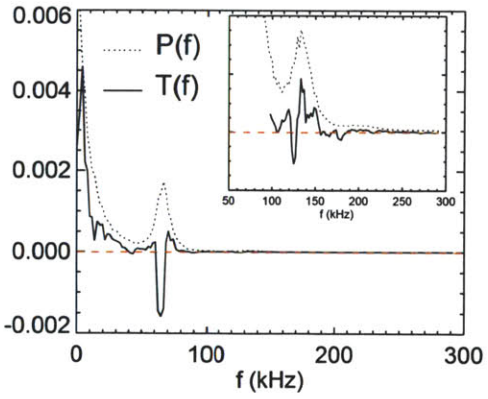

Figure 4-32: The power transfer function $T(f)$ calculated from propagation velocity filtered signals in the sense of the previous section for the same EDA H-mode as above. Features are enhanced compared to Fig. 4-31. The inset is a zoom into the first harmonic frequency range.

Finally, the same analysis is applied to the L-mode spectrum well described phenomenologically by two power-law sections with a break in slope around $f = 100$ kHz

and $k_\theta \rho_s \simeq 0.1$. The single view pair analysis is inconclusive, showing no significant values in the transfer function (or too much noise). Seeing that the bicoherences are far weaker in this case than with a QCM, and that the $L(f)$ and $Q(f_1, f_2)$ coefficients sensitively depend on them, this is not far from expectations. The second type of analysis finally shows the results summarized in Figure 4-33. The frequency range $85 < f < 105$ exhibits a set of small negative values, and the broadband low frequency part is on average positive. Following the same logic as above, we find that the turbulence does indeed seem to be driven at the break in slope scale in the spectrum.

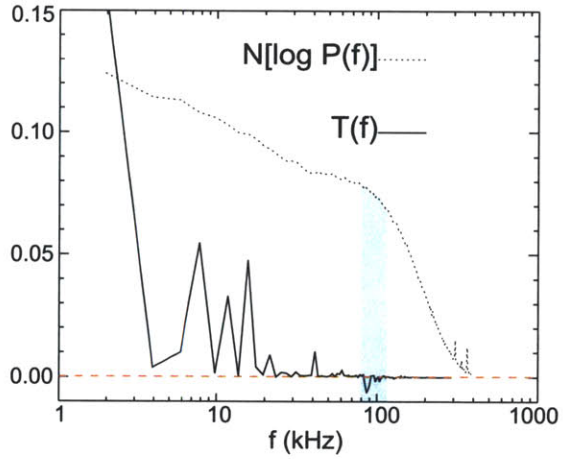

Figure 4-33: The power transfer function $T(f)$ calculated from prop. velocity filtered signals in the sense of the previous section for the Ohmic L-mode plasma analyzed in the section before. The power spectrum is overlaid on a log-log scale (shifted and rescaled in P, though not in frequency) for illustrative purposes. The only significant negative values are found in the shaded area.

The chapter on the GPI measurements and the physical results found through their analysis concludes with this significant result. The findings of this chapter are discussed and compared to some expectations found in the literature in the next chapter.

Chapter 5

Edge Turbulence Scalings and Discussion

5.1 Density vs Pressure Scaling

The scaling of the edge turbulence power with the Greenwald-fraction $F_{Gr} = \bar{n}_e/n_G$ was particularly useful in Chapter 4. It helped connect the rapid magnitude growth of the turbulence in the edge region propagating in the EDD direction to the increase in the (normalized) line-average density, and thus connect the measured turbulence to observed and important cross-field transport processes. In addition, it implies a connection between the turbulence and the density limit itself. Nevertheless the line average density is a macroscopic, "engineering" type of parameter, which does not therefore help one to connect the experimental results to microscopic processes from which a theory could be derived, e.g. what physics might be important in developing the observed turbulence. In search of another parameter, which could better serve that purpose, the results were expanded by measurements done in later campaigns (2009-2010), and then plotted against β_p, the plasma pressure normalized to the pressure of the poloidal magnetic field, measured at the top of the steep gradient, where the EDD turbulence is strongest. Figure 5-1 shows that the parameter seems to organize the data better, in other words, it appears to be a more sensitive figure of merit, over the range of experimental conditions and where exponential (or even

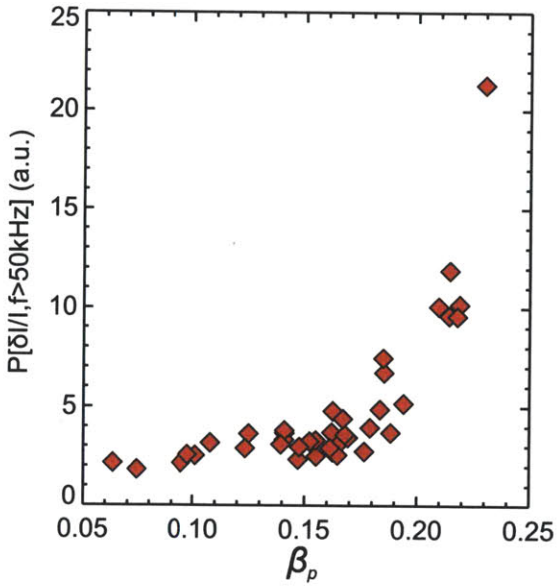

Figure 5-1: Sum of the fluctuation power relative to the DC level above 50 kHz from the EDD turbulence plotted against the pressure normalized to the pressure of the poloidal field β_p.

faster than exponential) growth is seen in the turbulence power.

Theoretically, in the modern edge codes (for example DALF3 [39] and GEM3 [110]) the key physical parameter for kinetic shear Alfvén effects is $\hat{\beta} = \beta_p(a/L_n)^2$, a quantity very similar to our poloidal beta. Further support is given by the results from [5], which show that L_n is quite stiff in the range of densities involved in the investigation both in [5] and this thesis. In addition, in electromagnetic simulations a finite β_p was found to enhance nonlinear interchange-drift effects [111].

5.2 Characteristic Size Scale

The characteristic size scale $k_\theta \rho_s \approx 0.1$ found to be quite robust for the edge fluctuations both through the changes of Ohmic L-mode operations, where the edge transport and the spectral distribution of the turbulence underwent significant changes, and even in the EDA H-mode, where this scale matched the well defined wavenumber of the quasi-coherent mode is of further interest. Even though historically edge plasmas demonstrated the importance of the scales $k_\perp \rho_s \lesssim 0.15$ (as was discussed in

Chapter 2), we have seen that various theories involving drift-like edge turbulence, starting from the earliest H-M and W-H models, favor the scale $k_\perp \rho_s = 1$.

Even though we found important indications that the break in slope in the spectra is the result of an underlying instability, in search for a physical theory which could predict a breaking point in the spectra at the required scale, two-nonlinearity models [102, 101] were tested. Even though these models do not predict a spectral index in either of the ranges in which one is measurable in C-Mod GPI measurements, they do introduce a scale, (more or less the same in both models)

$$\delta = \frac{c_s}{L_n \nu_e}$$

at which the $\mathbf{E} \times \mathbf{B}$ nonlinearity is on the same order as is the polarization nonlinearity, where the spectra in $k_\theta \rho_s$ are predicted to show a sudden drop-off. For the cases of C-Mod L-modes, $\delta \approx 10 - 20$ depending on the discharge. This means that the scale at which the drop off in this model should occur is approximately 100 times higher than experimentally observed. What this comparison positively tells us is that since $k_\theta \rho_s \ll \delta$ for the entire spectrum, the $\mathbf{E} \times \mathbf{B}$ nonlinearity is important. It has to be emphasized though that this theory [102] does *not* predict spectral transfer away from this particular scale, and hence does not provide a complete description of the turbulence dynamics.

Indeed the same can be learned from far more advanced codes, such as the already cited [39]. In addition, this code does provide complete spectra for both density (pressure) and potential fields. In the range of poloidal betas of interest, the predictions are quite widely distributed as is evidenced by [112], falling in the range $3 < \beta < 5$ for the fast dropping part of the spectrum, and thus do not reproduce the fairly robust short wavelength spectral index found in Chapter 4. Perhaps more important is the fact that even in this fairly advanced code the "breaks in slope" occur in the range $0.5 < k_\perp \rho_s \leq 1.2$, still significantly different from the observed results. One particularly interesting feature of the code outputs is the fact that at the parameter values best matching those of C-Mod, $k\rho_s \approx 0.1$ *is* an important scale. It is the scale at

which in the competition between the drift wave and the interchange/ballooning dynamics, the latter becomes important. This theoretical prediction appears to support the connection between the L-mode broadband turbulence and the quasi-coherent mode (a mode which has been identified as a resistive ballooning mode) found in this thesis.

A further deficiency in the theories predicting spectra and spectral transfer processes for the edge turbulence is the apparent lack of output spectra which could in fact predict a low density L-mode spectrum in which at the critical wavenumber of $k_\theta^c \rho_s \approx 0.1$ a peak is found in the spectrum. Such spectra *do* appear in the cited modern codes, but without exception they appear only as transient states. Thus we find from these examinations of the present state of edge turbulence theory/modeling that modeling does not reproduce the quantitative features of the experimental observations, although some qualitative features are intriguing.

5.3 Forward vs Inverse Transfer: Criticism of the Bispectral Techniques Used, GAMs

Even though the analysis presented at the end of Chapter 4 concluded with results above the noise level, there is a point of concern, which is the reason why the absolute magnitude of the spectral transfer in these measurements was not reported, and further, the reason the strength of the forward and inverse cascade directions should not be compared. As the previous section clearly pointed it out, the turbulence in the edge and SOL region of Alcator C-Mod exists in a parameter range where the $\mathbf{E} \times \mathbf{B}$ nonlinearity is important. As a consequence of that, a single field approach, such as the H-M equation (Eq. (2.8), which is completely analogous to the three-wave coupling analysis formula, Eq. 4.12, used in this work) does not adequately describe all the transfer processes in the turbulence.

Indeed, a two-field model, such as the Wakatani-Hasegawa equation (Eq. (2.9)), can be seen to include terms of the form

$$\langle n_{\mathbf{k}_1} \phi_{\mathbf{k}_2} \overline{n_{\mathbf{k}}} \rangle$$

and

$$\langle \phi_{\mathbf{k}_1} \phi_{\mathbf{k}_2} \overline{\phi_{\mathbf{k}}} \rangle$$

upon Fourier transformation. In other words, there are no terms involving only density field (as is the case in our analysis). One case, in which the single density field analysis would still provide completely consistent values (and not merely an indication of a total transfer direction, such as in our case) would be an $i\delta$ model. Unfortunately, as the previous section pointed it out once more, theory suggests that in the edge turbulence we observe, interchange effects are important, and these are known to strongly violate $|\tilde{n}| = |\tilde{\phi}|$.

Recent analysis by Manz of a Wakatani-Hasegawa turbulence simulation and experimental results using both the single field model and a complete two-field analysis [113, 100] showed that the two nonlinearities transfer fluctuation power in opposite directions. Moreover, it was shown in these papers that using only the density field will be representative of the *forward transfer* directions, but will greatly distort results in the inverse transfer direction, where the vorticity nonlinearity is dominant.

Since direct electric potential measurements are normally not available at the depth inside the LCFS where the most interesting spectral features are observed, one possibility of improving the accuracy of the analysis would be to use the velocity-fluctuation field as the second turbulence field, as was done by Holland [114], in the first true two-field analysis performed solely via optical measurements. Holland showed that geodesic-acoustic modes [115] (GAM, see Appendix A) transfer energy forward in the turbulence. In an attempt to reproduce Holland's two-field analysis using C-Mod GPI data, a two-field analysis toolkit was written and applied. No GAM oscillation in any of the confinement regimes used in the main analysis of Chapter 4 was apparent using this approach. However, as will be shown in Appendix A, strong evidence for GAMs in C-Mod is found in the GPI data from the more "exotic" I-mode discharges using bispectral analysis techniques.

5.4 Characteristic Edge Fluctuations of Confinement Regimes

There is a further point to be considered in order to support the importance of the edge region and in particular, the EDD propagating fluctuations therein. One outstanding result from the past few years of GPI experiments on Alcator C-Mod is that each of the attainable confinement regimes has a unique and *qualitatively* different pattern of fluctuations just inside the LCFS. Here we will make a list of these confinement regimes C-Mod and their characteristic edge-turbulence patterns in the wavenumber-frequency range, distribution signatures, etc. This can also serve as a thumbnail gallery for use in identifying confinement regimes on Alcator C-Mod.

5.4.1 L-Mode

Since all the previous chapters of this thesis are devoted to the detailed analysis of the edge- and some of the SOL-turbulence in Ohmic L-mode plasmas, here we only refer the reader to Fig. 5-5 where a typical L-mode of fairly high normalized density ($n/n_G = 0.4$) is compared to all other regimes in terms of *edge* turbulence dispersion and power spectrum. Note that a high enough Greenwald fraction guarantees a well-developed lobe in the EDD direction, reaching almost all the way to ($k = 0, f = 0$), as discussed in Chapter 4. The spectrum below was recorded at the most typical resolution of $df = 2$ kHz.

5.4.2 EDA H-mode

Once again, the EDA H-mode regime has been studied in detail in previous chapters, and some additional features of the QCM are discussed in Appendix A, where it is compared to the WCM of the I-mode regime. Here we show the experimental dispersion of the EDA edge fluctuations in order to contrast them with those of the other regimes in Fig. 5-5. In addition, we draw attention to an important and robustly reproducible feature of the QCM, namely its characteristic onset [21]. The

time evolution of the mode frequency spectrum is shown in Fig. 5-2. The mode typically appears with a frequency of 200250 kHz following the transition from the L-mode to the EDA H-mode as described in Sec. 4.5.4. It then sweeps down in frequency to a steady-state value of 50120 kHz. The time scale for this frequency evolution is $\sim 30 - 60$ ms, comparable to the momentum confinement time [116].

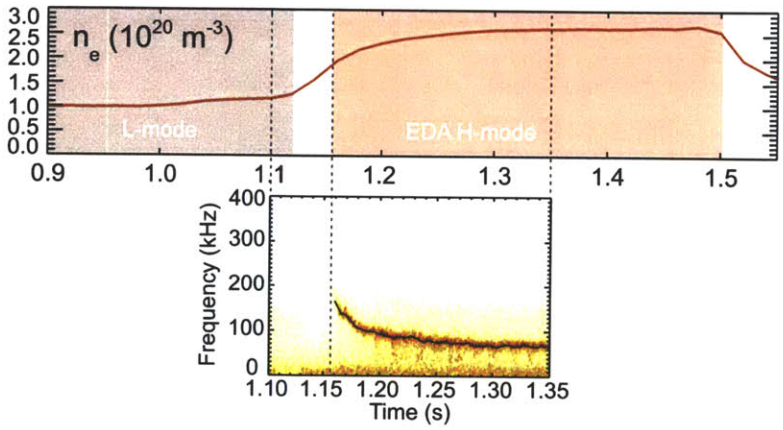

Figure 5-2: Time history of a typical EDA H-mode regime with a heating power of $P = 2.5$ MW. Top: line averaged electron density; bottom: spectrogram of density fluctuations at $k_\theta^{\mathrm{QCM}} = 2\ \mathrm{cm}^{-1}$, $\rho = -1.1$ cm. The QCM appears with $f^{\mathrm{QCM}} = 190$ kHz at $t = 1.158$ s, which marks the onset of the EDA H-mode, and it subsequently spins down to $f^{\mathrm{QCM}} = 70$ kHz with a time constant $\tau_{\mathrm{fit}} = 30 \pm 10$ ms. The black line corresponds to the centroid of the peak in frequency where applicable.

5.4.3 ELM-free H-Mode

The strong particle transport barrier in the edge of ELM-free H-modes has long been associated with the sharp suppression of L-mode density and magnetic fluctuations at the onset of ELM-free H-modes. As GPI measurements revealed, this is predominantly due to the reduction of EDD direction propagating turbulence in the region we termed the *edge*. The two spectrograms in the figure demonstrate the vast difference between the response of the turbulence in the two distinct propagation directions.

As both the spectra in Chapters 4 and 5.2 and the one from the sample ELM-free H-mode below testify, there is typically a clear IDD propagating feature in the edge signals. The IDD lobe in the conditional spectrum is mostly very sharp, indicating

that the poloidal propagation speed of these fluctuations is very well defined with $\Delta v/v < 0.05$. This speed however shows great variation from one ELM-free H-mode to the next, ranging anywhere between $v_\theta = 0.7$ km/s and 6 km/s. Establishing any scalings of this speed remains to future studies, as does the identification of these modes.

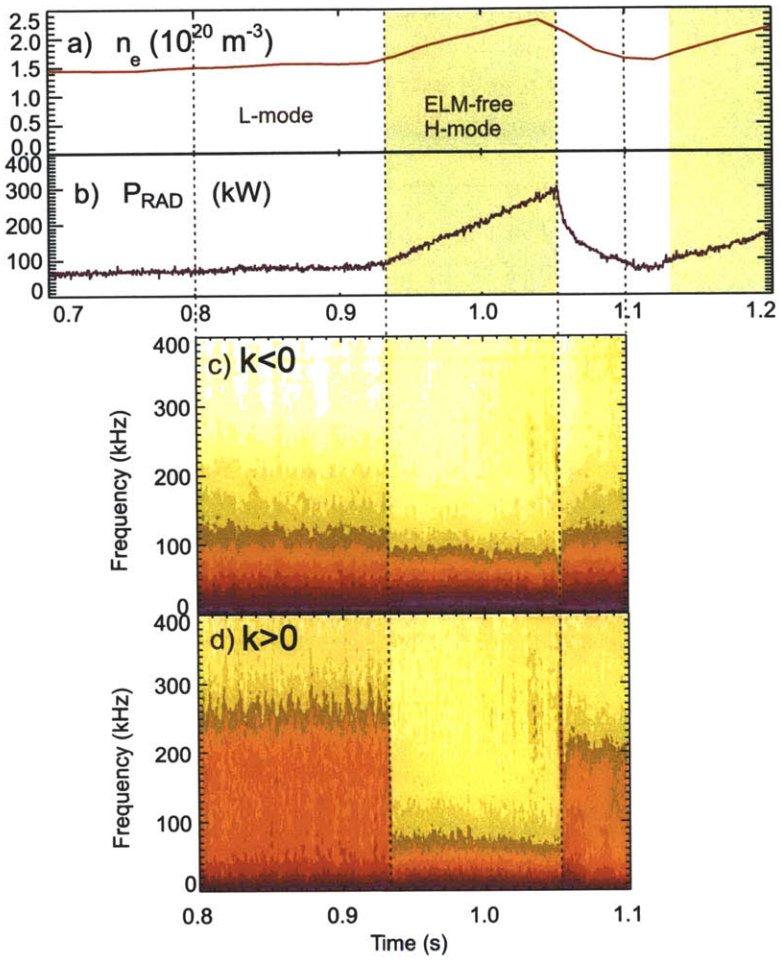

Figure 5-3: Characteristics of a typical ELM-free H-mode regime with a total heating power of up to $P = 0.9$ MW; a) line averaged electron density, b) radiated power; spectrograms of density fluctuations integrated for c) $k_\theta < 0$ cm^{-1}, and d) $k_\theta > 0$ cm^{-1} at a distance $\rho = -1.1$ cm from the LCFS.

Considering the sharply defined velocity, and the fact that in shots with a large gas-puff contrast (He puff in D plasmas) and considerable RF power the lobe does not show up in views outside of $\rho \approx -0.3$ cm, the spatial localization appears to

be correct and not a result of brighter emission from larger radii. This, however, presents a further puzzle, since this localization places these features at about the radial position of the narrow E_r well, which has been reported [6] to be the "deepest" (most negative) in ELM-free H-modes, reaching values of $E_r = -100$ kV/m. Indeed, the low power feature close to $k = 0$ at high frequencies in Fig. 5-5(ELM-free) matches the $\mathbf{E} \times \mathbf{B}$ velocity such a field would cause at $v_\theta \approx 25$ km/s. There are, however, at least to my knowledge, no modes predicted to move at a speed higher than that (far above the diamagnetic velocity) in the IDD direction in the plasma frame, even though such is required of any modes to fit the experimental dispersion provided below.

A systematic study of both the fast, low-power, EDD feature and the strong, well defined IDD feature would consequently be desirable in order to understand what we are recording in these plasmas and would contribute significantly to the understanding of the crucial differences between ELM-free and EDA or ELMy H-modes, as well as L-modes.

5.4.4 I-mode

Although at the beginning of the C-Mod studies of I-modes it was believed that it evolves smoothly from L-mode plasmas after the application of ICRF heating, our new measurements show that the typical I-mode edge fluctuation spectrograms exhibit a sudden ($< 100\mu$s, or 1 frame in a fast spectrogram) onset of the WCM at a time that is often significantly later (by at least one sawtooth period) than the time at which the ICRF turns on (Fig. 5-4). One or two short "dithers" of the WCM, such as the one at 1.12 s$-$1.13 s in the figure, are typical before the WCM becomes steady in the edge region. The growth of the stored energy W_{plasma} often ($\sim$ 75% of GPI-diagnosed I-modes) breaks in slope at the time the WCM appears. This is one reason why the specific transport qualities of this regime can be (and indeed have been) attributed to this range of fluctuations, or perhaps to the suppression of lower frequency turbulence [117].

To the untrained eye, the differences between the empirical dispersions of I-mode

and EDA H-mode plasma edges in Fig. 5-5 may seem elusive, so we devote Appendix A to the detailed comparison of these apparently beneficial edge fluctuations.

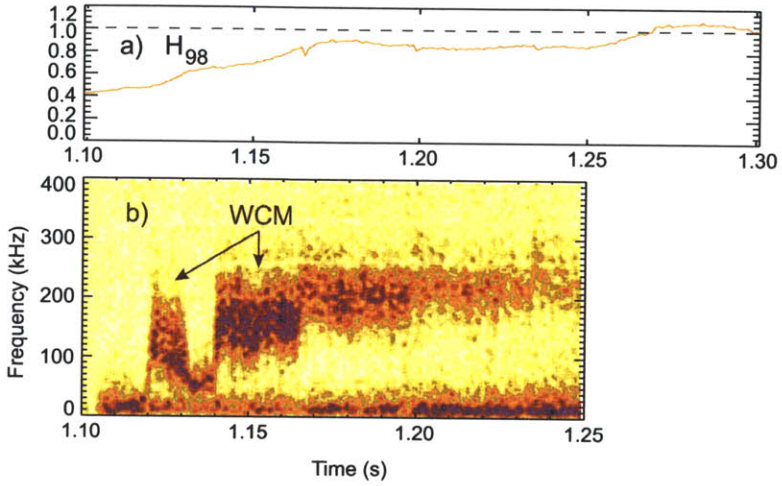

Figure 5-4: Characteristics of a typical I-mode regime with a heating power of $P = 4.3$ MW; a) H_{98} confinement factor [4] and b) spectrogram of density fluctuations at $k_\theta^{\mathrm{WCM}} = 1.8$ cm^{-1}, $\rho = -0.8$ cm.

5.4.5 ELMy H-mode

Due to the limited spatial range and gas-puff contrast provided by the previous GPI system, the local poloidal mode structure of the ELM precursors could only be inferred from the assumption that the modes, much like the ejected filaments, are aligned with the magnetic field. The new diagnostic has constructively verified that the poloidal wavenumber of the precursor oscillation is consistent with this assumption. The particular shot exemplifying a pre-crash ELMy H-mode plasma in Fig. 5-5 has a poloidal wavenumber of $k_\theta \approx 0.6$ cm^{-1}. This large wavelength is barely measurable with the ~ 4.4 cm vertical extent of the viewing array, hence the satellite lobes on both sides of the peak in the graph, the displacement of which from a completely symmetric distribution is a good indication of the truly nonzero value of the wavenumber of the central peak. The bands at higher frequency are due to the length of the spectrogram bin, as the mode is observed to slow down in the last $\sim 50\mu$s before the crash to approximately half its frequency.

Due to the rapid variation of the period, a more thorough study of these features in the future should apply a wavelet transform instead of regular Fourier-techniques to this problem. In addition, the full 2D extent of the new GPI viewing array now enables us to study the kinematics of filament detachment in the crash event, which can be an important piece in the analysis of the peeling nature of the instability.

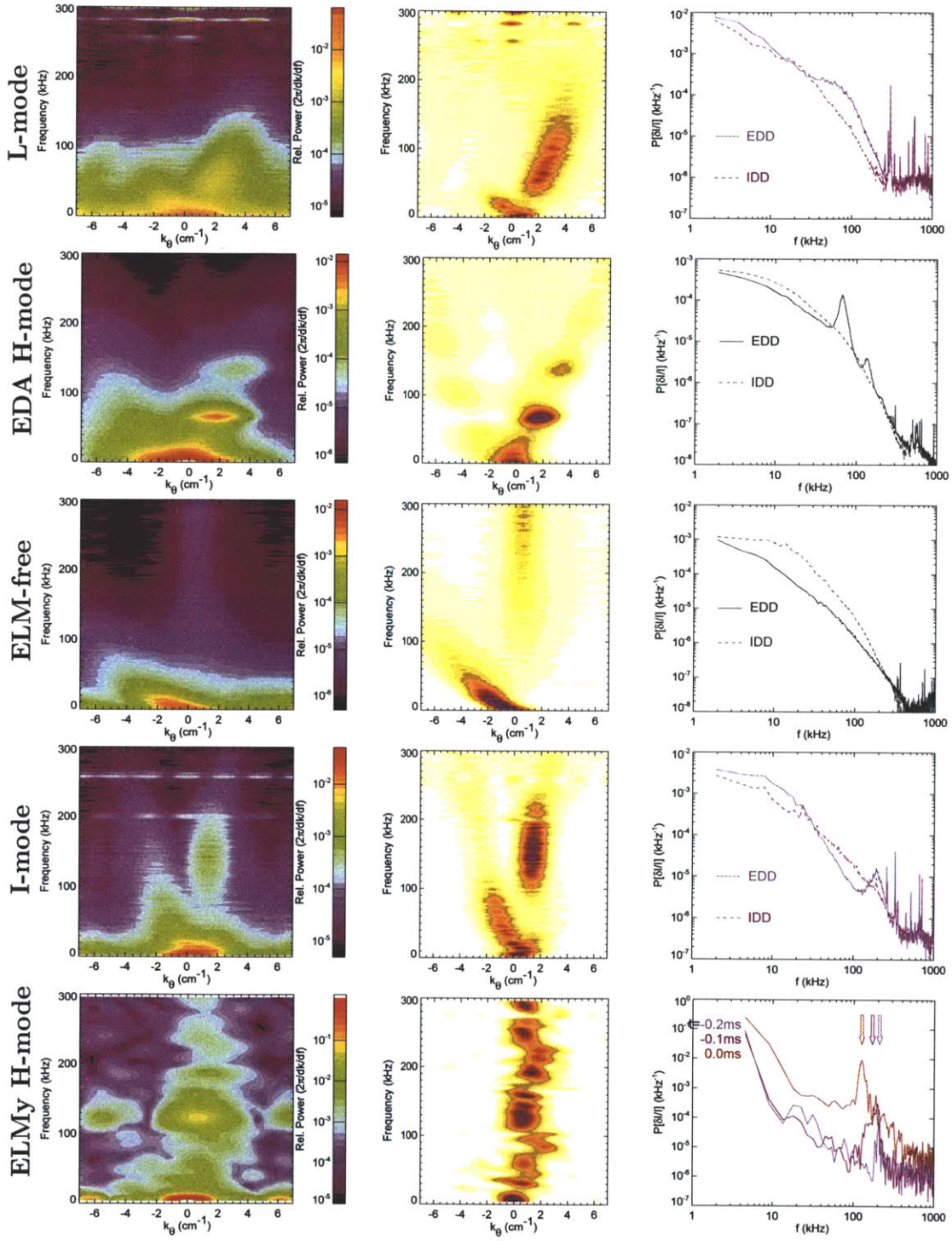

Figure 5-5: Characteristic spectra of edge fluctuations for all confinement regimes. Left: wavenumber and frequency autopower spectra $S(k_\theta, f)$; middle: conditional spectra $S(k_\theta|f)$; right: total power for $k_\theta < 0$ cm^{-1} and $k_\theta > 0$ cm^{-1}.

Chapter 6

Summary and Future Directions

6.1 Results

The primary goal of this thesis was to investigate the dependence of turbulence characteristics on macroscopic plasma parameters. Specifically, this work focused on the edge and Scrape-Off-Layer regions of the outboard midplane of Alcator C-Mod, where fluctuations of plasma density are the strongest due to turbulence. In order to provide new information which can be used for testing physically comprehensive theories of edge plasma turbulence in tokamaks, that is theories which would explain the source of edge turbulence, the distribution of fluctuation energy to all scales at which turbulence exists and finally the transport phenomena caused by these structures, this study collected data about each of the above.

To accomplish this experimentally, the study required a new fast, sensitive, low noise detector system for the gas-puff-imaging diagnostic, capable of covering the entire physical range in which transport phenomena go from a more diffusion-like process to a clearly singular-feature dominated one. An avalanche-photodiode-system was designed and built, which outperforms all previous GPI diagnostics on C-Mod and most other current tokamaks. The new system features 90 channels in a 9×10 array of views with a 3.8 mm spot size for a single view, providing a poloidal wavenumber range $0.4\ \text{cm}^{-1} < |k_\theta| < 7\ \text{cm}^{-1}$. The APDs are sampled at 2 MHz, and with the sensitivity of the detectors and the typical light levels of the observed space, the signals

commonly become photon noise dominated at above 500 kHz. In this frequency range, the system regularly covers up to 6 orders of magnitude in spectral power of the observed turbulence. The gas puff imaging can be used in D_2 or ^4He mode in order to maximize contrast.

A specific physical region was identified as especially important for turbulence and transport processes. The fully two-dimensional nature of the diagnostic enabled us to acquire radial profiles of a number of relevant quantities; the significance of the the closed flux surface edge region is emphasized by the following observations. Radial profiles of the poloidal phase velocities of emission features were recorded using 2D Fourier techniques. The profiles resemble those from previous measurements done on C-Mod by Langmuir-probes and results from other machines: the SOL moves in the ion-diamagnetic drift direction at a velocity 0.5 km/s $< v_\theta <$ 3.0 km/s depending on the plasma, closely matching the $\mathbf{E} \times \mathbf{B}$ drift velocity in the far SOL, while the edge features propagate in the electron diamagnetic drift direction at a speed close to the diamagnetic drift velocity. A previously unexpected result shows that the transition between the two velocities is not smooth as probe measurements with minimal spatial resolution suggested, but rather, there are two distinct layers of turbulence with velocities that are relatively robust through the region. In the views between the regions, the two counter-propagating features flicker on a fast times scale of $\sim 100\mu$s that was shown to be the characteristic time of filament ejection into the SOL.

These filaments cause intermittent signals, and accordingly strongly skewed distributions. However, the probability distribution of the signals through both zones are found to be well fitted with one single class of distributions, so long as the linearity of the emissivity with plasma density can be ensured or restored from a detailed model. This "universality" further suggests that the source, or birth region of the blobs responsible for the vast majority of cross-field transport in the SOL is the EDD propagating edge turbulence.

The separation of the two propagation directions and radial regions enabled us to study these separate pieces of the turbulence with a wide range of plasma densities, toroidal magnetic fields and plasma currents. The separation and the scans together

revealed a trend not found before: the relative fluctuation power $\tilde{n}/n$ in the EDD edge turbulence was shown to scale sensitively with $\bar{n}_e/n_G$, the line average density normalized to the robust tokamak density limit in the range $0.15 < \bar{n}_e/n_G < 0.5$. In the same range, the SOL is found to fill in with plasma, and the directly measured cross field particle flux density just outside the LCFS also exhibits an explosive growth. These phenomena indicate the important role of the turbulence in the edge region in determining the SOL structure and the cross-field transport in general. These results, together with the observation of bright features "invading" the closed field line structures at even higher densities, suggest that the Greenwald limit is in fact transport related, rather than being a purely radiation related limit.

Having realized that separate regions and directions need to be treated separately, the spectral analysis of the EDD edge turbulence through these important changes revealed a physical scale $k_\theta \rho_s \approx 0.1$ at which the spectral index has a clear break for all Ohmic L-mode plasmas. The spectral shape below this point also depends on plasma density, filling in more and more scales as the density increases. Moreover the spectra of discharges at a low densities even exhibit a broad peak at the critical physical scale. Current edge turbulence theories do not predict such characteristics.

The turbulence phenomenology of the L-to-H transition was also investigated. Neither the $\tilde{n}/n$, nor the spectral distribution of the SOL showed any changes through the transition except for a very short quiet period ($\sim 200\mu$s), while the EDD edge turbulence dropped by about an order of magnitude through the ELM free H-mode regime, and developed the well-known quasi-coherent mode in the EDA regime, exactly at the physical scale $k_\theta^{\mathrm{QCM}} \rho_s \approx 0.1$.

Because of the above phenomenology, bispectral analysis was conducted on both L-mode and H-mode EDD fluctuation spectra, including the *first spectral transfer measurement* for turbulence at C-Mod. The spectral transfer estimation showed that the critical wavenumber region is indeed feeding energy into the rest of the turbulence. The low density, low turbulence power discharges showed a significantly reduced phase coupling structure, explaining the peaked spectra as a reduction in spectral transfer away from the critical scale. The key difference between L-mode

and H-mode spectra was the significant forward transfer in H-mode. These results suggest that the underlying instabilities of the two regimes might be the same and the primary cause of the transition should be sought for in the competition between forward and inverse transfer.

Thus the new GPI experiments have provided information on all three of: the source, the spectral transfer and the transport characteristics of typical Ohmic L-mode edge turbulence.

6.2 Future Use of Wavelet Techniques

During this research, we concentrated on the edge turbulence characteristics of the Ohmic L-mode discharges and the way they relate to the trends experienced in cross field particle transport and the coherent H-mode edge fluctuations. The tools developed in the course of this work, however, can be both put to further use and expanded. The wavelet analysis software which was used here to prove true intermittency in the SOL, and which found the most intermittent scale and the waiting time distributions, has already been expanded for fast time scale velocity detection. This will enable the 2D fast GPI system to study the blob-filament regimes and the blob-size-radial speed distributions, as well as ELM crashes in unprecedented detail.

6.3 Effects of RF heating on the SOL

While concentrating on the simple case of Ohmically heated L-mode plasmas helped us isolate the effects intrinsic to the plasma edge and its turbulence, it is clearly not the operational regime with the most potential for high confinement studies and eventually fusion applications. The effects of radio frequency heating on the edge and the SOL could not have been fit into the main discussion of this thesis. However, the broad 2D viewing area has now enabled us to study these effects which would never have been observed on the single vertical viewing array. In the case of some of the H-mode plasmas presented in Chapter 4 heating at Ion Cyclotron Range of Frequencies

(ICRF) was in use, but we took care not to discuss the regions outside the plasma edge, except in terms of total fluctuation power. On closer inspection of SOL GPI signals from these shots, it turns out that the introduction of radio-frequency (RF) waves to the SOL creates novel structures, indeed some of them are reported here for the first time.

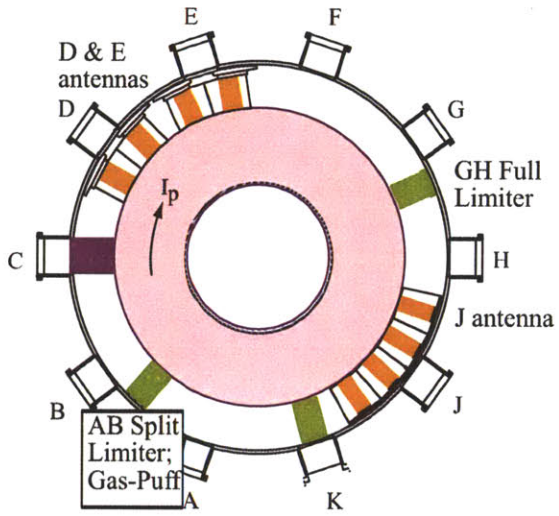

Figure 6-1: Top view of Alcator C-Mod showing the locations of the ICRF antennas D, E and J in relation to the toroidal position of the diagnostic gas-puff.

At the most common edge safety factors the region observed by the low-field-side GPI diagnostic is magnetically connected to the ICRF antennas, all of which are approximately a quarter toroidal turn away from the location of the outer gas-puff, as shown in Figure 6-1. The magnetic pitch angle of the field both at normal and reversed I_p and B_T operation is such that the field lines piercing the GPI observed poloidal slice in the middle, are connected anywhere from the middle to the bottom of the antennas at the J and D ports and the bottom of the one at E port, or just missing it.

In order to highlight the radial regions in which a certain poloidal propagation velocity is dominant, and at the same time provide a measure of a) how much overlap there is between potential counter-propagating features and b) how large the velocity spread is, we calculate a distribution in velocity space by integrating the conditional

spectrum along fixed phase velocity contours, such as the ones shown in Section 4.5,

$$D(v_\theta) = \frac{1}{N(v_\theta)} \sum_{f=0}^{v_\theta k_N/(2\pi)} S(k_\theta = 2\pi f/v_\theta | f).$$

A figure showing the above distribution for the case in Figure 4-13 can serve as a comparison and help facilitate the understanding of this method (Fig. 6-2).

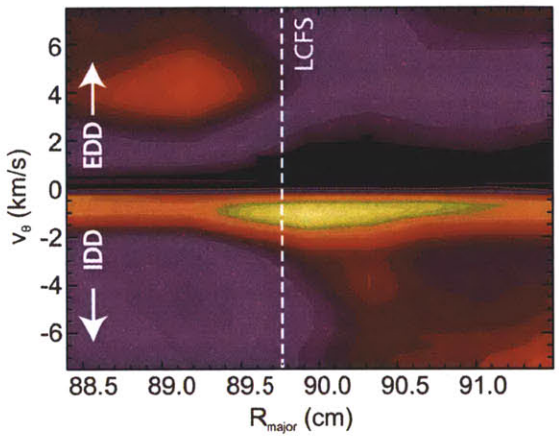

Figure 6-2: Demonstration of the velocity visualization technique described in the text. The figure shows the same results as Fig. 4-13.

A wide range of operating parameters was scanned for the tests in this appendix in an attempt to provide sufficient information for theoretical work in understanding the following observations, *which have never been reported before.* Line integrated plasma densities of 4×10^{19} m^{-2} $< nl_0 4 <$ 1.1×10^{20} m^{-2}, ICRF heating powers $P_{RF} \leq 3$ MW, from all antennas, at RF frequencies of 50 MHz, 78 MHz and 80 MHz into both USN and LSN geometries at various edge safety factors, L-mode and H-mode confinement regimes, forward and inverse plasma current and magnetic field combinations were all investigated. The figures below were obtained.

The basic observation is summarized as a side by side view of an Ohmic L-mode discharge and a strongly ICRF heated discharge of the same field strength, plasma current, density and USN geometry in Figure 6-3. By slowly ramping the heating power, it is found that at $\gtrsim 600$ kW the dominant propagation directions in the SOL change. No oscillation is observed in time, the structure is steady, but the dominant

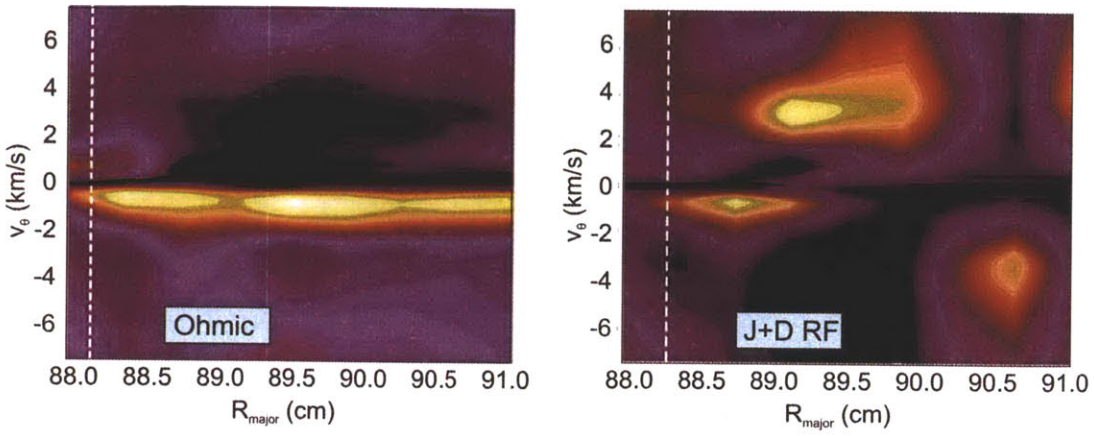

Figure 6-3: GPI measurements of the poloidal velocity profile in the SOL with a large gap between the wall and the plasma in order to clearly identify regions of interest. When the RF heating is on (right), a radially oscillating structure is observed which is steady in time.

propagation direction changes sign up to 4 times in the $\sim$ 3 cm region between the wall and the separatrix. Since it was shown both in this thesis and other works [84] that in the far SOL where blobs dominate the emission landscape, they act as tracers for the electric field, it seems that *the RF is strongly modifying the E_r profile.* The amplitude of the electric field structure implied by the poloidal velocities as $v_\theta = E_r/B$ is large, up to $E_r = 25$ kV/m.

Since the fast wave [118] begins propagating at $91 - 91.5$ cm, it seems highly unlikely that the effect is a consequence of near fields of the RF antenna which are localized to $R > 91.5$ cm, especially considering that the antenna protection tiles are located at $R = 91.3$ cm and the RF protection Faraday screen is at $R = 92$ cm.

From the GPI observations of this effect caused by different antennas at different plasma currents, and thus different values of the edge safety factor, such as the ones depicted in Figure 6-4 we find that antennas have a unique signature on the velocity field at the gas-puff location. In addition, since in the given example the effect is significantly reduced in amplitude for antenna E, which is farther from the observation site than antenna D, when q_{95} drops from 5.5 to 3.5, these results suggest that the magnetic mapping from the site to the antenna is important in determining the local electric field.

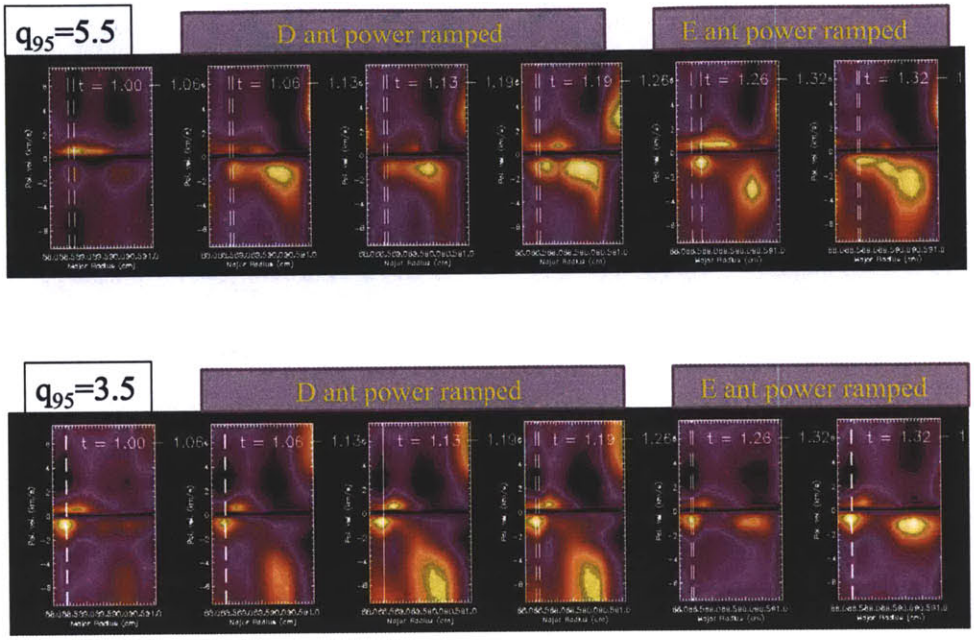

Figure 6-4: Dependence of the poloidal velocity profile in the SOL of RF heated plasmas on current, antennas used and power transmitted.

These results show no dependence on the frequency of the RF wave used or the confinement regime in which the main plasma exists. As for the effect of forward versus inverse magnetic field and plasma current directions, the experiments so far have been largely inconclusive and will in future works need more elaborate analysis techniques.

6.4 Further Studies of Edge Fluctuations

The partially coherent modes in the edges of the recent I-mode regime and the EDA H-mode regime have also gathered a considerable amount of interest lately due to attempts at explaining the decoupling of energy and mass transport channels in the cross field transport. Appendix A reports on some recent studies of these apparently benevolent edge fluctuations. One extremely interesting finding is evidence for a first observation of geodesic acoustic modes on C-Mod. If proven to be GAMs these fluctuations could be used for a more elaborate, two-field spectral transfer anal-

ysis employing the density and velocity fields by combining time delay estimation techniques with the Fourier methods used throughout this thesis.

An additional, completely new path for investigations is delineated in Appendix B, where a newly developed method is explained for estimating temperature fluctuations from GPI signals in the edge plasmas.

Appendix A

Characterization of Partially Coherent Edge Fluctuations

As was shown in the previous chapters, the edge region, in particular the last few centimeters inside the LCFS of certain high energy confinement plasmas exhibits partially coherent modes ("waves") that propagate in the poloidal direction. The two most prominent and persistent features are the QCM of EDA H-modes and the WCM observed only in I-mode plasma discharges; their typical experimental dispersion patterns are shown in Fig. A-1. While the two modes, or quasi-modes, have similar frequencies, wavenumbers and propagation directions, they show a number of clear differences. This appendix is devoted to a detailed analysis of these modes in order to characterize their major dissimilarities and find possible links to physical processes separating them.

In recent years both the EDA H-mode and the I-mode have been identified as desirable high energy confinement regimes [6, 119]. Sections 4.5.4 and 5.2 already discussed the significant role the QCM plays in regulating the edge transport and providing a non-explosive way of releasing impurities and relaxing the pedestal profile. In the I-mode regime the WCM has been implicated as either a contributor to enhanced, essentially L-mode level particle transport [120] or a part of the dynamics leading to the development of an energy transport barrier. As a starting point to our comparison, we first summarize the most obvious and most important similarities

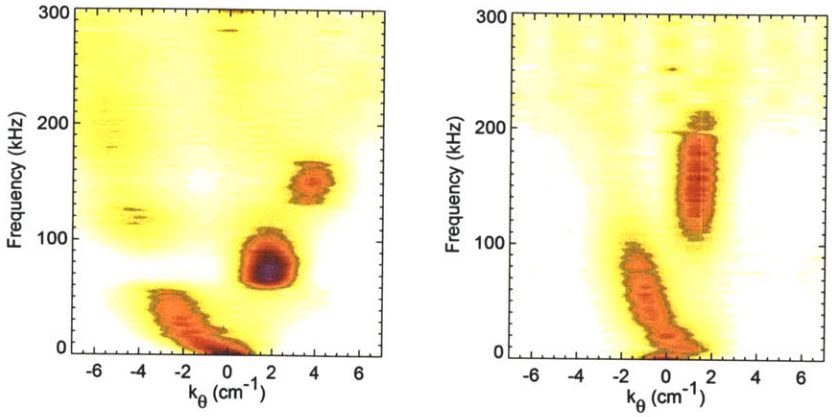

Figure A-1: Conditional auto-power spectra $S(k|f)$ from a radial location of $\rho = -1.2$ cm in an EDA H-mode (left) and an I-mode (right) confinement regime. Both features appear with small positive poloidal wavenumbers k_θ, corresponding to a propagation in the EDD sense in the lab frame. Note the difference in mode widths Δf, the harmonic structure exhibited by the QCM but not the WCM fluctuations, and the difference between the speeds of poloidal propagation seen as the slope of the line connecting the mode to ($k_\theta = 0$ cm^{-1}, $f = 0$ kHz)

beyond the positive effect both modes seem to have on the particle confinement in hte plasma, hence serving a positive role in impurity control.

With the sign convention of the spatial and temporal Fourier transforms we apply to the GPI signals, a positive k_θ represents a wave propagation vertically up. The plasma current and toroidal magnetic field directions most commonly used on Alcator C-Mod make this the direction of the electron diamagnetic drift. Figure A-1 makes it quite clear that both the QCM at $k_\theta^{QCM} = 1.8$ cm^{-1}, $f^{QCM} = 75$ kHz and the WCM at $k_\theta^{WCM} = 1.3$ cm, $f^{WCM} = 160 \pm 60$ kHz propagate in the EDD sense. It is worth mentioning that while this has been known for the QCM from multiple measurements (PCI [21], magnetics [121]), GPI is the first diagnostic to show the rotation direction of the WCM. The spectral distributions of the two modes, in fact, seem to be even more similar, with the typical drift-normalized wavenumber of the WCM being in the range $0.09 < k_\theta^{WCM}\rho_s < 0.12$, matching the characteristic size scales quoted in Chapter 4. Although the width of the frequency distribution of the WCM is certainly much larger than that of the QCM in the typical cases demonstrated in the figure (hence the "weakly coherent" mode), it should be noted that QCM's of the same

frequency width as typical WCM's are occasionally observed, especially in transient states. The major spectral differences characterizing the modes will be addressed later in the appendix.

As for distributions in the configuration space, typical examples of QCM and WCM spatial profiles are plotted in Fig. A-2, where it is shown that both the radial location and radial width of the modes are very similar, and place them to approximately $0.7 - 1.0$ cm inside the LCFS, around the middle to top of the temperature (and density) pedestal with a width of about 0.75 cm. The mode amplitude is measured as the integral under the 2D wavenumber-frequency spectral surface with the background turbulence level subtracted as a curve with a constant spectral index; a choice motivated by the results shown in Section 4.4 and further validated *a posteriori* by both radial intensity profiles dropping to essentially zero where the modes are not observed in the conditional spectra $S(k_\theta|f)$. The mode amplitudes are normalized to the average brightness of the GPI signal in the spectrogram bins, taking into account the line sensitivities as will be discussed in App. B, yielding a typical QCM fluctuation amplitude of up to $\delta n/n = 35\%$ and a highly variable WCM amplitude with an average of $\delta n/n = 6\%$ with a maximum of 13%. This difference between mode amplitudes is reproduced in over 30 shots each.

Further inspection of the radial profiles of the mode spectra starts to reveal some key differences. Even though the amplitude profiles are quite similar, the phase profiles of the complex spectra show an important difference. Fig. A-3 summarizes the phase shift results from both EDA H-mode and I-mode discharges in which the full physical width of the modes was within the field of view of the APD system and the GPI was operating with a He puff (the reason of the latter distinction is also addressed in App. B). While no significant phase shifts are detected across WCM's from I-modes with global confinement quality varying between $0.45 < H_{98} < 0.95$, there is a clear trend of increasing phase shifts across QCM's with H_{98}. In addition to the selection of full spatial profiles of the mode, special care was taken to choose QCM's with an amplitude within a 15% range, so as to minimize the differences that might arise due to ionization-shadowing due to atomic physics effects, as described in

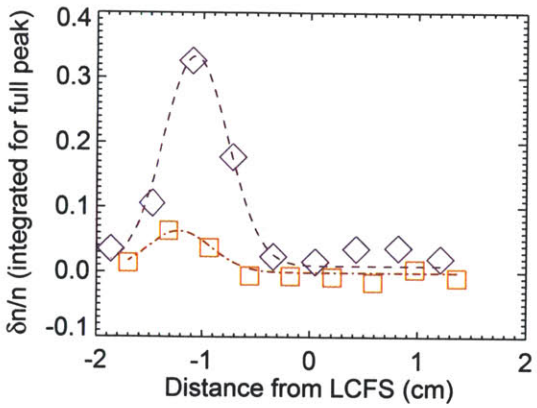

Figure A-2: Radial mode amplitude profiles of the QCM (blue diamonds, dashed line) and the WCM (red squares, dash-dot line). The amplitudes are integrated for the entire mode range in wavenumber and frequency, with the background turbulence subtracted. The spatial width and localization of the two modes are remarkably similar, and measured to be ~ 0.75 cm (FWHM)

[80]. Further, the value of the maximal phase-shift across the mode in weak energy confinement EDA plasmas, well below π, is also inconsistent with the perfectly out of phase structure expected from ionization-shadowing.

An example of a small but substantial phase shift measurement is shown in Fig. A-4; the phase is measured with respect to the center of the peak (zero phase and error bar). The error bar plotted in Fig. A-3 is the maximum of the first five error bars on the left in Fig A-4, providing a fairly conservative estimate considering the trend established by the first four points.

Another feature consistently different between the two edge modes is already demonstrated in Fig. A-1 by the second peak in the QCM spectrum. The appearance of this second feature is very common in EDA H-modes, the GPI system having been the first diagnostic to routinely show its presence through resolving the poloidal wavenumber structure. The latter has also showed this feature to exist at exactly twice the frequency and wavenumber of the QCM, as is required from a harmonic of a fundamental wave. Bispectral analysis of the feature is not only uniquely suitable for constructively proving the existence of phase coupling between the harmonic and the fundamental (thereby affirming the relation as harmonics of the same wave and

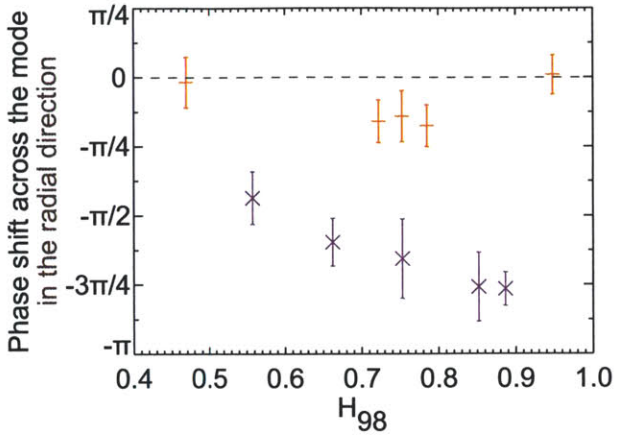

Figure A-3: Trends of the phase shift across the physical width of the QCM (blue x's) and the WCM (red crosses) against $H_{98\text{-ITER}}$ confinement factor. Discharges with a full visible mode structure and a He gas-puff are included only. The error bars represent the maximum measured phase uncertainty between two channels; representative of the average uncertainty in the WCM case and a very conservative estimate for QCM signals.

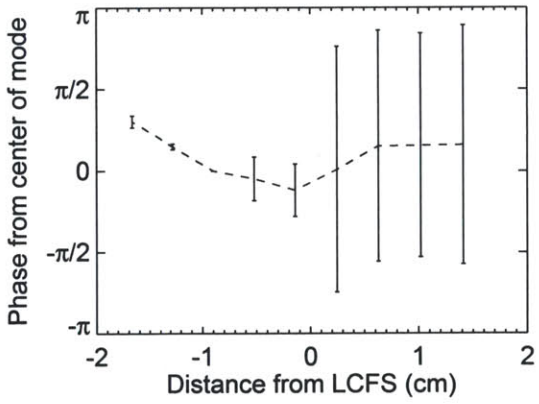

Figure A-4: Phase angle between the signals of a fixed channel (channel 3 from the left in figure) at and around the central frequency of the mode $\phi(f^{QCM} \pm \Delta f)$. Points in the region on the right have large error bars due to the lack of a coherent mode there.

the presence of nonlinearity), it can also demonstrate the presence of the harmonic (or even higher harmonics indeed) if they are not readily apparent from the spectra themselves, due to enhancement through phase locking. With the methods described in App. C, routine bispectral analysis of a single propagation speed signal through an APD column has shown that *the lack of QCM harmonics is, in fact, uncommon in EDA H-mode* discharges in which the mode is visible on at least two radially-resolving viewing columns (half the usual physical width). Examples of GPI auto-bispectra are plotted in Fig. A-5 in order of increasing H_{98}, motivated by the trend seen in Fig. A-3. The peak in the first spectrum at $f_1 = f_2 = 65$ kHz is due to the presence of a harmonic wave at $f_1 + f_2 = 130$ kHz and its being phase coupled to the QCM fundamental. The second graph exhibits two satellites (faintly) at $f_1 = 2f_2 = 2f^{QCM}$ and $f_2 = 2f_1 = 2f^{QCM}$ as a sign of the fundamental coupling to its first harmonic into a second harmonic, and completely similarly, the third graph shows the appearance of a fourth peak in the harmonic structure. Again, it must be registered that the amplitudes of the three QCM's are within 10% of each other, excluding diagnostic sensitivity as the source of the above differences. The mirror symmetry about the $f_1 = f_2$ axis is inherent to an auto-bicoherence spectrum in which only one spectral dimension is concerned. This is effectively the case for Fig. A-5 graphing the root bicoherence squares from

$$b^2\left(f_1, f_2\right) = b^2\left(k_{\theta,1} = f_1/v^{QCM}, f_1; k_{\theta,2} = f_2/v^{QCM}, f_2\right)$$

In effect, this indicates the presence of an increasing strength of nonlinear coupling of the mode towards smaller and smaller features (forward transfer direction) as H_{98} increases.

This trend can be quantified by examining the summed bicoherence estimator for all EDA H-mode shots where the radial center of the QCM amplitude is within the field of view. Since, however, at this point we are not interested in the amount of peak broadening brought about by small velocity jogs, it makes sense to introduce

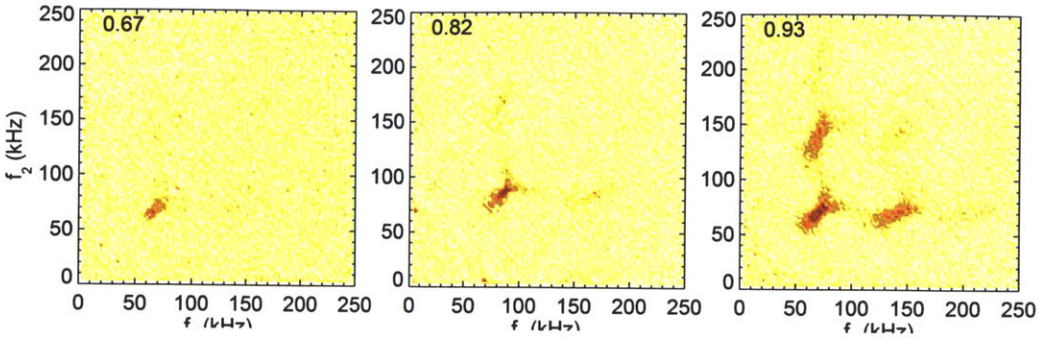

Figure A-5: Bicoherences ($\sqrt{b^2(f_1, f_2)}$) from the EDD spectra in three EDA H-mode discharges of the same experimental run but distinctly different qualities of confinement. The numbers in the top left corner of each graph are the H_{98} factors measured during GPI data collection for the graph. The symmetry about the $f_1 = f_2$ line is inherent to an auto-bicoherence spectrum.

the modified summed bicoherence estimator

$$\hat{b}^2 = \Sigma b^2_{mod} = \left\{ \sum_{f_1,f_2} b^2(f_1, f_2) - \overset{\text{inactive region}}{\sum_{f_1,f_2}} b^2(f_1, f_2) \frac{f_{max} - f_{min}}{f^{\text{inact}}_{max} - f^{\text{inact}}_{min}} \right\} / \Delta f \qquad \text{(A.1)}$$

which picks up only the strength of the forward coupling in the harmonic structure, and is the quantity plotted against H_{98} in Fig. A-6. The result in this figure can be briefly summarized by stating that *the harmonic structure of the QCM tends to be more developed in high "quality" EDA* regimes, perhaps indicating a coupling between confinement and enhanced forward transfer dynamics. It should be mentioned though, that even though no transient EDA H-modes are included in the figure, around $H_{98} = 0.8$ almost the full range of $\hat{b}^2$'s occur, and there is a considerable spread about the least squares fit plotted as a dashed line in the figure; however, no trend has yet been found vs I_p, q_{95}, B_T, $\bar{n_e}$ or P_{ICRF}, the most obvious candidates for determining macroscopic quantities.

The comparison of these features and the bicoherence spectra recorded from the edge of I-mode plasmas shows a striking difference. At no values of the confinement factor do the WCM spectra exhibit a harmonic structure. Since the Nyquist frequency of the GPI system is at 1 MHz and the wavenumber cutoff is just above $k_{\text{max}} = 7\ \text{cm}^{-1}$, the diagnostic should be more than adequate to record any higher harmonics.

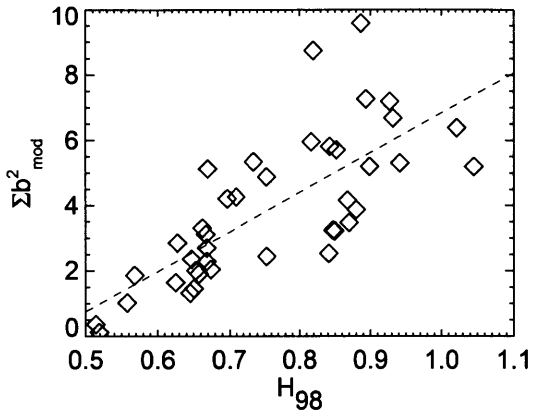

Figure A-6: Total bicoherence estimator Σb^2_{mod} (see text) against confinement coefficient H_{98} in the EDD fluctuation from EDA H-modes in which at least the expected center of the mode ($\sim$ 0.8 cm, two channels) is seen in GPI views. The dashed line is a least squares fit.

Nevertheless, the bicoherence spectra of WCM signals (Fig. A-7) above the WCM frequency are completely featureless. Therefore this difference must be attributed to the physics of the modes themselves.

Even though the WCM exhibits neither a harmonic structure nor a trend in total estimated bicoherence against global confinement quantities (such as H_{98}, the stored energy W_{plasma} or the confinement time τ_E), it still does provide valuable and nontrivial physical information in both respects.

First, the auto-bicoherence spectra generated at the radius where the WCM ampliude is maximum, have a clear coupling feature between a narrow mode around $f^{\text{res}} = 15 - 30$ kHz (a sharp $f^{\text{res}} = 20$ kHz in the sample spectrum in Fig. A-7) and the entire frequency range of the WCM. Note that these auto-bicoherence spectra are generated in the same way as those for the QCM. The presence of this phase coupling is especially surprising considering that the conditional spectrum of the same time segment of the same shot (leftmost contour plot in Fig. A-7) has no conspicuous mode at this frequency.

In order to scan for further nonlinear interactions, which may occur between the WCM and the IDD propagating turbulence, a small section of which might be the

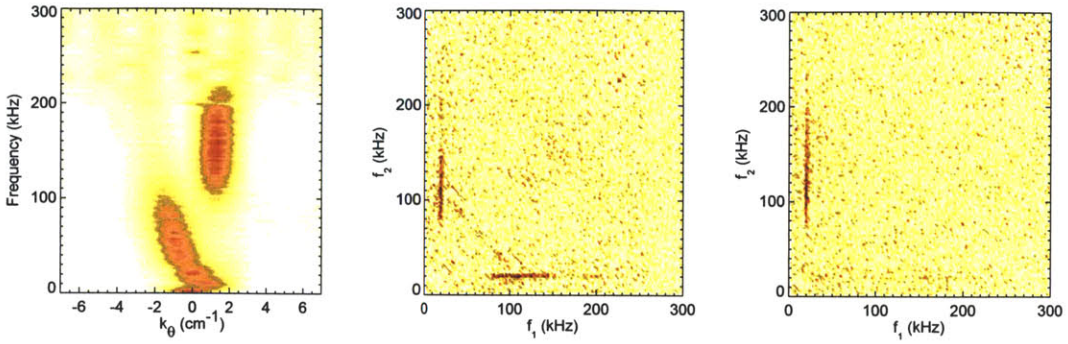

Figure A-7: Phase coupling structure in I-mode edge fluctuations; (from left to right) A-7a - the conditional spectrum $S(k_\theta|f)$; A-7b - the auto-bicoherence spectrum $\sqrt{b^2(f_1, f_2)}$ along the WCM quasi-mode in the EDD direction (dashed line in Fig a.); A-7c - the section of the 2D k, f auto-bicoherence spectrum $\sqrt{b^2(k_{\theta,1}, f_1; k_{\theta,2}, f_2)}$ between the IDD lobe (solid line in Fig a.) and the EDD propagating WCM. Note the $k_\theta = 0$ cm^{-1} direction reversal point in Fig a. at the peak in the f_1 frequency in Fig. b and c.

narrow line appearing in an EDD-only autobicoherence, we generated the full 2D auto-bicoherence spectrum $b^2(k_{\theta,1}, f_1; k_{\theta,2}, f_2)$ and interrogated it for features along various v^{IDD} and $k_{\theta,1}$ values. The result is that no spectra exhibit a broad $f_1 - f_2$ feature, but the narrow line in the bicoherence showing coupling between the sharp mode and the WCM persists so long as the $k-f$ region at $k_\theta = 0 \pm 1$ cm^{-1}, $f = 20$ kHz is included in the non-WCM component of the bispectrum. Searching specifically for such a feature in the spectrum turns out to be quite fruitful in fact. In the sample spectrum provided, the propagation direction of the dominant features flips sign at exactly this spectral range, and a mode-like peak can be observed at this location between the two lobes. Upon further scrutiny, this coupling feature turns out to be common to most well diagnosed I-modes, and the propagation reversal point is absolutely ubiquitous in all I-modes.

While the source of this low frequency mode is as yet unknown, one must note the significant similarity of our bispectra to those shown by C. Holland[114], where the feature was unequivocally identified as a geodesic acoustic mode (GAM) and its coupling to the main turbulence was established a source of spectral transfer. In terms of spectral location, after accounting for the geometric differences between

DIII-D and C-Mod, the frequency range of GAM oscillations should be exactly where the coupling peak occurs in these I-mode plasmas[115, 122, 123]. Additionally, we expect $k_\theta^{\mathrm{GAM}} = 0$ cm^{-1}, since GAM's are purely radial electrostatic modes, causing entire plasma shells to rotate together. Even though some I-mode shots operate with fairly low edge safety factors ($q_{95} < 3$), in which GAM oscillations are expected to be strongly Landau damped [124], many I-modes occur at higher values of the safety factor: $3 < q < 5$. In this range of q, a finite GAM amplitude has been observed on DIII-D [123, 124].

The identification of this mode as GAM would be the first observation of their existence in C-Mod plasmas; but beyond that, this opens up the possibility of the higher level bispectral analyses discussed previously in the section on the criticism of single-field models for spectral transfer. In addition, such a mechanism would explain why the WCM exists at a very well defined wavenumber and yet a broad frequency range, resulting from Doppler-broadening from a relatively large range of poloidal velocities.

It was noted above that neither the phase across the WCM, nor the phase coupling therein exhibits any trends as a function of the quality of global confinement. An early observation of the highly variable center frequency of the mode, however, motivates a closer look at the propagation speed of WCM in the lab frame in this aspect. Fig. A-8 summarizes the phase velocity fits through the center of the peak in k-f space from all I-mode shots on C-Mod since Feb 2010 with a diagnostic gas-puff.

The figure shows that the propagation direction of the WCM is consistently in the EDD in the lab frame, but more importantly, that the phase velocity of the center peak in the lab frame increases steadily with H_{98}.

The observations summarized here come together into a consistent picture if we attempt to relate them to the underlying flow (or more precisely, the radial electric field) structure. The local time-average radial electric field can be expressed from the radial force balance equation. In an equilibrium, the momentum equation reduces to

$$0 = Z_i e n_i \left(\mathbf{E} + \mathbf{v}_i \times \mathbf{B}\right) - \nabla p_i$$

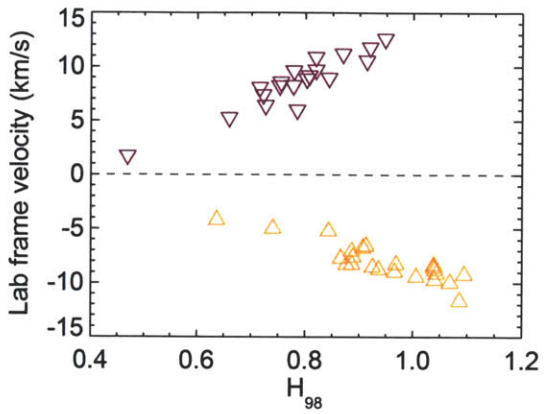

Figure A-8: Phase velocity of the center of the WCM peak as observed from the lab frame against the confinement factor H_{98}. Both propagations are in the EDD direction, positive velocities belong to shots with a "normal" plasma current (I_p) and toroidal magnetic field (B_T) direction (purple "down" triangles), and negative velocities to those with a "reversed" field direction (orange "up" triangles).

which, upon multiplication by $\hat{\mathbf{r}}$ and rearrangement becomes

$$E_r = \frac{1}{Z_i n_i e}\partial_r p_i - v_{\phi,i}B_\theta + v_{\theta,i}B_\phi \tag{A.2}$$

for any species "i" in the plasma, where Z_i is the species charge, n_i its number density, p_i its pressure.

Using expression A.2, charge exchange recombination spectroscopy (CXRS) measurements can provide all of the information necessary to determine E_r. The radial electric field profiles in Fig. A-9 were produced in this manner.

The most prominent feature in the figure is the E_r well which develops in I-mode and is even deeper in the EDA H-mode case. The radial location of this well is within error with the typical location of the QCM and WCM fluctuations, as was reported on multiple occasions [21, 125, 120] for the QCM. Note also, that as one of the major findings of previous studies of the E_r well in C-Mod [126, 6] showed, *the width and the radial location of the E_r wells are robust* through confinement modes, similarly to the radial mode structures.

Electric field measurements from the CXRS system are less readily available than

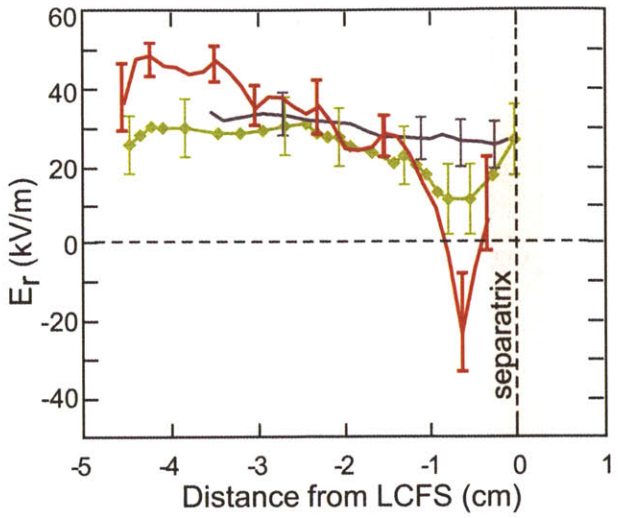

Figure A-9: Radial electric fields measured by charge exchange recombination spectroscopy; blue: L-mode, green: I-mode, red: EDA H-mode; after McDermott[6]

GPI signals, which means that at this point we are not yet able to reproduce Figs. A-3 and A-6 against the local E_r. One of the main results of previous C-Mod studies of the edge pedestal on the other hand informs us that the depth of the radial electric field well, or alternatively the magnitude of the E_r shear (constant width), shows a strong correlation with improved plasma energy confinement, see Fig. 6-3. in [126].

Since a strongly sheared background $\mathbf{E}\times\mathbf{B}$ flow is expected to cause a radial phase shift in a mode which spans the sheared region (convection), the growth of the phase shift with H_{98} ties in well with the aforementioned results. Indeed the increasing rate of forward coupling, and in fact the strength of higher harmonics of the mode might be connected to this point as well. In the simplest edge turbulence models, where $\tilde{n}_e$ is strictly adiabatically tied to $\tilde{\phi}_e$, we expect a positive vorticity at the leading edge of a sheared mode, similar to a 2D fluid flow (as in a Kelvin-Helmholtz instability), which should drive the wave form non-sinusoidal in a harmonic manner. The analogy is of course not complete because the parallel dynamics introduces a dissipative coupling between density and potential fluctuations, so that even in the simplest case we have a finite (though often small) term on the RHS of the vorticity equation

$$\left[\partial_t - \nabla\phi\times\hat{\mathbf{z}}\cdot\nabla\right]\nabla^2\phi = \nabla_\parallel(n-\phi)$$

Nevertheless the hydrodynamic analogy informs us about the possible connection between the two results, the confinement dependence of the phase shift and that of the nonlinear wave form.

Relating the WCM result demonstrated in Fig. A-8 to the E_r structure and *its* correlation with plasma confinement brings up the important issue of the propagation velocity of the two modes *in the plasma frame.*

Even though both the QCM and the WCM go around the plasma edge in the EDD direction, the E_r profiles in Fig. A-9 warn us that the situation may be different in the co-moving frame. Carrying out the analysis for two representative shots, we indeed find the propagation velocities given in Table A.1. If both the GPI and the CXRS localization are within $\sim$ 2 mm of each other, this means that *the WCM and the QCM propagate in opposite directions in the plasma frame*, with the QCM moving in the IDD direction and the WCM in the EDD. Since a *negative* radial electric field drives a flow in the *electron* diamagnetic drift direction, the increasing speed of the WCM with H_{98} may be interpreted as a consequence of the E_r well depth correlation to confinement, demonstrated in [126].

Table A.1: Comparison of QCM and WCM propagation speeds in the lab frame and the plasma frame

	$v_{\text{lab}}^{\text{mode}}$	E_r	$v_{\text{plasma}}^{\text{mode}}$
QCM	2.5 km/s	-44.5 ± 15 kV/m	-4.5 to -13.5 km/s
WCM	10.1 km/s	-20 to 18 kV/m	4.5 to 14.5 km/s

Finally we should mention that this interpretation is further corroborated by the characteristic onset spectrogram of the two modes plotted in Figs. 5-2 and 5-4, where the QCM's typical "spin-down" is contrasted with the slightly increasing frequency of the WCM as their respective high confinement regimes develop from an L-mode plasma.

Appendix B

Measurement of Temperature Fluctuations using GPI

Although in the previous appendix the WCM was presented as a rather conspicuous feature of the I-mode edge, well diagnosed by GPI, the fact that it was not originally found by GPI, but by reflectometry is due to a discrepancy between the measurements of these diagnostics in the I-mode, reported by Hubbard [120]. The relative amplitude of the WCM compared to that of the low frequency turbulence is an order of magnitude higher in the O-mode reflectometry responses than in GPI. At the description of the principles of the diagnostic in Chapter 3.1 and at the main results in Chapter 4 it was mentioned that the neutral emissions recorded by GPI are sensitive to both n_e and T_e; and it was argued that the primary source of fluctuations is the density fluctuation $\tilde{n}_e$. The purpose of this appendix is to expand on this argument and explore the more accurate parameter dependence of the brightness signals, in order a) to support it for the cases in Chaps. 4 and A, b) to make an attempt at resolving the aforementioned discrepancy and finally c) to propose a way to diagnose T_e fluctuations by a simple GPI system.

The response of the neutral gas to the plasma is calculated by collisional-radiative models, and, for example, is implemented in the DEGAS2 neutral transport simulation code [80]. The outputs relevant to our measurements are as follows. The density

of the hydrogen $n = 3$ excited state can be found with

$$N_3 = \left(\frac{N_3^{(i)}}{N_1}\right) N_1 + \left(\frac{N_3^{(ii)}}{n_i}\right) n_i.$$

The corresponding emission rate for the Balmer-α line is given by $N_3 A_{23} = N_3 4.41 \times 10^7$ cm^{-3}s^{-1}. For Helium emssions, the DEGAS2 code, even more conveniently, generates an output of emission rates which combined with the ground state and ion densities yield the total emitted power in the line:

$$P_{5877} = P_{5877}^{(i)} N_1 + P_{5877}^{(ii)} n_i$$

Considering that the puff introduces a highly non-equilibrium amount of neutrals to the plasma edge for both gases, D_2 and He, we may work with the assumption that the primary source of the excited state is from the transported neutrals, and neglect the recombination source. All these output quantities are tabulated for a wide range of n_e and T_e combinations. Evaluating the functions of emitted power for the relevant parameter range shows that to an excellent approximation, the emitted energy locally behaves as

$$I_{\mathrm{GPI}} = A n_e^{\alpha_n} T_e^{\alpha_T}, \tag{B.1}$$

where A is a proportionality factor, which still depends on the local density of neutrals, etc, mostly unimportant for our analyses, as it will be seen. The exponents for the density- and temperature dependence can be generated from the code output in a straightforward way. Their values are plotted in Figs. B-1 and B-2 over the ranges relevant for the edge plasmas in C-Mod.

First, we must notice that in the density and temperature range where our Ohmic L-mode and most of the EDA H-mode results from the edge and separatrix regions were obtained in Chapter 4, $\alpha_T \approx 0$ or at most $\approx \pm 0.1$, contrasted with an α_n density fluctuation sensitivity larger by at least a factor of 3 in He and a factor 6 in D. This is exactly the reason why in Chapter 4 we simply neglected the effect of electron temperature on the observed brightnesses. The second thing to observe is

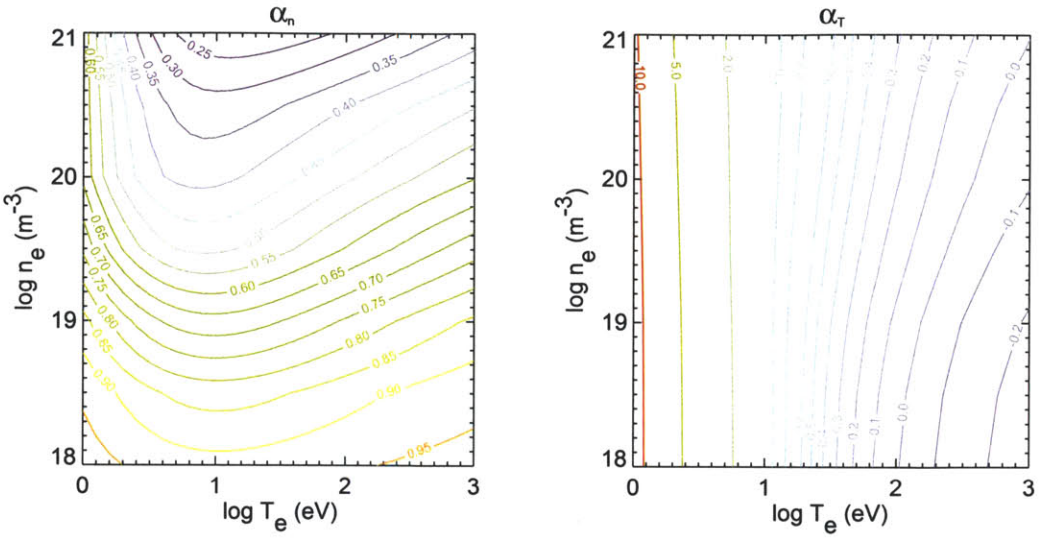

Figure B-1: Exponents of electron-density and -temperature dependence of the D Balmer α $\lambda = 656.1$ nm line brightness in a deuterium gas-puff.

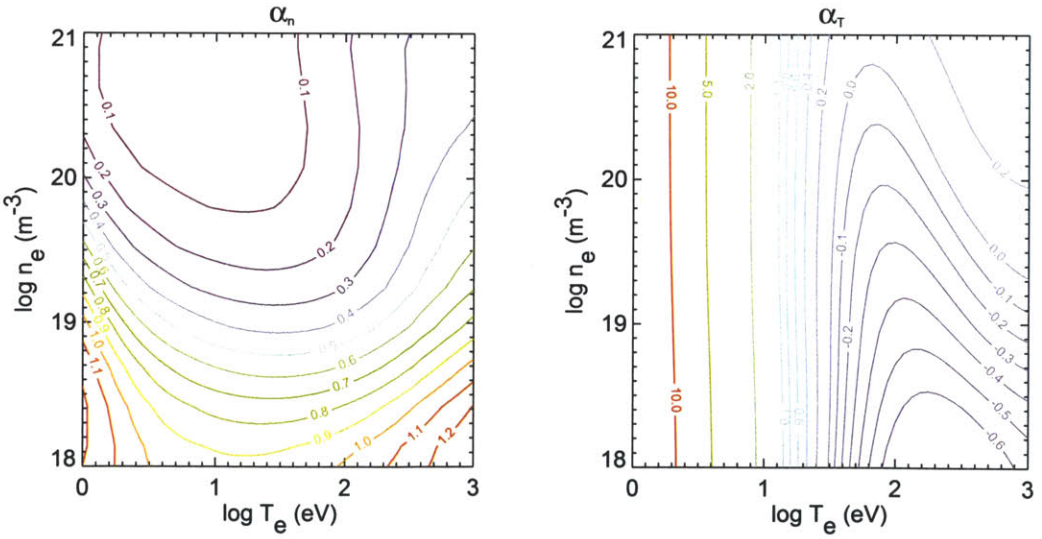

Figure B-2: Exponents of electron-density and -temperature dependence of the HeI $(3^3D \rightarrow 2^3P)$ $\lambda = 587.6$ nm line brightness in a He gas-puff.

that in the graph for the D exponents, there is a significant shift from a $\alpha_{T,D} \approx 0$ in the case when the plasma enters an I-mode. This is due to the fact that at the typical densities ($\mathcal{O}(10^{20}$ m^{-3})) and temperatures ($\mathcal{O}(100$ eV)) of the L-mode edge, the iso-contours of $\alpha_{T,D}$ are oriented along growing n_e and T_e, so luckily, a regular L-to-H mode transition leaves $\alpha_{T,D}$ close to zero. As it can be read from Fig. B-1, a typical L-mode edge at $\rho = -1$ cm with $n_e = 0.6 \times 10^{20}$ m^{-3} and $T_e = 200$ eV has $\alpha_{T,D} \approx 0.05$, and $\alpha_{n,D} \approx 0.65$, a typical H-mode at $n_e = 1.5 \times 10^{20}$ m^{-3} and $T_e = 500$ eV would have $\alpha_{T,D} \approx 0.0$ and $\alpha_{n,D} \approx 0.45$; however, since the particle and heat transport decouple in I-mode, a regular I-mode edge in the parameter range $n_e = 0.6 \times 10^{20}$ m^{-3} and $T_e = 500$ eV has an $\alpha_{T,D} \approx -0.1$ and $\alpha_{n,D} \approx 0.7$.

Now, in order to understand and exploit the sensitivities of the signal levels to the average electron density and temperature, let us write down the brightness-fluctuation of GPI signals expected from Eq. B.1:

$$\begin{aligned}
\tilde{I} = I - I_0 &= A\left[n^{\alpha_n} T^{\alpha_T} - n_0^{\alpha_n} T_0^{\alpha_T}\right] \\
&= A\left[n_0^{\alpha_n}\left(1+\frac{\tilde{n}}{n_0}\right)^{\alpha_n} T_0^{\alpha_T}\left(1+\frac{\tilde{T}}{T_0}\right)^{\alpha_T} - n_0^{\alpha_n} T_0^{\alpha_T}\right] \\
&\approx A\left[n_0^{\alpha_n}\left(1+\alpha_n\frac{\tilde{n}}{n_0}\right) T_0^{\alpha_T}\left(1+\alpha_T\frac{\tilde{T}}{T_0}\right) - n_0^{\alpha_n} T_0^{\alpha_T}\right] \\
&\approx A\left[n_0^{\alpha_n} T_0^{\alpha_T}\left(\alpha_n\frac{\tilde{n}}{n_0} + \alpha_T\frac{\tilde{T}}{T_0}\right)\right]
\end{aligned}$$

which gives us a normalized brightness-fluctuation of

$$\frac{\tilde{I}}{I_0} = \alpha_n\frac{\tilde{n}}{n_0} + \alpha_T\frac{\tilde{T}}{T_0}. \tag{B.2}$$

Since in the edge we gather most of our information from spectrograms, let us consider a spectral decomposition. In the most general case, the Fourier components at a given

frequency of the two fluctuations can take the form

$$\tilde{n} = \delta n \cos(\omega t) \tag{B.3}$$

$$\tilde{T} = \delta T \cos(\omega t + \phi_{n,T}(\omega)), \tag{B.4}$$

where $\phi_{n,T}(\omega)$ is the relative phase angle between density and temperature fluctuations. If we substitute expressions B.3 and B.4 into the general form of the normalized brightness-fluctuation, we are led to

$$\frac{\tilde{I}}{I_0} = \alpha_n \frac{\delta n}{n_0} \left[\cos(\omega t) + \frac{\alpha_T}{\alpha_n} \frac{\delta T/T_0}{\delta n/n_0} \cos(\omega t + \phi_{n,T}(\omega)) \right]. \tag{B.5}$$

With Thompson-scattering measurements of the edge n_e and T_e profiles, one can evaluate the $\alpha_{n,T}$ at the location of the GPI measurement, so that the above expression contain three unknown quantities: the density and temperature fluctuation amplitude $\delta n/n_0(\omega)$ and $\delta T/T_0(\omega)$, respectively, and the spectrum of the phase angle $\phi_{n,T}(\omega)$ between the two.

For the Fourier amplitudes of the expression in B.5, one can solve numerically for every single ω, or alternatively after some analytic manipulation we may arrive at the approximate formula for the amplitude of a cosine plus a phase shifted cosine of a different amplitude as

$$\text{Amp}\{\cos(x) + R\cos(x+\phi)\} \approx 1 + R\left[2\cos^{2-R}\left(\frac{\phi}{2}\right) - 1\right],$$

plotted as a surface in Fig. B-3. The plot and the analytic form of the expression bring the even parity of the amplitude in the ϕ argument to the surface, which means that the phase shift can be determined up to a sign only.

So for the GPI case the set of equations one has to solve upon recording the spectra $(\delta I/I_0)|_i$ with different neutral gas species is

$$\left.\frac{\delta I}{I_0}\right|_i(\omega) = \alpha_{n,i} \left.\frac{\delta n}{n_0}\right|(\omega) \left[1 + \alpha_{R,i} R(\omega) \left\{ 2\cos^{2-\alpha_{R,i}R(\omega)}\left(\frac{\phi_{n,T}(\omega)}{2}\right) - 1 \right\}\right],$$

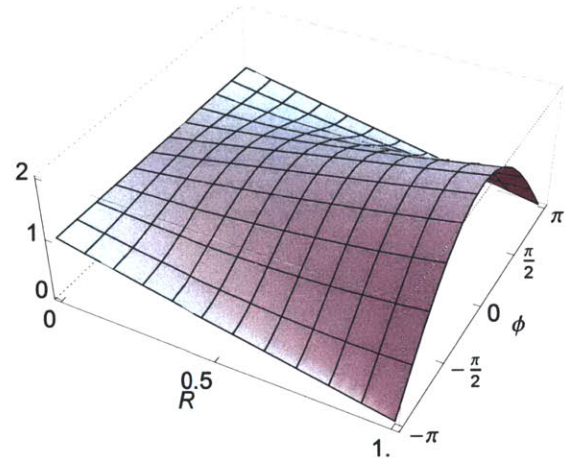

Figure B-3: Apparent amplitude of the combination of density and temperature fluctuations as a function of the sensitivity times fluctuation level and phase angle.

where the intensity ratio $R = [(\delta T/T_0)/(\delta n/n_0)]$ and the (known) sensitivity ratio $\alpha_{R,i} = \alpha_{T,i}/\alpha_{n,i}$ are introduced to simplify notation. Note that $\delta n/n_0$, $\delta T/T_0$ (therefore R) and $\phi_{n,T}$ bear no species index, since they are properties of the plasma turbulence, not the gas puff; and note further that for this measurement one *needs not evaluate the time histories of* $\tilde{n}$ *and* $\tilde{T}$, rather only their power spectrum, a stationary, integral property. Even though one does not gain a direct measurement for $T_e(t)$, the method provides information about the nature of the fluctuations while having the advantage of avoiding the issues which would arise from the inequality of the atomic de-excitation rates of the different observed lines, should the atomic physics of any one of them include a slow transition, whose speed be comparable to turbulent time scales. Moreover, so long as a reproducible, steady plasma is examined – one with a well-behaved, stationary turbulence spectrum – the two measurements can be done at different times, indeed in different incarnations of the same plasma.

Since the current setup of GPI at C-Mod can operate with either He or D gas-puffs, a single variable expression for two out of the three unknowns can be determined without any further assumptions by repeating a well-controlled shot. For a full characterization, one may accept reflectometric measurements of $\delta n/n_0$, eliminating the last unknown component and generating full $\delta T/T_0(\omega)$ and $\phi_{n,T}(\omega)$ spectra; or in order to avoid relying on complex measurements like reflectometry, the following

simplifying assumption can be made.

If we consider the small fluctuations of n_e and T_e in a non-zero gradient background, to first order these may be approximated as the displacement ξ of a small element of the plasma:

$$\delta n = \xi \nabla n$$
$$\delta T = \xi \nabla T.$$

Substitute into Eqn. B.5 to get

$$\frac{\tilde{I}}{I_0} = \xi \frac{1}{L_n} \left[\cos(\omega t) + \frac{\alpha_T}{\alpha_n} \frac{L_n}{L_T} \cos(\omega t + \phi_{n,T}(\omega)) \right],$$

which with the same analytic approach as above yields

$$\left. \frac{\delta I}{I_0} \right|_i (\omega) = \xi(\omega) \frac{\alpha_{n,i}}{L_n} \left[1 + \alpha_{R,i} \frac{L_n}{L_T} \left\{ 2 \cos^{2-\alpha_{R,i} L_n / L_T} \left(\frac{\phi_{n,T}(\omega)}{2} \right) - 1 \right\} \right], \qquad \text{(B.6)}$$

where L_n and L_T are the density- and temperature-gradient scale lengths respectively. This form of the assumption shows that it considers the phase angle between temperature and density oscillations alone to be the source of the difference between the recorded spectra; and it leaves us with the displacement spectrum $\xi(\omega)$ and the phase spectrum $\phi_{n,T}(\omega)$, which can then be fully determined from the two GPI measurements currently available.

The analysis method just delineated marks the path for two potential future upgrades of the GPI system, enabling it to perform routine measurements of $\tilde{T}/T_0(\omega)$ and $\phi_{n,T}(\omega)$. The most inexpensive upgrade, (A) selectivity for a third line besides the He 587 nm and D 656 nm lines, would enable the GPI to be entirely independent of both a separate measurement of $\delta n/n_0$ and the assumption B.6. Unfortunately, this upgrade would still leave the strain of needing to reproduce the same plasma with the same stationary statistics reliably multiple times. Expanding the system (B) to accommodate for simultaneous detection of the different line radiations could, however overcome this shortcoming as well.

Appendix C

Details of Analysis Techniques

C.1 Time Delay Estimation

A common method for estimating velocity fields from fluctuation signals recorded at different locations is the use of time delay estimation (TDE) techniques. The method is useful in situations where the locations of observation are close enough to each other for the fluctuations to stay coherent as they travel from one point to the next. This is obviously the case in any situation for which the Taylor hypothesis [77] is applicable. What is required is for the correlation time τ_c of the fluctuations to be longer than the time it takes for the flow or propagation to move the perturbations from one observation point to the next, i.e. $\tau_c > \Delta/v$, where Δ is the separation between the points of observation and v is the phase velocity of perturbations. Here the correlation time represents the e-folding time of the cross-correlation function

$$\rho_{xy}(\tau) = \frac{1}{\sigma_x \sigma_y} \langle (x(t) - \langle x \rangle)(y(t+\tau) - \langle y \rangle) \rangle \,, \tag{C.1}$$

at the time lag τ_d which maximizes $\rho_{xy}(\tau)$, where $x(t)$ and $y(t)$ are the two fluctuation signals, and σ_x and σ_y are their respective variances. By definition, the cross-correlation function takes values from the $[0, 1]$ interval, and the validity of the TDE can be tested by the value $\rho_{xy}(\tau_d)$. The condition above dictates that the method can be considered absolutely reliable for a value of $\rho_{xy} \gtrsim 1 - 1/e \approx 0.63$, and it is

commonly deemed unreliable below a value of $\rho_{min} \approx 0.36$ (twice the e-folding value). For the adjacent channels on the GPI APD array, this condition is generally satisfied with cross correlation values around ~ 0.75 and up to ~ 0.9. The velocity of emission features can then simply be calculated as

$$v = \Delta/\tau_d. \tag{C.2}$$

The advantages of this method over the one described in Chapter 4 using the conditional spectra $S(k_\theta|f)$ are that (1) measurements only need to be made at two points, therefore a 2D velocity space can be mapped out, (2) since it was shown that fully converged spectra can be generated only over $\sim$ 15 ms for the generally used frequency resolution of df = 2 kHz, TDE methods can provide much better time resolution for velocity measurements. Indeed, marginally reliable velocity estimates have been calculated from as few as 20 samples in recent studies [122], which when applied for the C-Mod GPI diagnostic would provide a time resolution up to ~ 10 μs. This method was in fact used in this thesis in order to find regions where the radial propagation was dominant (or negligible, as in the edge), since such a search requires spatially resolved measurements.

However, there are three major disadvantages to this method. Firstly, due to the use of the cross-correlation function, the method is inherently weighted towards the fluctuations with the largest amplitude. In the case of edge GPI signals, this means (a) being weighted to the lowest frequency part of the spectrum, (b) being sensitive to basically exclusively to the largest blobs in the SOL. The former can be a problem because the linearity of the experimental dispersions is not established *a priori*, and any deviation from linearity will go unnoticed if one is limited to a TDE technique. The latter on the other hand is problematic for two reasons: (1) the motion of blobs strongly depends on their size scale [69] and therefore the frequency range used to determine the velocity, therefore small features and their corresponding experimentally interesting velocities are effectively lost for the study, and (2) blobs have been shown to be good tracers for the background velocity field in the far SOL

[84], but they strongly deviate from this field in the near SOL (which was also shown in Chapter 4). Secondly, in a region where counter-propagating fluctuation features exist the TDE technique cannot resolve the two velocities, but will rather provide velocity estimates with an average between the velocities of the two features and very large variances. Since in the region between the edge and the SOL features of this kind indeed dominate the fluctuation field, TDE techniques miss the fine structure of the radial velocity profile. Thirdly, in regions where bright, coherent features are rare, there are very few points for the TDE analysis to lock into, and estimation errors will go very large in the absence of somewhat sophisticated post-processing (such as in [84]).

The technique is implemented for the C-Mod GPI diagnostic in the IDL language, as listed below.

C.2 Definitions of Objects for Fourier Analysis

Many mathematical objects in the analysis used in this thesis are based on spectrograms. Spectrograms are also known as short-time Fourier transforms and are used to determine the frequency and phase content of local sections of a signal as it changes over time. Here we clearly describe how these are generated and how the more complicated objects are formed from them.

We assume there is an analog signal x(t) which we sample at times separated by dt the time resolution for a period of length T, generating the discrete signal

$$\{x(j\,dt)\}_{j\in M}\,,$$

where $T = M\,dt$, M an integer, and $j \in M$ for an indexing array is interpreted as j an integer for which $0 \leq j < M$. In order to retain some time resolution, the Fourier transform is not performed on the entire discrete signal, but rather on N short *bins* thereof of length $\tau = M/N\,dt$, which are also known as epochs:

$$S_x(j,k)_{j\in M/N;k\in N} = \left\{\mathcal{F}\left(\{x(k\,\tau + j\,dt)\}_{j\in M/N}\right)\right\}_{k\in N}\,,$$

where $\mathcal{F}$ denotes a Fourier transform, which in our case is a fast discrete Fourier transform. In addition, a window function, such as a Hanning filter, or a Gaussian bell curve, with the same number of points (M/N) as the bins can be used to multiply the signals before transformation in order to avoid spurious peaks due to the discontinuous ends of the bin. The bins may also overlap to provide smoother time histories of the spectra. Since the samples are all real, the complex Fourier spectra will be redundant. The first half of S_x is what is used throughout the main chapters and is commonly denoted

$$X(f,t) = S_x(j,k)_{j\in M/2N;k\in N}.$$

The frequency resolution and maximum frequency are then given by

$$df = \frac{1}{\tau}$$

and

$$f_N = \frac{M}{2N}df,$$

respectively, where f_N is known as the Nyquist frequency. The above procedure is implemented in the IDL language for the C-Mod GPI diagnostic as listed below.

The time index k (or t in the shorthand version) is considered to be "slow" time, and averages of the form $\langle . \rangle_t$ in Chapter 4 are meant over this index. Thus, the power spectrum of $x(t)$ for instance is

$$P_X(f) = \frac{1}{N}\sum_t X(f,t)\overline{X}(f,t).$$

The wavenumbers are extracted from the spatially separated signals by a true Fourier transform on the vertical columns of the GPI views. This transform takes the actual physical locations of the viewing spots into account and is performed in the matrix form, since it is implemented in the IDL language (see below). For this method the matrix of Fourier components is written as

$$\mathrm{C} = \exp(i\,\mathbf{z} \circ \mathbf{k}),$$

where i is the imaginary unit, $\mathbf{z}$ is the vector (n-tuplet) of viewing locations, $\mathbf{k}$ is the vector of required wavenumbers and $\circ$ denotes a dyadic product, $C_{jk} = \exp(i\, z_j k_k)$. Then using tensor notation on the spatially resolved Fourier spectra as

$$X_{jkl} = X(z_l; f_k, t_k)$$

The wavenumber and frequency spectrum S is calculated as $\mathrm{S} = \mathrm{X} \cdot \mathrm{C}$, where $\cdot$ is the regular tensor multiplication, also known as index contraction. Thus, the array $S(k, f, t)$ will have as many points in the k dimension as did the n-tuplet of required wavenumbers. This means that the method can be simply adapted to any required oversampling in wavenumber for smoother spectra. The wavenumber resolution and the Nyquist wavenumber are defined similarly to the frequency counterparts (cf. the implemented form below).

This method is used throughout this thesis instead of the popular two-point technique [76] for calculating wavenumber frequency spectra. In the two-point technique two spectrograms $X(f,t)$ and $Y(f,t)$ are generated from signals at two locations separated by a distance Δ. The phase between the components of the two spectra, known as the cross-phase, is calculated as

$$\theta(f,t) = \arg(X(f,t)\overline{Y}(f,t)),$$

where arg is the function operating on complex numbers giving the angle between the line joining the point to the origin and the positive real axis, so that by definition $z = |z|e^{i\arg(z)}$ for all complex z. Hence the wavenumber spectrum is calculated as

$$K(f,t) = \theta(f,t)/\Delta.$$

Finally, the wavenumber–frequency spectrum is defined as

$$S_{\mathrm{2point}}(k,f) = \left\langle P_{(X+Y)/2}(f,t)\mathrm{I}_{\delta k}(k - K(f,t))\right\rangle_t, \tag{C.3}$$

where the discrete delta function is defined as

$$\mathrm{I}_{\delta k}(\xi) = \begin{cases} 1 & \text{where } -\delta k/2 \leq \xi < \delta k/2 \\ 0 & \text{elsewhere.} \end{cases}$$

The major disadvantage because of which this is not the method used in this thesis is the following. As is clear from the definition Eq. (C.3), the two-point technique forces the spectrum to have a single wavenumber for every frequency. If the sampled spectrum features multiple wavenumbers at a given frequency, the two-point wavenumber and frequency spectrum misrepresents the nature of these fluctuations unless the two (or more) features switch between each other on a time scale that is slower than the slow time in the spectrograms. With the characteristic time ~ 100 μs of the switching between the two features in the crossover region between the edge and the SOL, two-point spectra could only correctly represent the fluctuations at a fairly crude frequency resolution of $df > 10$ kHz. However, even this boundary cannot be known *a priori*, but is rather determined from the more accurate spectra used in the thesis.

Finally, in the energy transfer analysis, the matrix notation was used for the vector of the third order moments of spectra and the matrix of the fourth order moments. With the notations of Chapter 4, for a given sum frequency f_j:

$$\mathbf{A} = \begin{pmatrix} \langle X(f_j/2)X(f_j/2)\overline{X}(f_j)\rangle \\ \langle X(f_{j+2}/2)X(f_{j-2}/2)\overline{X}(f_j)\rangle \\ \vdots \\ \langle X(f_N)X((f_j - f_N))\overline{X}(f_j)\rangle \end{pmatrix}; \; \mathbf{B} = \begin{pmatrix} \langle X(f_j/2)X(f_j/2)\overline{Y}(f_j)\rangle \\ \langle X(f_{j+2}/2)X(f_{j-2}/2)\overline{Y}(f_j)\rangle \\ \vdots \\ \langle X(f_N)X((f_j - f_N))\overline{Y}(f_j)\rangle \end{pmatrix};$$

$$\mathrm{F} = \begin{pmatrix} \langle X_{j/2}X_{j/2}\overline{X}_{j/2}\overline{X}_{j/2}\rangle & \langle X_{j/2}X_{j/2}\overline{X}_{(j+2)/2}\overline{X}_{(j-2)/2}\rangle & \cdots \\ \langle X_{(j+2)/2}X_{(j-2)/2}\overline{X}_{j/2}\overline{X}_{j/2}\rangle & \langle X(f_j/2)X(f_j/2)\overline{X}(f_j/2)\overline{X}(f_j/2)\rangle & \cdots \\ \vdots & \vdots & \ddots \end{pmatrix}.$$

C.3 List and Usage of Codes

```
TDE VELOCITY CALCULATION
location: /home/cziegler/auxcodes/cor_vel.pro
```

```
function cor_vel,frames,$
                 loc,$
                 time,$
                 fmax_req=fmax_req,$
                 ncor=ncor,$
                 smooth=smooth,$
                 disc=disc,$
                 overlap=overlap,$
                 cor=cor
;INPUTS
;frames   - a 2D array of fluctuation values at locations (1st
;           coordinate) and times (2nd coordinate) - real array
;loc      - a vector of locations, a real array with the same length
;           as the first dimension of the array 'frames'
;time     - a vector of the time base, a real array with the same
;           length as the second dimension of the array 'frames'
;OPTIONAL
;fmax_req - the required Nyquist frequency in kHz, if unspecified
;           ncor will be set to 100
;ncor     - the required number of points used for correlation
;           analysis, if unspecified, ncor will be set to 100.
;           Specifying this value overrides fmax_req.
;cor      - set this equal to a named variable that will contain the full
;           cross correlation function if needed
;KEYWORDS
;overlap - set this keyword if you want to have 50% overlap between
;          neighboring time bins, this quasi-oversampling helps in
;          producing lower noise signals and smoother time traces (recommended)
;smooth  - additional smoothing of the output (not recommended)
;disc    - discard points at which the lag time for maximum correlation is zero
;          (the next, more sophisticated version will adaptively find farther
;          measurement points, until then: highly recommended)
;OUTPUT
;is a structure containing the fields
;vel     - the velocities in units of the location vector divided by units
;          of time
;time    - the time base for vel
;weights - the max correlation coefficients for every point in vel
;td      - indices of the times at which the velocity is finite

VELOCITY SPECTRA FROM VERTICAL COLUMNS (for GAM)
location: /home/cziegler/gpi/GAM_apd.pro
@/home/cziegler/auxcodes/tvplot.pro
@/home/cziegler/auxcodes/blk_fft.pro
@/home/cziegler/auxcodes/cor_vel.pro
pro GAM_apd,frames,$
            time,$
            z_arr,$
            ncor=ncor,$
            df_req=df_req,$
            spec=spec,$
            freq=freq,$
            t_freq=t_freq,$
            r_arr=r_arr,$
            vel=vel,$
            ccoef=ccoef,$
            flow=flow,$
            fhigh=fhigh,$
```

```
            hann=hann,$
            overlap=overlap,$
            voverlap=voverlap
;INPUTS
;frames   - a 3D array of fluctuation values at locations (1st two
;          coordinate) and times (3rd coordinate) - real array
;time     - a vector of the time base, a real array with the same
;          length as the second dimension of the array 'frames'
;z_arr    - a vector of locations, a real array with the same length
;          as the first dimensions of the array 'frames'
;KEYWORDS
;are inherited from BLK_FFT and COR_VEL, voverlap is overlap in the latter
;OUTPUT is a radial profile of poloidal velocity spectra.

SPECTROGRAM
location: /home/cziegler/auxcodes/blk_fft.pro
pro blk_fft,signal,time,df_req,spec,freq,t_freq,$
            normalize=normalize,$
            blk_norm=blk_norm,$
            n_t=n_t,$
            overlap=overlap,$
            hann=hann,$
            padded=padded
;INPUT arguments
;signal - the signal to be block-fft'd. The type can be float or
;         double; 'signal' is allowed to have any number of indices
;         but the last index is always assumed to be the one representing time
;time - the time basis for the signal in seconds (n_elements(time)
;       must be = n_elements(signal(i,..,*)))
;df_req - the required frequency resolution in kHz, provided that the
;         time basis is given in seconds
;
;OUTPUT arguments
;spec - the complex spectrogram of "signal" with the last index
;       being time, and the one but last being the frequency of
;       the transform
;freq - the frequency axis of the block-transform in kHz, provided
;       that the time basis is given in seconds
;t_freq - the time basis for the bins in the same units as time
;
;KEYWORD usage
;normalize - set this keyword if you want the fourier spectra to be
;            normalized according to average intensities in the bins
;blk_norm - set this equal to a named variable that will contain the
;           normalization factors for every bin
;n_t - set this keyword to an integer that will determine how many
;      time bins the block-fourier-transform is going to have
;      Setting n_t will override df_req
;overlap - set this keyword if you want to have 50% overlap between
;          neighboring time bins, this quasi-oversampling helps in
;          producing lower noise signals and smoother time traces
;hann - set this keyword if you want to apply a hanning filter to
;          the time bins before applying the Fourier transformation,
;          this reduces many kinds of noise and it is recommended to
;          be used together with the "overlap" keyword
;padded - if this keyword is set, the last bin is padded with the
;         average of the signals as opposed to zeros (mildly useful)
```

```
SPATIAL FOURIER TRANSFORMATION
location: /home/cziegler/auxcodes/kspec.pro
@/home/cziegler/auxcodes/tensor_multiply.pro
function kspec,spec,xvec,$
                antialias=antialias,$
                odd=odd,$
                k_hann=k_hann,$
                dimension=dimension,$
                inverse=inverse

;INPUT
;spec - a spectrogram of any indices, such as the one generated by blk_fft
;       unless the dimension keyword is specified, the 1st dimension (IDL) is
;       regarded as the spatial location
;xvec - a vector of the spatial locations; xvec has to be the same length
;       as the spatial dimension (default=1) of spec

;OUTPUT
;A structure with the fields kspec and k, where the Fourier-transformed
;array kspec has the same dimensions as spec, except in the transformation
;dimension (default=1), in which it has the same number of elements as
;k - the wavenumbers

;KEYWORDS
;antialias - set this keyword to a number between 0 and 1 to determine
;            at what fraction of the estimated Nyquist wavenumber
;            the spectrum should be cut off
;            in order to minimize aliasing effects (default=0.85)
;odd       - set this keyword to make the kspectrum have an odd number of
;            wavenumbers in it
;k_hann    - set this keyword to perform spatial Hamming filtering
;            in order to minimize first neighbor sidebands
;dimension - set this keyword to the IDL index number of the dimension
;            which represents the spatial dimension (default=1)
;inverse   - set this keyword to perform an inverse transform

ima=complex(0,1) ; imaginary unit
inv=keyword_set(inverse)? -1:1
antialias=keyword_set(antialias)? antialias:0.85
dimension=keyword_set(dimension)? dimension-1:1

;Rearranging dimensions according to requested direction
spsi=size(spec)
dims=spsi[1:spsi[0]]
dexp=dims
dimord=indgen(spsi[0])
dexp[where(dimord ne dimension)]=1
dimord=[where(dimord ne dimension),dimension]
bacord=sort(dimord)
spec=transpose(temporary(spec),dimord)

dummy=reform(xvec)
dummy=dummy[sort(dummy)]
dx=min(dummy[1:*]-dummy[0:n_elements(dummy)-2])
  ;round the resolution to 1st dec place
kmin = floor(10*!pi/(max(dummy)-min(dummy))/2.)/10.
  ;factor to reduce aliasing effects
kmax = !pi/dx*antialias
klen = 2*round(kmax/kmin)+keyword_set(odd)
  ; number of wavenumbers (odd, in order to
  ; contain exactly k=0)
```

```
k_arr= (findgen(klen)-klen/2+(1-(klen mod 2))/2.)*kmin
;optional spatial Hamming filtering to suppress the nearest neighbor sideband
if keyword_set(k_hann) then begin
   hamm=rebin(reform(hanning(dims[dimension],alpha=0.54),dexp),dims)
   spec=spec*hamm
   hamm=0
endif
;The actual transformation
fcomps=exp(inv*ima*xvec#k_arr)
kfspec=transpose(tensor_multiply(spec,fcomps),bacord)
;spec=transpose(temporary(spec),bacord)
result={kspec:kfspec,k:k_arr}
return,result
end

ENERGY TRANSFER ANALYSIS
location: /home/cziegler/auxcodes/en_transfer.pro
bispectrum with indices set for energy transfer analysis:
@/home/cziegler/auxcodes/bisp_mod.pro
trispectrum with the same index notation:
@/home/cziegler/auxcodes/a_trisp_m.pro
function en_transfer,x,y,$
                     fullt=fullt
;INPUT
;x and y are the spectrograms X(f,t) and Y(f,t)
;set the keyword fullt to access the full 2D T function
;instead of just T(f).
;OUTPUT
;A structure with the fields L (linear coefficient L(f), complex)
; and T (energy transfer function T(f))
```

Bibliography

[1] I. H. Hutchinson, R. Boivin, F. Bombarda, P. Bonoli, S. Fairfax C. Fiore, J. Goetz, S. Golovato, R. Granetz, M. Greenwald, S. Horne, A. Hubbard, J. Irby, B. LaBombard, B. Lipschultz, E. Marmar, G. McCracken, M. Porkolab, J. Rice, J. Snipes, Y. Takase, J. Terry, S. Wolfe, C. Christensen, D. Garnier, M. Graf, T. Hsu, T. Luke, M. May, A. Niemczewski, G. Tinios, J. Schachter, and J. Urbahn. *Phys. Plasmas*, 1:1511, 1994.

[2] B. LaBombard, J.E. Rice, A.E. Hubbard, J.W. Hughes, M. Greenwald, J. Irby, Y. Lin, B. Lipschultz, E.S. Marmar, C.S. Pitcher, N. Smick, S.M. Wolfe, S.J. Wukitch, and the Alcator Group. *Nucl. Fusion*, 44:1047–1066, 2004.

[3] J. Myra and D. D'Ippolito. *Phys. Plasmas*, 12:092511, 2005.

[4] J. Wesson. *Tokamaks*. Oxford University Press, 2004.

[5] B. LaBombard, J. W. Hughes, N. Smick, A. Graf, K. Marr, R. McDermott, M. Reinke, M. Greenwald, B. Lipschultz, J. L. Terry, D. G. Whyte, S. J. Zweben, and Alcator C-Mod Team. *Phys. Plasmas*, 15:056106, 2008.

[6] R. M. McDermott, B. Lipschultz, J. W. Hughes, P. J. Catto, A. E. Hubbard, I. H. Hutchinson, R. S. Granetz, M. Greenwald, B. LaBombard, K. Marr, M. L. Reinke, J. E. Rice, D. Whyte, and Alcator C-Mod Team. *Phys. Plasmas*, 16:056103, 2009.

[7] J. Hugill. *Nucl. Fusion*, 23:331, 1983.

[8] L. A. Artsimovich. *Nucl. Fusion*, 12:215, 1972.

[9] H. P. Furth. *Nucl. Fusion*, 15:487, 1975.

[10] M. Greenwald. *Plasma Phys. Control. Fusion*, 44:27, 2002.

[11] S. I. Krashenninikov. *Phys. Letters A*, 283:368, 2005.

[12] D. A. D'Ippolito, J. R. Myra, and S. I. Krasheninnikov. *Phys. Plasmas*, 9:222, 2002.

[13] B. Coppi. *Nucl. Fusion*, 42:1, 2002.

[14] D. A. D'Ippolito and J. R. Myra. *Phys. Plasmas*, 15:082316, 2008.

[15] F. Wagner, G. Becker, K. Behringer, D. Campbell, A. Eberhagen, W. Engelhardt, G. Fussmann, O. Gehre, J. Gernhardt, G. v. Gierke, G. Haas, M. Huang, F. Karger, M. Keilhacker, O. Klüber, M. Kornherr, K. Lackner, G. Lisitano, G. G. Lister, H. M. Mayer, D. Meisel, E. R. Müller, H. Murmann, H. Niedermeyer, W. Poschenrieder, H. Rapp, H. Röhr, F. Schneider, G. Siller, E. Speth, A. Stäbler, K. H. Steuer, G. Venus, O. Vollmer, and Z. Yü. *Phys. Rev. Lett.*, 49(19):1408–1412, 1982.

[16] ITER physics expert groups. *Nucl. Fusion*, 39:2137, 1999.

[17] J. Freidberg. *Plasma Physics and Fusion Energy.* Cambridge University Press, 2008.

[18] F. Wagner et al. Recent results of h-mode studies on asdex. In *Proceedings of the Thirteenth Conference on Plasma Physics and Controlled Nuclear Fusion Research (IAEA, Vienna), vol. I, pp. 277-90*, 1982.

[19] J. L. Terry, I. Cziegler, A. E. Hubbard, J. A. Snipes, J.W. Hughes, M. J. Greenwald, B. LaBombard, Y. Lin, P. Phillips, and S. Wukitch. *J. Nucl. Mat.*, 363-365:994–999, 2007.

[20] J. L. Terry, N.P. Basse, I. Cziegler, M. Greenwald, O. Grulke, B. LaBombard, S.J. Zweben, E.M. Edlund, J.W. Hughes, L. Lin, Y. Lin, M. Porkolab, M. Sampsell, B. Veto, and S.J. Wukitch. *Nucl. Fusion*, 45:1321, 2005.

[21] A. Mazurenko, M. Porkolab, D. Mossessian, J. A. Snipes, X. Q. Xu, and W. M. Nevins. *Phys. Rev. Lett.*, 89:225004, 2002.

[22] J. D. Jackson. *Classical Electrodynamics.* John Wiley & Sons, Illinois, 1962.

[23] I. H. Hutchinson et al. *Plasma Phys. Control. Fus.*, 41:A609, 1999.

[24] M. Greenwald. *Nucl. Fusion*, 37:793, 1997.

[25] G. R. Tynan, P. H. Diamond, C. Holland, S. H. Muller, M. Xu, Z. Yan, and J. Yu. *Plasma Phys. Control. Fusion*, 51:113001, 2009.

[26] A. J. Wootton, B. A. Carreras, H. Matsumoto, K. McGuire, W. A. Peebles, Ch. P. Ritz, P. W. Terry, and S. J. Zweben. *Phys. Fluids B*, 2:2879, 1990.

[27] P. C. Liewer. *Nucl. Fusion*, 25:543, 1985.

[28] D. L. Brower et al. Tokamaks: Turbulence and first test of an ergodic magnetic limiter. In *Plasma Physics and Controlled Nuclear Fusion Research, IAEA*, 1985.

[29] D. L. Brower, W. A. Peebles, N. C. Luhmann, and R. L. Savage. *Phys. Rev. Lett.*, 54:689, 1985.

[30] C. M. Surko and R. E. Slusher. *Phys. Rev. Lett.*, 37:1747, 1976.

[31] S.J. Zweben and R. W. Gould. *Nucl. Fusion*, 25:171, 1985.

[32] M. Greenwald. *Nucl. Fusion*, 28:2199, 1988.

[33] B. LaBombard, R. L. Boivin, M. Greenwald, J. Hughes, B. Lipschultz, D. Mossessian, C. S. Pitcher, J. L. Terry, and S. J. Zweben. *Phys. Plasmas*, 8:2107, 2001.

[34] B. LaBombard. *Nucl. Fusion*, 45:1658–1675, 2005.

[35] A. Hasegawa and K. Mima. *Phys. Rev. Lett.*, 39(4):205, 1977.

[36] R. H. Kraichnan. *Phys. Fluids*, 10:1417, 1967.

[37] W. Horton. *Phys. Fluids*, 29:1491, 1986.

[38] M. Wakatani and A. Hasegawa. *Phys. Fluids*, 27:611, 1984.

[39] B. D. Scott. *Phys. Plasmas*, 12:062314, 2005.

[40] S. J. Zweben, D. P. Stotler, J. L. Terry, B. LaBombard, M. Greenwald, M. Muterspaugh, C. S. Pitcher, K. Hallatschek, R. J. Maqueda, B. Rogers, J. L. Lowrance, V. J. Mastrocola, and G. F. Renda. *Phys. Plasmas*, 9:1981, 2002.

[41] J. L. Terry, S. J. Zweben, K. Hallatschek, B. LaBombard, R. J. Maqueda, B. Bai, C. J. Boswell, M. Greenwald, D. Kopon, W. M. Nevins, C. S. Pitcher, B. N. Rogers, D. P. Stotler, and X. Q. Xu. *Phys. Plasmas*, 10:1739, 2003.

[42] D. P. Stotler, B. LaBombard, J. L. Terry, and S. J. Zweben. *J. Nucl. Mater.*, 313-316:1066, 2003.

[43] J. L. Terry, S. J. Zweben, B. Bose, O. Grulke, E. S. Marmar, J. Lowrance, V. Mastrocola, , and G. Renda. *Rev. Sci. Inst.*, 75:4196, 2004.

[44] J. L. Terry, R. Maqueda, C. S. Pitcher, S. J. Zweben, B. LaBombard, E. S. Marmar, A. Yu. Pigarov, and G. Wurden. *J. Nucl. Mater.*, 290-293:757, 2001.

[45] R. Jha, P. K. Kaw, S. K. Mattoo, C. V. S. Rao, Y. C. Saxena, and ADITYA Team. *Phys. Rev. Lett.*, 69:1375, 1992.

[46] V. Antoni, V. Carbone, E. Martines, G. Regnoli, G. Serianni, N. Vianello, and P. Veltri. *Europhys. Lett.*, 54:57, 2001.

[47] N. L. Johnson, S. Kotz, and N. Balakrishnan. *Continuous Univariate Distributions*. John Wiley & Sons, New York, 1995.

[48] U. Frisch. *Turbulence*. Cambridge University Press, 1995.

[49] J. E. Wilkins Jr. *Annals of Math. Stat.*, 15(3):333, 1944.

[50] P. C. Chatwin, D. M. Lewis, and N. Mole. *Adv. Comput. Math.*, 6:227, 1996.

[51] M. Hatori. *J. Oceanogr. Soc. Jpn.*, 40:1, 1984.

[52] B. Labit, I. Furno, A. Fasoli, A. Diallo, S. H. Müller, G. Plyushchev, M. Podestà, and F. M. Poli. *Phys. Rev. Lett.*, 98:255002, 2007.

[53] J. A. Boedo, D. L. Rudakov, R. A. Moyer, G. R. McKee, R. J. Colchin, M. J. Schaffer, P. G. Stangeby, W. P. West, S. L. Allen, T. E. Evans, R. J. Fonck, E. M. Hollmann, S. Krasheninnikov, A. W. Leonard, W. Nevins, M. A. Mahdavi, G. D. Porter, G. R. Tynan, D. G. Whyte, and X. Xu. *Phys. Plasmas*, 10:1670, 2003.

[54] B. Nold, G. D. Conway, T. Happel, H. W. Müller, M. Ramisch, V. Rohde, U. Stroth, and the ASDEX Upgrade Team. *Plasma Phys. Control. Fusion*, 52:065005, 2010.

[55] F. Sattin, P. Scarin, M. Agostini, R. Cavazzana, G. Serianni, M. Spolaore, and N. Vianello. *Plasma Phys. Control. Fusion*, 48:1033, 2006.

[56] M. Agostini, S. J. Zweben, R. Cavazzana, P. Scarin, G. Serianni, R. J. Maqueda, and D. P. Stotler. *Phys. Plasmas*, 14:102305, 2007.

[57] R. Graves, J. Horacek, R. A. Pitts, and K. I. Hopcraft. *Plasma Phys. Control. Fusion*, 47:L1, 2005.

[58] A. N. Kolmogorov. *Dokl. Akad. Nauk SSSR*, 32:16, 1941. reprinted in Proc. R. Soc. Lond. A 434,15.

[59] M. Farge. *Ann. Rev. of Fluid Mech.*, 24:395, 1992.

[60] G. Y. Antar, S. I. Krasheninnikov, P. Devynck, R. P. Doerner, E. M. Hollmann, J. A. Boedo, S. C. Luckhardt, and R. W. Conn. *Phys. Rev. Lett.*, 87:065001, 2001.

[61] I. Furno, B. Labit, M. Podestà, A. Fasoli, S. H. Müller, F. M. Poli, P. Ricci, C. Theiler, S. Brunner, A. Diallo, and J. Graves. *Phys. Rev. Lett.*, 100:055004, 2008.

[62] S. J. Zweben, R.J. Maqueda, D.P. Stotler, A. Keesee, J. Boedo, C.E. Bush, S.M. Kaye, B. LeBlanc, J.L. Lowrance, V.J. Mastrocola, R. Maingi, N. Nishino, G. Renda, D.W. Swain, J.B. Wilgen, and the NSTX Team. *Nucl. Fusion*, 44:134, 2004.

[63] S. H. Müller, A. Diallo, A. Fasoli, I. Furno, B. Labit, , and M. Podestà. *Phys. Plasmas*, 14:110704, 2007.

[64] B. Carreras, V. E. Lynch, and B. LaBombard. *Phys. Plasmas*, 8:3702, 2001.

[65] J. A. Boedo, D.L. Rudakov, R.J. Colchin, R.A. Moyer, S. Krasheninnikov, D.G. Whyte, G.R. McKee, G. Porter, M.J. Schaffer, P.C. Stangeby, W.P. West, S.L. Allen, and A.W. Leonard. *J Nucl. Mater.*, 313-316:813, 2003.

[66] M. Agostini, P. Scarin, R. Cavazzana, F. Sattin, G. Serianni, M. Spolaore, and N. Vianello. *Plasma Phys. Control. Fusion*, 51:105003, 2009.

[67] T. Carter. *Phys. Plasmas*, 13:010701, 2006.

[68] G. R. Tynan, M. J. Burin, C. Holland, G. Antar, N. Crocker, and P. H. Diamond. *Phys. Plasmas*, 11:5195, 2004.

[69] J. Myra and D. D'Ippolito. *Phys. Plasmas*, 13:112502, 2006.

[70] S. I. Krashenninikov, D. A. D'Ippolito, and J. R. Myra. *J. Plasma Phys.*, 74:679, 2008.

[71] J. A. Boedo, D. Rudakov, R. Moyer, S. Krasheninnikov, D. Whyte, G. McKee, G. Tynan, M. Schaffer, P. Stangeby, P. West, S. Allen, T. Evans, R. Fonck, E. Hollmann, A. Leonard, A. Mahdavi, G. Porter, M. Tillack, and G. Antar. *Phys. Plasmas*, 8:4826, 2001.

[72] A. Fasoli, B. Labit, M. McGrath, S. H. Müller, G. Plyushchev, M. Podestà, and F. M. Poli. *Phys. Plasmas*, 13:055902, 2006.

[73] J. R. Myra, D. A. DIppolito, D. P. Stotler, S. J. Zweben, B. P. LeBlanc, J. E. Menard, R. J. Maqueda, and J. Boedo. *Phys. Plasmas*, 13:092509, 2006.

[74] D. C. Pace, M. Shi, J. E. Maggs, G. J. Morales, and T. A. Carter. *Phys. Plasmas*, 15:122304, 2008.

[75] J. Li and Y. Kishimoto. *Phys. Plasmas*, 17:072304, 2010.

[76] Y. Kim, J. M. Beall, E. J. Powers, and R. W. Miksad. *Phys. Fluids*, 23:258, 1980.

[77] G. I. Taylor. *Proc. R. Soc. Lond. A*, 164:476, 1938.

[78] P. C. Stangeby. *The Plasma Boundary of Magnetic Fusion Devices.* Institute of Physics, Berkshire, 2000.

[79] L. C. Johnson and E. Hinnov. *Quant. Spectrosc. Radiat. Transfer*, 13:333, 1973.

[80] D.P. Stotler. *J. Nucl. Mat.*, 313-316:1066, 2003.

[81] J.W. Hughes, D. A. Mossessian, A. E. Hubbard, E. S. Marmar, D. Johnson, and D. Simon. *Rev. Sci. Instrum.*, 72:1107, 2001.

[82] N. Smick and B. LaBombard. *Rev. Sci. Instrum.*, 80:023502, 2009.

[83] B. LaBombard, S. Gangadhara, B. Lipschultz, and C.S. Pitcher. *J. Nucl. Mat.*, 313-316:995–999, 2003.

[84] Y. Sechrest, T. Munsat, D. A. DIppolito, R. J. Maqueda, J. R. Myra, D. Russell, and S. J. Zweben. *Phys. Plasmas*, 18:012502, 2011.

[85] J. W. Hughes, D. A. Mossessian, A. E. Hubbard, B. LaBombard, and E. S. Marmar. *Phys. Plasmas*, 9:3019, 2002.

[86] T. H. Osborne, R. J. Groebner, L. L. Lao, A. W. Leonard, R. Maingi, R. L. Miller, G. D. Porter, D. M. Thomas, and R. E. Waltz. *Plasma Phys. Control. Fusion*, 40:845, 1998.

[87] W. Suttrop, M. Kaufmann, H. J. de Blank, B. Brüsehaber, K. Lackner, V. Mertens, H. Murmann, J. Neuhauser, F. Ryter, H. Salzmann, J. Schweinzer, J. Stober, H. Zohm, and the ASDEX Upgrade Team. *Plasma Phys. Control. Fusion*, 39:2051, 1997.

[88] S. Zweben. *Phys. Fluids*, 28:974, 1985.

[89] F. Sattin, M. Agostini, P. Scarin, N. Vianello, R. Cavazzana, L. Marrelli, G. Serianni, S. J. Zweben, R. J. Maqueda, Y. Yagi, H. Sakakita, H. Koguchi, S. Kiyama, Y. Hirano, and J. L. Terry. *Plasma Phys. Control. Fus.*, 51:055013, 2009.

[90] R. Sánchez, B. Ph. van Milligen, D. E. Newman, and B. A. Carreras. *Phys. Rev. Lett.*, 90:185005, 2003.

[91] J.W. Hughes. *Nucl. Fusion*, 47:1057, 2007.

[92] A.E. Hubbard, R. L. Boivin, R. S. Granetz, M. Greenwald, J. W. Hughes, I. H. Hutchinson, J. Irby, B. LaBombard, Y. Lin, E. S. Marmar, A. Mazurenko, D. Mossessian, E. Nelson-Melby, M. Porkolab, J. A. Snipes, J. Terry, S. Wolfe, S. Wukitch, B. A. Carreras, V. Klein, and T. Sunn Pedersen4. *Phys. Plasmas*, 8:2033, 2001.

[93] M. Greenwald, J.L. Terry, S.M. Wolfe, S. Ejima, M.G. Bell, S.M. Kaye, and G.H. Neilson. *Nucl. Fusion*, 28:2199, 1988.

[94] M. Greenwald. *Fusion Sci. Tech.*, 51:266, 2007.

[95] R. A. Moyer, J. W. Cuthbertson, T. E. Evans, G. D. Porter, and J. G. Watkins. *J Nucl. Mater.*, 241-243:633, 1997.

[96] A. E. White, S. J. Zweben, M. J. Burin, T. A. Carter, T. S. Hahm, J. A. Krommes, and R. J. Maqueda. *Phys. Plasmas*, 13:072301, 2006.

[97] J. A. Boedo. *J Nucl. Mater.*, 390-391:29, 2009.

[98] O. Cadot, Y. Couder, A. Daerr, S. Douady, and A. Tsinober. *Phys. Rev. E*, 56(1):427, 1997.

[99] M. K. Rivera, W. B. Daniel, S. Y. Chen, and R. E. Ecke. *Phys. Rev. Lett.*, 90(10):104502, 2003.

[100] P. Manz, M. Ramisch, and U. Stroth. *Plasma Phys. Control. Fusion*, 51:035008, 2009.

[101] D. E. Newman, P. W. Terry, P. H. Diamond, and Y. M. Liang. *Phys. Fluids B*, 5(4):1140, 1993.

[102] Y. M. Liang, P. H. Diamond, X. H. Wang, D. E. Newman, and P. W. Terry. *Phys. Fluids B*, 5(4):1128, 1993.

[103] M. Williams and C. Dainty. *Dig. Sig. Proc.*, 91:45, 1991.

[104] K. Itoh, Y. Nagashima, S.-I. Itoh, P. H. Diamond, A. Fujisawa, M. Yagi, and A. Fukuyama. *Phys. Plasmas*, 12:102301, 2005.

[105] T. Yamada, S.-I. Itoh, S. Inagaki, Y. Nagashima, S. Shinohara, N. Kasuya, K. Terasaka, K. Kamataki, H. Arakawa, M. Yagi, A. Fujisawa, and K. Itoh. *Phys. Plasmas*, 17:052313, 2010.

[106] C. P. Ritz and E. J. Powers. *Physica D*, 20:320, 1986.

[107] C. P. Ritz, E. J. Powers, and R. D. Bengtson. *Phys. Fluids B*, 1:153, 1989.

[108] Y. Kim, R. D. Durst, R. J. Fonck, A. Ware, and P. W. Terry. *Phys. Plasmas*, 3:11, 1996.

[109] S. J. Camargo, D. Biskamp, and B. D. Scott. *Phys. Plasmas*, 2:48, 1995.

[110] B. D. Scott. *Plasma Phys. Control. Fusion*, 45:A385, 2003.

[111] B. D. Scott. *Plasma Phys. Control. Fusion*, 39:1635, 1997.

[112] U. Stroth, F. Greiner, C. Lechte, N. Mahdizadeh, K. Rahbarnia, and M. Ramisch. *Phys. Plasmas*, 11:2558, 2004.

[113] P. Manz, M. Ramisch, U. Stroth, V. Naulin, and B. D. Scott. *Plasma Phys. Control. Fusion*, 50:035008, 2008.

[114] C. Holland, G. R. Tynan, R. J. Fonck, G. R. McKee, J. Candy, and R. E. Waltz. *Phys. Plasmas*, 14:056112, 2007.

[115] N. Winsor, J. L. Johnson, and J. M. Dawson. *Phys. Fluids*, 11:2448, 1968.

[116] I. H. Hutchinson, J. E. Rice, R. S. Granetz, and J. A. Snipes. *Phys. Rev. Lett.*, 84(15):3330, 2000.

[117] A. E. Hubbard, D. G. Whyte, R. M. Churchill, I. Cziegler, A. Dominguez, T. Golfinopoulos, J. W. Hughes, J. E. Rice, I. Bespamyatnov, M. J. Greenwald, N. Howard, B. Lipschultz, E. S. Marmar, M. L. Reinke, W. L. Rowan, J. L. Terry, and the Alcator C-Mod Group. *Phys. Plasmas*, 18:056115, 2011.

[118] D. DIppolito and J. Myra. *Phys Fluids B*, 5:3603, 1993.

[119] D. Whyte, A.E. Hubbard, J.W. Hughes, B. Lipschultz, J.E. Rice, E.S. Marmar, M. Greenwald, I. Cziegler, A. Dominguez, T. Golfinopoulos, N. Howard, L. Lin, R.M. McDermott, M. Porkolab, M.L. Reinke, J. Terry, N. Tsujii, S. Wolfe, S. Wukitch, Y. Lin, and the Alcator C-Mod Team. *Nucl. Fusion*, 50:105005, 2010.

[120] A.E. Hubbard, D. G. Whyte, R. M. Churchill, I. Cziegler, A. Dominguez, T. Golfinopoulos, J. W. Hughes, J. E. Rice, I. Bespamyatnov, M. J. Greenwald, N. Howard, B. Lipschultz, E. S. Marmar, M. L. Reinke, W. L. Rowan, J. L. Terry, and Alcator C-Mod Group. *Phys. Plasmas*, 18:056115, 2011.

[121] J. A. Snipes, B. LaBombard, M. Greenwald, I. H. Hutchinson, J. Irby, Y. Lin, A. Mazurenko, and M. Porkolab. *Plasma Phys. Control. Fusion*, 43:L23, 2001.

[122] G. R. McKee, R. J. Fonck, M. Jakubowski, K. H. Burrell, K. Hallatschek, R. A. Moyer, D. L. Rudakov, W. Nevins, G. D. Porter, P. Schoch, and X. Xu. *Phys. Plasmas*, 10:1712, 2003.

[123] G R McKee, D K Gupta, R J Fonck, D J Schlossberg, M W Shafer, and P Gohil. *Plasma Phys. Control. Fusion*, 48:S123, 2006.

[124] X. Q. Xu, Z. Xiong, Z. Gao, W. M. Nevins, and G. R. McKee. *Phys. Rev. Lett.*, 100:215001, 2008.

[125] D. A. Mossessian, P. B. Snyder, M. Greenwald, J. W. Hughes, Y. Lin, A. Mazurenko, S. Medvedev, H. R. Wilson, and S. Wolfe. *Plasma Phys. Control. Fusion*, 44:423, 2002.

[126] R. M. McDermott. *Edge Radial Electric Field Studies Via Charge Exchange Recombination Spectroscopy.* PhD thesis, MIT Plasma Science and Fusion Center, 2009.